VOLUME 3, ISSUE 2, JUNE 2026

THE JOURNAL OF CRIS

Featured Article

Chemical Extraction and Physicochemical Characterization of Cellulose Nanocrystals from Saudi Arabian Date Palm Waste for Drilling Fluid Applications

p. 23

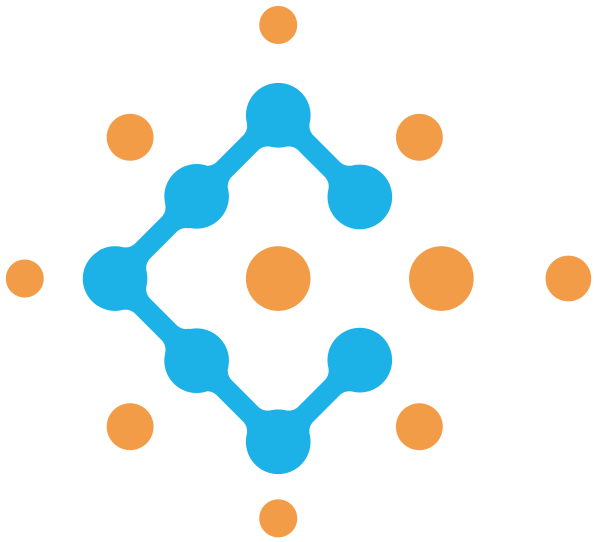

Table of **Contents**

Board Message

Dear Esteemed Readers,

It is with immense pride and excitement that we welcome you to the Second issue of volume 3 of our society's technical journal. Building on the foundation laid in our inaugural issue, this edition signifies our unwavering commitment to fostering innovation, sharing knowledge, and strengthening connections within our professional community.

As our field continues to evolve, so too does the scope of ideas and challenges we face. This journal remains dedicated to providing a platform where groundbreaking research, practical insights, and diverse perspectives converge. It is our hope that these contributions spark dialogue, inspire action, and drive meaningful progress.

In this issue, you will find an enriched selection of articles that delve deeper into the complexities of our discipline. Each piece reflects the dedication and expertise of our contributors, as well as the collective vision of our society to lead and inspire. I encourage you to explore the content thoughtfully and consider how these insights might shape your work and broaden your understanding.

The success of this endeavor would not be possible without the support and collaboration of our authors, reviewers, and editorial team. Their hard work and passion have once again made this journal a testament to the vibrancy and depth of our community.
As we move forward, let us continue to celebrate the spirit of curiosity, innovation, and excellence that unites us. Thank you for your ongoing engagement and support. Together, we are shaping the future of our field.

Warm regards,

Letter From The Editor

Dear Colleagues,

Welcome to the Second issue of Volume 3 of the Journal of Chemicals Research and Innovation Society. As we embark on another year of scientific exploration and knowledge sharing, we are excited to continue our mission of fostering groundbreaking research and collaboration in the chemical sciences.

Building on the foundation laid in our previous volumes, this issue presents a diverse collection of studies that showcase innovative methodologies, novel discoveries, and practical advancements across various fields of chemistry. Each contribution reflects the dedication and expertise of our research community, and we are proud to provide a platform for such impactful work.

I extend my deepest gratitude to our authors, reviewers, and editorial team for their unwavering commitment to excellence. Your contributions ensure that this journal remains a trusted source of scientific progress and a hub for meaningful discourse.

As we move forward, I encourage you to actively engage with the journal, whether through submitting your research, participating in discussions, or sharing insights with your peers. Together, we can continue to drive innovation and push the boundaries of chemical research.

Thank you for your continued support, and I look forward to the discoveries and advancements that lie ahead.

Best regards,

Shakeel Ahmed, Ph.D.,
Editor-in-Chief
Journal of Chemicals Research and Innovation Society

The Dosimetric and Radiobiological Evaluation of Patient Setup Errors in Radiotherapy Procedures during Nasopharyngeal Irradiation

Safa Elfaramawy[1], Ehab Attalla[2], Mohamed Alm El-Din[3], Fathi Elhussiny[1], Ahmed Elmekawy[1]

[1]Faculty of Science, Physics Department, Tanta University, Tanta, Egypt
[2]National Cancer Institute, Cairo University, Cairo, Egypt
[3]Department of Clinical Oncology, Tanta Faculty of Medicine, Tanta, Egypt
Correspondence: SafaElfaramawy@yahoo.com

Abstarct

Intensity-modulated radiotherapy (IMRT) is the leading treatment modality for nasopharyngeal cancer (NPC), offering precise tumor dose delivery while minimizing exposure to nearby organs at risk (OARs) compared to 3D conformal radiation therapy. This study assessed IMRT resilience to patient positioning errors. Ten nasopharynx carcinoma patients received IMRT with a simultaneous integrated boost, targeting tumor volumes with varying doses over 35 fractions. Simulated setup errors of 3, 5, and 7 mm were applied in different directions. The clinical target volume (CTV) showed minor sensitivity to 3 mm shifts. However, the planning target volume (PTV-70) displayed notable dose variations even with 3 mm shifts, especially in lateral directions. Dose discrepancies were minimal for CTV-70 but more pronounced for PTV-70 with increasing shift size. A 3 mm error notably impacted OAR doses. While the Conformity Index (CI) remained stable with a 3 mm shift, the Homogeneity Index (HI) deviated with larger shifts. Tumor Control Probability (TCP) variations were insignificant for CTV with 3 mm shifts but decreased substantially for PTV-70, particularly in lateral shifts. Setup errors also elevated normal tissue complication probabilities (NTCP) for several OARs. This study highlights IMRT limitation to setup errors in NPC treatment, potentially compromising tumor coverage and OAR protection. To improve IMRT reliability, a comprehensive evaluation emphasizing plan robustness and complexity is suggested, emphasizing the need for daily setup error correction to maintain treatment precision. Setup errors of up to 7 mm, with 3 mm errors occurring in a substantial portion of fractions without daily corrections, can significantly impact dose delivery to PTV, potentially compromising tumor control and increasing the risk to surrounding healthy tissues.

Keywords: Nasopharyngeal Radiotherapy; Intensity-modulated radiotherapy (IMRT); Set-up uncertainty; Dosimetric Evaluation; Radiobiological evaluation

Introduction

In NPC, surgical intervention is generally ruled out as an initial course of treatment

due to the complex anatomical location of the primary tumor, which is in close proximity to vital organs. Radiotherapy has emerged as the principal treatment modality for NPC, with intensity-modulated radiotherapy (IMRT) gaining prominence for its dose-painting capabilities. IMRT allows for precision in dose distribution to the target area while minimizing exposure to nearby OARs, making it superior to 3D conformal radiation therapy [1–5]. Recent advancements in radiotherapy have led to the introduction of the simultaneous integrated boost technique (SIB). This method delivers radiation doses to both initial and boost fields in parallel, thereby not only reducing the overall treatment duration but also potentially augmenting the dose to the primary target volume. However, the use of the SIB technique in head and neck cancers, including NPC, comes with its own set of challenges. Minor inaccuracies in patient positioning can lead to unintended radiation exposure to adjacent healthy tissues and an increased likelihood of missing the tumor altogether. This is particularly concerning given the steep dose gradient between the target volume and sensitive structures such as the parotid gland, spinal cord, and brainstem. As a result, managing setup uncertainties becomes a crucial aspect in the treatment of head and neck cancers [4]. Different previous studies evaluated the varying imaging protocols for imaging frequency, different alignment procedures and different registration sub regions during the treatment in order to strike a balance between treatment efficacy and patient position accurate [6–10].

Different healthcare centers adopt varying protocols for imaging frequency in order to strike a balance between treatment efficacy and accuracy. Incomplete knowledge of the remaining fractions can lead to unanticipated deviations in dose and the risk of tumor recurrence [11]. To address this issue, our study seeks to examine the impact of geometric deviations on the precision of highly-optimized IMRT plans [12–16]. While dose-volume histograms (DVH) offer a plethora of data, their complexity often hinders rather than aids the analytical process. To circumvent this challenge, these analysis employs models of tumor control probability (TCP) and normal tissue complication probability (NTCP) as more interpretable metrics [14].This approach enables us to assess the clinical implications of uncertainties in a more intuitive way, moving beyond the limitations of traditional dose-space evaluations. Moreover, this method allows us to incorporate uncertainties and their associated probabilities into the expected outcomes for both tumor control and tissue toxicity, facilitating population-level impact assessments[2, 15].

This study focuses on setup errors across three different shifts 3 mm, 5 mm, and 7 mm in all axes of the Cartesian coordinate system. These values were selected to encapsulate both the range of clinically anticipated uncertainties (3 mm and 5 mm) as well as larger, more extreme uncertainties (7 mm) to observe their exaggerated effects [11, 15–20]. The study aim is to estimate and correlate TCP and NTCP values with traditional dosimetric criteria in IMRT plans for a sample of 10 patients diagnosed with nasopharyngeal carcinoma. This study offers a framework for improving IMRT precision by emphasizing the importance of robust planning, adaptive imaging protocols, and personalized immobilization strategies to mitigate setup errors and optimize treatment outcomes in NPC.

Methodology

Dosimetric Analysis and Treatment Protocols for IMRT:

In this retrospective dosimetric study, patient anonymity was maintained by omitting personal identifiers like age and gender. The research focused on ten patients diagnosed with locally advanced nasopharyngeal carcinoma, who were treated using IMRT with the simultaneous integrated boost (SIB) technique and concurrent chemotherapy. Patients were immobilized in a supine position using custom thermoplastic head-neck-shoulder casts. High-resolution computed tomography (CT) scans were taken in helical mode with a 3 mm slice thickness, covering the area from the skull vertex to mid-chest. All treatment planning was conducted in the Eclipse software (Version 13.7, Varian Medical Systems, USA), and treatments were administered via a Clinac 600C linear accelerator equipped with 6 MV photons and an 80-leaf multileaf collimator.

To ensure consistency and control for operator variability, all contouring was carried out by a single oncologist and validated by a senior counterpart, while one medical physicist created all IMRT plans using nine distributed coplanar fields. Dosimetric calculations were performed using the Anisotropic Analytical Algorithm (AAA) on a 2.5 mm calculation grid, optimized with a dose volume optimizer. The study used multiple dose levels prescribed to PTV using the SIB technique. These included doses of 70 Gy for PTV70, 60 Gy for PTV60, and 54 Gy for PTV54. All clinical CTV were expanded by a 3 mm margin to form the PTVs, and prescription doses were administered in either 33 (N= 2) or 35 (N= 3) fractions.

Imaging Protocol

Two orthogonal digitally reconstructed radiographs (DRRs) were generated using the treatment planning software, with a field size of 10 × 10 cm^2 and gantry angles set to 0° (anterior) and 90° (lateral). These DRRs were transferred to the treatment unit as reference images. Portal images were then acquired at the same gantry angles using the electronic portal imaging device (EPID) system integrated with Varian linear accelerators.

Anatomic reference landmarks included at least two clearly visible bony structures. For anterior images, landmarks such as the external mandible profile, nasal septum, maxillary sinus, and spinous process of a lower cervical vertebra were commonly used. For lateral images, features such as the internal and external mandible profiles, skull base, and cervical vertebral bodies.

Setup errors were assessed at least three times during the first week of treatment and subsequently on a weekly basis. If displacements exceeding 2 mm were observed in any direction, the linear accelerator couch was adjusted to realign with the treatment isocenter, followed by the acquisition of new electronic portal images (EPIs).

Uncertainty analysis

Selected patient setup errors in this study encompass a clinically meaningful range of uncertainties commonly observed in head and neck radiotherapy. Extant literature, exploring various tracking and immobilization methods, reports both random and systematic setup uncertainties that fluctuate between 1 mm and 5 mm [15, 17, 18, 20, 21]. Hence, setup errors of 3 mm and 5 mm are considered to represent a typical clinical scenario, while a 7 mm setup

error serves as an outlier, simulating an extreme case.

The Plan Uncertainty tool in Eclipse version 13 serves as the computational backbone for assessing treatment plan resilience against simulated isocenter shifts. This tool allows for the semi-automatic generation, computation, and archival of dose distributions in altered replica plans. In these modified plans, isocenter shifts can be arbitrarily applied along the X, Y (axial), or Z (cranio-caudal) axes. The original treatment plan acts as the benchmark for all recalculations. Shifts are applied along only one axis at a time, and both positive and negative deviations from the reference isocenter coordinates are considered. The study includes an analysis of five sets of modified plans with shifts of 3 mm, 5 mm, and 7 mm.

Initial treatment plans were formulated in the Eclipse treatment planning system, During the treatment planning process, various OAR dose constraints were used as per Radiation Therapy Oncology Group (RTOG) and Quantitative Analysis of Normal Tissue Effects in the Clinic (QUANTEC) protocols adhering to the constraints specified in Table 1 adhering to the constraints specified in Table 1 and ensuring that at least 95% of the PTV received the prescribed dose, utilizing the sliding windows technique [22, 23]. Subsequent recalculations were performed within the planning system by displacing the isocenter by 3, 5, and 7 mm across all three spatial dimensions: anterior, posterior, superior, inferior, right lateral, and left lateral.

Table 1. Dosimetric Constraints for Organs at Risk (OARs) [22, 23]

Organ at Risk	Dosimetric Constraint (Gy)
Spinal Cord	50 Gy
Brain Stem	54 Gy
Optic Nerves/Chiasm	54 Gy
Parotid Glands	26 Gy
Lens	6 Gy

Evaluating Treatment Plan Efficacy through Physical and Biological Metrics

Differences in the quality of various treatment plans were assessed through the examination of both quantitative physical dose metrics and biological indices, derived from DVH. For both CTV and PTV, coverage was assessed based on the criteria presented in Table 1. Metrics such as maximum doses, denoted by doses received by 2% of the target volumes (D_2%), and minimum doses, represented by doses absorbed by 98% of the target volumes (D_{98}%), were reported alongside mean doses. Plan conformity was evaluated using a Conformity Number (CN), calculated as (CN) = (TVRI)2/(TV×VRI), as proposed by Van't Riet et al. [24]Here, VRI refers to the volume of the reference isodose, TV signifies the target volume, and TVRI denotes the target volume encompassed by the reference isodose.

Homogeneity Index (HI) served as a measure of dose uniformity within the target, defined as HI = $((D_2-D_{98})/D_P) \times 100$, in accordance with the formula developed by Wu et al.[25]. In this equation, D_2 and D_{98} correspond to the doses received by 2% and 98% of the target, respectively, while D_P is the prescribed dose. Lower HI values indicate greater homogeneity of the target dose.

Additionally, a freely accessible Matlab

code, developed by Gay et al. [26], was utilized for calculating Tumor Control Probability (TCP) and Normal Tissue Complication Probability (NTCP) based on the generalized Equivalent Uniform Dose (gEUD) concept. This code is capable of utilizing DVH parameters (Di,vi)(Di,vi) available from existing treatment plans.

The Equivalent Uniform Dose (EUD) concept posits that disparate dose distributions are functionally identical if they induce the same radiobiological impact on irradiated tissues. Calculations for Tumor Control Probability (TCP) and Normal Tissue Complication Probability (NTCP) principally rely on a unified set of equations, distinguishing this approach from alternative models that compute TCP and NTCP values independently. While the model parameters align well with tissue tolerance data presented by Emami et al. [27, 28] , it should be noted that the tolerance doses identified by these authors are specifically suited for evaluations within the framework of conventional therapies.

$$TCP=1/ (1+ (TCD_{50}/EUD))^{4\gamma 50} \quad (1)$$

$$NTCP=1/ (1+ (TD_{50}/EUD))^{4\gamma 50} \quad (2)$$

In this model, TD_{50} represents the dose tolerance associated with a 50% complication rate over a designated time period, such as the 5-year data provided by Emami et al. The γ50 parameter, which is dimensionless, is unique to the specific normal tissue or tumor under study and characterizes the slope of the dose-response curve [27, 29].

Figure 2: Summary of evaluated Radiobiological and dosimetric Parameters for PTV&CTV and OAR in Radiation Therapy [5, 30]

PTV/OARs	Evaluated Items
PTV 70	Mean (D2%, D98%, D95%, TCP, HI, CI) (ΔD2%, ΔD98%, ΔD95%, ΔTCP, ΔHI, ΔCI)
CTV 70	Mean (D2%, D99%, D98%, D95%, TCP) (ΔD2%, ΔD98%, ΔD95%, ΔTCP)
Brain Stem	ΔDmax, mean Dmax, ΔNTCP, mean NTCP
Spinal Cord	ΔDmax, mean Dmax, ΔNTCP, mean NTCP
Optic Nerve L	ΔDmax, mean Dmax, ΔNTCP, mean NTCP
Optic Nerve R	ΔDmax, mean Dmax, ΔNTCP, mean NTCP
Optic Chiasma	ΔDmax, mean Dmax, ΔNTCP, mean NTCP
Parotid L	ΔDmean, mean Dmean, ΔNTCP, mean NTCP
Parotid R	ΔDmean, mean Dmean, ΔNTCP, mean NTCP

Table 2 provides a comprehensive guide for evaluating the quality and efficacy of radiation therapy plans, focusing on different metrics for PTV-70, CTV-70 and OARs. For CTV-70, the main criteria are variations in $D_{2\%,}$ $D_{99\%}$, $D_{98\%}$ and $D_{95\%}$, Tumor Control Probability (TCP) and for PTV 70, the main criteria are variations in D2%, D98% and D95%, Tumor Control Probability (TCP), Homogeneity Index (HI), and Conformity Index (CI) to ensure that the target receives the prescribed dose while maintaining the quality of treatment. For critical OARs such as the Brain Stem, Spinal Cord, and Optic Structures (Nerve L, Nerve R, Chiasma), the emphasis is on evaluating the maximum dose and Normal Tissue Complication Probability (NTCP) to minimize radiation-induced complications. Lastly, for the Parotid glands (L and R), the focus is on the mean dose and NTCP, given these glands' sensitivity to dose averages, which could affect their function. The every normal tissue has an upper threshold of radiation exposure beyond which its functionality is compromised; this threshold is termed as radiation tolerance. Similarly, TCD_{50} defines the dose required to achieve control over 50% of the tumor, assuming the tumor is subjected to homogeneous irradiation. The values of a, γ50, TCD_{50} (Gy), TD_{50} (Gy) are shown in table 3.

Table 3. Utilized input parameters for calculating generalized equivalent uniform dose (Gy) and tumor control probability OARs [27, 28]

Structures	a	Gamma (γ50)	TCD50 (Gy)	TD50 (Gy)
Tumor	-13	2.28	51.77	-
Spinal Cord	7.40	4	-	66.50
Brain Stem	7	3	-	65
Parotid	1	2.2	-	28.40
Chiasma	25	3	-	65
Optic Nerve	25	3	-	65

Statistical analysis

For examining the significance of the

results obtained during plan comparison, statistical tests have been carried out. The variations in both target coverage and OAR doses across the nominal and shifted plan were statistically studied by using one way ANOVA. The differences between data were considered statistically significant, if denoted by small p values (<0.05).

Results

Dosimetric Evaluation: The impact of the simulated shift on targets

Figures 1(A-F) present a comprehensive illustration of a single session showcasing the dosimetric impact of setup errors, specifically accounting for a 3,5 mm shift in the left direction for both CTV-70 and PTV-70. Understanding the variations in dose coverage resulting from these shifts is pivotal for evaluating the robustness of the treatment plan. As depicted in the figures, deviations from the intended setup noticeably affect dose metrics such as D98%, D95%, and D99% volumes within the PTV-70, underscoring the need for a meticulous examination of plan sensitivity to positional errors, even with a 3 mm shift.

In contrast, the behavior observed for CTV-70 presents a distinct pattern. Despite experiencing shifts of up to 3 mm in all directions, the CTV maintains adequate dose coverage, thereby enhancing its resilience to setup errors, as depicted in Figure 1B. Notably, the dose parameters of CTV-70 are notably influenced by lateral shifts of 5 mm, as illustrated in Figure 1C.

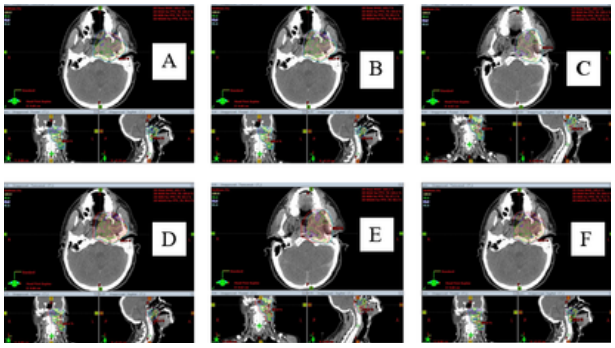

Figure1 (A-F) An example of uncertainties impact on Axial, Coronal and Sagittal dose distribution for CTV-70 & PTV-70. (A&D) dose distribution refers to the resulting dose distribution of CTV-70 & PTV -70 for the reference plan, respectively. (B&E) and (C&F) refers to the resulting recalculated dose distribution of CTV-70 & PTV -70, for 3mm and 5mm couch shift in the left direction, respectively.

Figure 2(A–B) illustrates the dose variation in the target volumes resulting from 3 mm shift scenarios in all directions for both CTV-70 and PTV-70, presented as DVH curves. Each curve on the graphs represents the average over the reference plan as well as plans recalculated for each left, Posterior and superior direction (+X, +Y, and +Z). Notably, the width of the envelope, defined as the area between all DVH curves, increases notably for PTV-70, particularly in lateral shifts, indicating a significant reduction in dose coverage.

In contrast, CTV-70 exhibits sufficient dose coverage and reduced sensitivity to 3 mm shifts. However, this observation raises concerns regarding the plan robustness in the presence of even minimal positional errors, particularly in lateral directions. At 5 and 7 mm shifts, coverage for both CTV-70 and PTV-70 is compromised, especially in lateral shifts, as depicted in Figure 3(A-C).

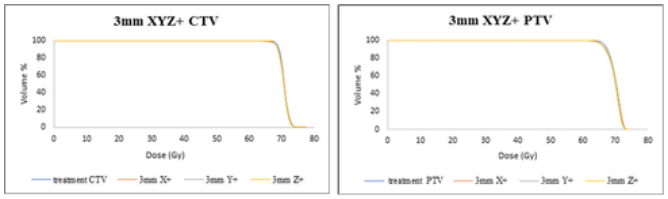

Figure 2(A-B): the dose volume histograms over single fraction for the reference plans and the plans recalculated after the application of the isocenter shifts over various directions. Each of these curves in the graphs corresponds also to the 3 plans recalculated for each of the shifts (+X, +Y and+ Z).

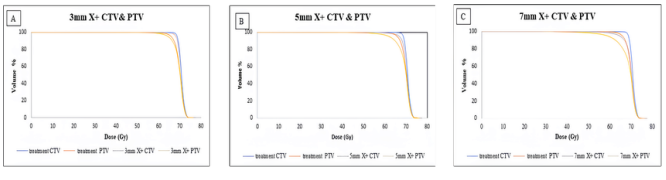

Figure 3(A-C): sample of dose-volume histograms

(DVHs) of CTV-70 and PTV-70, compared for 1 treatment plan and recalculated plans with 3,5,7 mm shifts in left direction, respectively.

The boxplot in Figure 4 (A&C) presents the average percentage dose variation, revealing minor dose discrepancies in CTV-70 for shifts of 3 mm, with mean variations of -0.99% for ΔD98% and -0.66% for ΔD95%. Importantly, indicates that these minor variations in ΔD98% and ΔD95% for a 3 mm shift in all directions are not statistically significant. The most significant dose variations were observed in the Right-Left directions, with the average variations for ΔD98% and ΔD95% in 5 mm and 7 mm isocenter shifts (compared to no shift) reported as -4.75% and -9.92% for ΔD98%, and -2.37% and -6.15% for ΔD95%, respectively. This demonstrates the impact of lateral shifts on dose accuracy, particularly for larger shift magnitudes.

In contrast to CTV-70, PTV-70 dosimetric parameters showed a significant impact from shifts as small as 3 mm in the Right-Left direction, as depicted in Figure 4(B&D). The mean changes in ΔD98% and ΔD95% for isocenter shifts of 3 mm, 5 mm, and 7 mm compared to no shift were -4.06%, -7.97%, and -15.83% for ΔD98%, and -2.55%, -7.78%, and -11.27% for ΔD95%, respectively.

Figure 4(F) indicates that ΔD2% for CTV-70 showed no significant differences. The average changes in ΔD2% for CTV-70 with isocenter shifts of 3 mm, 5 mm, and 7 mm from no shift were -0.532%, 0.343%, and 0.374%, respectively, with the largest deviations occurring in the inferior and the same occurs for PTV-70 with the largest deviation was observed in the inferior direction. The average changes in ΔD2% for PTV-70 with 3 mm, 5 mm, and 7 mm isocenter shifts from no shift were 0.57%, 1.06%, and 1.67%, respectively.

The mean absolute dosage (Gy) for D98%, D95%, and D2% in the CTV-70 and PTV-70 was compiled in Table 4. Despite a clear trend of deterioration in PTV coverage, the results indicate that there is no significant reduction in dose for any of the dosimtric parameters for CTV-70 under 3mm setup error. At 3mm shift for PTV-70 the dose reaches 62.08Gy and 64.18Gy for D98% and D95%, respectively, which is less than 95% of the prescribed dose. At 7 mm shift for CTV-70 the dose reaches to 59.84 Gy and 64.30 Gy for D98% and D95%, respectively, while for PTV-70 lowers to 53.61 Gy and 58.80 Gy for the 7 mm shift.

Table 4: The mean absolute dose (Gy) for CTV-70& PTV-70 for 10 patients due to shift scenarios. *Indicates a statistically significant difference

Shift in Setup	$D_{99\%}$(Gy) CTV	$D_{98\%}$(Gy) CTV	$D_{98\%}$ (Gy) PTV	$D_{95\%}$ (Gy) CTV	$D_{95\%}$(Gy) PTV	$D_{2\%}$(Gy) CTV	$D_{2\%}$(Gy) PTV
Zero shift	67.15	67.74	66.89	68.55	66.51	73.50	74.05
3mm Left lateral	65.64*	67.03	63.30*	68.21	65.08*	72.92	73.06
3mm Right lateral	65.89*	66.98	62.08*	68.07	64.81*	72.75	72.85
5mm Left lateral	63.00*	65.07*	60.51*	66.89*	63.00*	73.17	73.34
5mm Right lateral	62.34*	64.14*	58.16*	66.81*	62.18*	72.8	73.40
7mm Left lateral	59.57*	62.30*	57.06*	64.82*	60.37*	73.46	73.72
7mm Right lateral	57.57*	59.84*	53.61*	64.30*	58.80*	72.99	73.21
3mm Posterior	66.37*	67.24	64.08*	68.32	65.47*	72.79	72.81
3mm Anterior	64.94*	67.01	63.07*	68.13	64.90*	72.78	72.90
5mm Posterior	64.70*	66.17*	62.14*	67.41*	63.72*	72.90	73.14
5mm Anterior	61.73*	63.55*	59.03*	66.66*	62.63*	72.88	73.03
7mm Posterior	62.47*	64.36*	60.07*	66.07*	61.94*	73.04	73.36
7mm Anterior	57.96*	60.28*	55.98*	64.35*	59.93*	73.01	73.13
3mm Superior	66.45*	67.35	64.09*	68.48	65.37*	73.65	72.63
3mm Inferior	65.55*	67.12	62.30*	68.35	65.41*	73.11	73.58
5mm Superior	64.74*	65.97*	62.70*	67.18*	63.83*	72.45	72.64
5mm Inferior	62.88*	64.63*	59.01*	67.62*	63.21*	73.40	73.69
7mm Superior	62.73*	64.23*	61.11*	66.07*	62.06*	72.42	72.68
7mm Inferior	59.46*	61.54*	55.87*	65.82*	60.63*	73.77	74.05

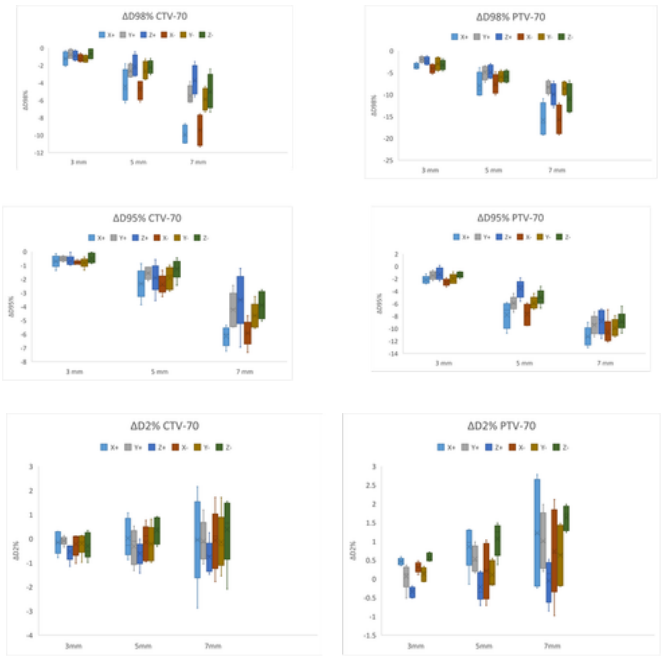

Figure 4: Box plot for percentage dose variation ΔD (%) for 3,5,7 mm setup errors in all directions for

D98%, D95% and D2% in (A, C,F) CTV-70, (B,D,G) PTV-70.The cross represents the mean, the line inside the box represents the median, the bottom of the box represents the 25% quartile, the top of the box represents the 75% quartile, the bottom whisker represents the minimum value, the top whisker represents the maximum value.

Table 5: Conformity index and Homoginty index

Shift in setup	HI	ΔHI	CI	ΔCI
Zero shift	0.12		0.94	
3mm Left lateral	0.16	0.04	0.90	0.04
3mm Right lateral	0.15	0.04	0.90	0.04
5mm Left lateral	0.21	0.09	0.86	0.08
5mm Right lateral	0.21	0.09	0.85	0.09
7mm Left lateral	0.27	0.15	0.82	0.13
7mm Right lateral	0.28	0.16	0.80	0.14
3mm Posterior	0.14	0.017	0.91	0.03
3mm Anterior	0.14	0.03	0.91	0.03
5mm Posterior	0.17	0.05	0.87	0.07
5mm Anterior	0.19	0.07	0.86	0.08
7mm Posterior	0.20	0.08	0.83	0.11
7mm Anterior	0.23	0.11	0.83	0.11
3mm Superior	0.11	0.03	0.93	0.02
3mm Inferior	0.15	0.03	0.92	0.02
5mm Superior	0.12	0.04	0.91	0.04
5mm Inferior	0.21	0.08	0.89	0.05
7mm Superior	0.14	0.06	0.86	0.08
7mm Inferior	0.25	0.13	0.86	0.08

Table 5 demonstrate that, the CI mean values in 3 mm, 5 mm and 7 mm shifts with respect to no shift were found 0.91, 0.87, and 0.83, respectively. The CI values were revealed no significant difference with nominal values in 3 mm shift a long all translational axis. Almost all other shifts lead to significant changes in the conformity.

The HI mean values in 3 mm, 5 mm and 7 mm isocenter shifts with respect to no shift were found 0.14,0.18, 0.23, respectively. The HI values were significantly closer to the nominal value in 3 mm for all shift scenarios but the difference was statistically significant in 5mm and 7 mm shifts.

The impact of the simulated shift on OARs

Figure 5 (A-F) illustrates the variation in dose received by organs at risk (OARs). Notably, the brain stem's dose-response envelope, as exemplified in Figure 5B, displays a narrow width, highlighting its high sensitivity to setup uncertainty. This sensitivity is particularly pronounced for posterior and lateral shifts, and to a lesser extent, for superior shifts, all of which are statistically significant even with a mere 3 mm shift. Conversely, anterior and inferior shifts did not significantly affect the dose to the brain stem across all evaluated shifts

The dose-volume statistics for the spinal cord, in response to various shifts, reveal that maximum point dose increases with greater isocenter misalignment, though not significantly at the D2% level. Significant impacts on the maximum dose are observed for lateral and posterior shifts, even with shifts as small as 3 mm, as illustrated in Figure 5A. In contrast, anterior, superior, and inferior shifts appear to have negligible effects on the spinal cord dose across all shifts

The analysis of right and left parotids under various shifts shows a moderate impact of posterior and inferior shifts on the mean dose (Dmean), whereas lateral shifts, followed by anterior and superior ones, significantly affect the dose to both parotids, even with 3 mm shifts, as depicted in Figure 5F.

Figure 5C presents the dose-volume statistics for the optic chiasma across different shifts. The maximum dose (Dmax) to the optic chiasma shows heightened sensitivity to setup uncertainty with lateral, posterior, and superior shifts, even at a 3 mm deviation. Meanwhile, the Dmax remains unaffected by anterior and inferior shifts, underscoring the critical importance of precise setup in avoiding undue exposure to these sensitive structures. For both the right and left optic nerves, a shift of 3 mm resulted in significant changes to the maximum dose (Dmax), particularly with lateral, anterior, and superior movements, indicating notable sensitivity.

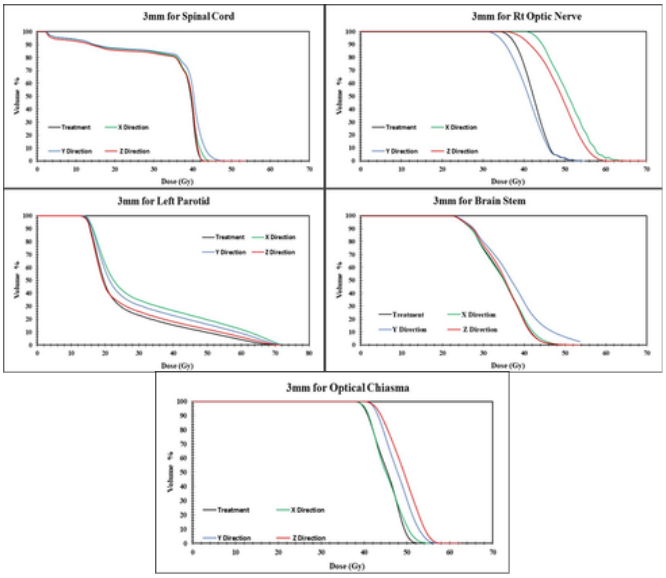

Figure 5: A sample of dose-volume histograms (DVHs) of OARs was compared for 1 treatment plan and 3 recalculated plans under 3 mm shift in left, posterior and superior direction.

Radiobiological evaluation

In exploring the robustness of radiation therapy plans against setup errors, specific thresholds were established to evaluate the impact on treatment and normal tissue complication probabilities (TCP and NTCP, respectively). For tumor control probability (TCP), a decrease greater than 2% was considered significant, while for neurological normal tissue complication probability (NTCP), an increase over 1%, and for all other NTCPs, a threshold of 5% was used to assess the significance of changes due to setup errors.

Table (6) revealed that the TCP variations in the clinical target volume (CTV) were minimal, staying below 1% for all considered directions with a 3mm shift and the reduction reached to 0.68%. However, significant sensitivity was observed in the planning target volume (PTV-70) in the right-left direction, indicating a notable decrease in TCP by over 2% even with a mere 3mm shift, and escalating to a dramatic decrease of 73.60% with a 7mm shift. This underscores the critical impact of lateral shifts on TCP and highlights the importance of precision in setup to ensure effective tumor control.

In Figure 6(A-B), the maximum reduction for TCP does not exceed 1% for CTV-70 shows insensitivity for TCP under 3mm shift, and with maximum average ΔTCP% reached to 5.08% in lateral direction, surprisingly, regarding PTV-70the average ΔTCP% in lateral direction reached to 2.42% with maximum variation reached to 73.60%.

Moreover, analyses of NTCP increases due to setup errors identified the most vulnerable regions and shifts. Specifically, a 3mm shift posed the highest risk of increased NTCP for the brainstem, spinal cord, and optic chiasma in posterior shifts; for the brainstem, spinal cord, parotid glands, optic chiasma, and optic nerves in lateral shifts; for the brainstem, parotids, optic nerves, and optic chiasma in superior shifts; and for the optic nerves in anterior shifts, Figure 7(A-F).

Table 6: radiobiological evaluation of setup uncertainty for CTV-70& PTV-70 for 10 patients due to set up uncertainty

Shift in setup	TCP% CTV	TCP% PTV	ΔTCP% CTV	ΔTCP% PTV
Zero shift	94.63%	93.13%		
3mm Left lateral	94.41%	90.29%	0.42%	2.42%
3mm Right lateral	94.29%	91.02%	0.68%	2.14%
5mm Left lateral	93.09%	68.41%	1.38%	24.30%
5mm Right lateral	92.71%	63.51%	1.77%	29.64%
7mm Left lateral	89.40%	38.60%	5.08%	54.09%
7mm Right lateral	86.23%	26.50%	4.40%	73.60%
3mm Posterior	94.39%	90.36%	0.48%	0.65%
3mm Anterior	94.31%	91.57%	0.63%	1.58%
5mm Posterior	93.69%	86.58%	0.79%	1.83%
5mm Anterior	92.48%	88.81%	1.99%	4.71%
7mm Posterior	93.03%	81.33%	1.45%	3.78%
7mm Anterior	90.55%	83.38%	3.93%	11.69%
3mm Superior	94.35 %	92.64%	0.53%	0.51%
3mm Inferior	94.30%	91.21%	0.63%	1.77%
5mm Superior	93.50%	91.63%	0.97%	1.70%
5mm Inferior	92.92%	87.69%	1.56%	5.52%
7mm Superior	92.93%	89.03%	1.54%	7.81%
7mm Inferior	91.65%	79.95%	2.80%	14.33%

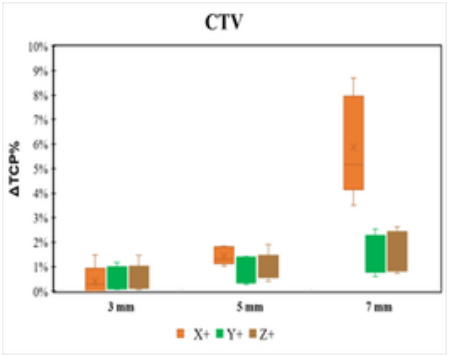

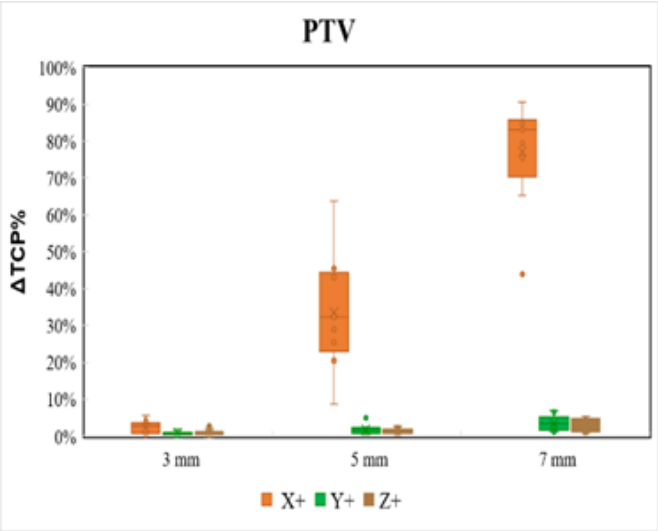

Figure 6 (A-B): The boxplot of ΔTCP% for CTV &PTV.

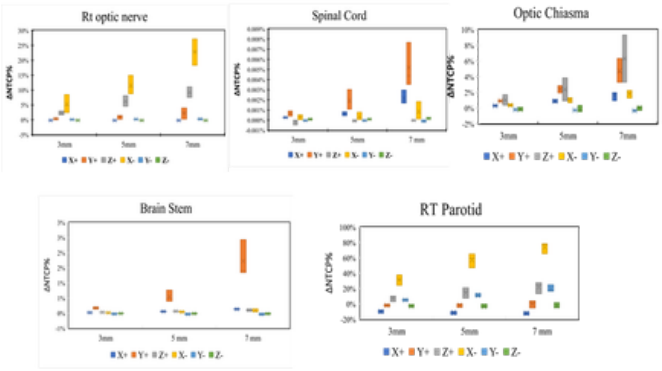

Figure 7 (A-F): The boxplot of ΔNTCP% for OARs.

Discussion

In this study, we evaluated the dosimetric and radiobiological impacts of setup errors on ten nasopharyngeal cancer patients treated with SIB-IMRT, using a weekly imaging protocol and robust patient immobilization. The findings provide insights into the robustness of treatment plans against isocenter misplacements and emphasize the importance of CTV-to-PTV margin selection in mitigating dosimetric impacts caused by positional uncertainties. Most of the studies have addressed the range of setup errors more than 5 mm shifts [14, 31] and based on these studies our assumption of random and systematic setup errors with standard deviations equal to 3,5,7 mm in each direction to simulate setup uncertainties.

In our study, with the CTV to PTV margins applied in the study 3mm in all directions, when the plan was recalculated within this margin, the coverage of the clinical target volume is not compromised in 3mm positioning errors. On the contrary, the isocenter positioning precision plays a relevant role in the case of the PTV and the data demonstrate that when the misplacement is comparable to the CTV to PTV margin, then the under-dosage estimation on the PTV becomes large in lateral shifts due to the area of the lymph nodes. A reason for the larger perturbation in the lymph node might be the adjacent location to skin-air as well as mucosal-air boundary.

In line with our results, recalculated the plan robustness under five distinct uncertainty plans (U-plans) using the first five setup mistakes that were acquired using CBCT. The findings highlighted the need of taking setup uncertainties into account when planning and executing treatments, as there were no discernible variations in D2cc for either PTV or CTV[5].

Our results indicate that ΔD98% &ΔD95% and ΔD2% for CTV-70 showed no significant differences with 3mm shift and the largest deviations occurring in the right -left shift for ΔD98% &ΔD95% and inferior direction for ΔD2% due to the involvement of lymph nodes and the dose falloff near the edges of CTV-60, respectively. The same attitude for PTV-70, ΔD2% shows the largest deviation was observed in the inferior direction, which can be attributed to dose variations at the periphery of the PTV-60 target.

The mean absolute dosage (Gy) for D98%, D95%, and D2% in the CTV-70 and PTV-70 was compiled in Table 4. Despite a clear trend of deterioration in PTV coverage, the results indicate that there is no significant

reduction in dose for any of the dosimtric parameters for CTV-70 under 3mm setup error. Similar to the focus of our study, Kaur [32] investigated the effects of setup uncertainties on target volume coverage, using kilovoltage cone beam computed tomography (kV CBCT). The research highlighted a significant discrepancy in PTV coverage when comparing the reference plan to the plan sum, which aggregated all recalculated plans at different isocenters based on setup errors in the x, y, and z directions.

In a related vein, Shinde [33]examined the dosimetric impact of interfractional 6D setup errors on tongue cancer treatments employing IMRT and VMAT, with daily monitoring via kV-CBCT. The research pointed out that interfractional 6D setup errors significantly affected D98% for CTV-60, CTV-54, PTV-60, and PTV-54, with measured errors reaching up to 7 mm, 7 mm, 8 mm, and rotations of 3.00, 2.90, and 2.90 degrees along the X, Y, Z, R_X, R_Y, and R_Z axes, respectively, showcasing a statistically significant dosimetric impact ($p < 0.05$). Expressing a similar viewpoint about the significance of taking uncertainty into account, Yang [18] proposed robustness optimization as a vital strategy for reducing unnecessary radiation dose to normal tissues owing to the conventional CTV-to-PTV margin concept. Yang's study engaged in a thorough assessment of worst-case robust optimization for intensity-modulated proton therapy (IMPT) plans, incorporating both setup and range uncertainties. This approach aimed to verify the hypothesis that worst-case robust optimization strategies are sufficiently comprehensive to accommodate the majority of potential setup and range uncertainties encountered in practical scenarios, thereby enhancing the accuracy and safety of radiation therapy treatments.

One plausible explanation for the heightened perturbation observed in lymph nodes could be their proximity to the skin-air and mucosal-air boundaries. This phenomenon is also evident in CTV-70 when shifts extend beyond 5 mm. Based on our findings, it is evident that when employing a 3mm CTV-PTV margin, the coverage of the CTV remains uncompromised even in the presence of a setup error of 3mm. This observation is consistent with the research conducted by Navran [31], which demonstrated that decreasing the CTV-PTV margin from 5 to 3 mm, coupled with daily CBCT-guided VMAT, mitigated the severity, frequency, and duration of radiation-induced toxicity without compromising treatment outcomes.

Furthermore, Prabhakar [14] reported that for simulated setup errors of 3, 5, and 10 mm, the dose to the target volume gradually decreases with increasing setup error, particularly in superior and inferior shifts. This finding underscores the importance of understanding and mitigating the impact of setup errors on dose delivery to ensure optimal treatment outcomes.

Ding study analyzed the impact of setup uncertainties by evaluating the first five CBCT scans to adjust the CTV-to-PTV margin. This adjustment enhanced the robustness of the CTV and GTV, reducing but not eliminating the risk of underdosage. The research employed a sophisticated method for quantifying plan robustness, enabling a detailed dose assessment within highly optimized clinical treatment plans. Additionally, Stroom [34] findings highlighted that applying specific CTV to PTV margins—5 mm for lung, 3 mm for brain, and 2 mm for the spine—ensures clinical target volume coverage remains

unaffected in most cases, even with significant setup errors (ranging from 0.5 to 3 mm). This indicates the effectiveness of strategic margin adjustments in preserving target coverage under varying setup inaccuracies.

As to OARs (Fig4), the organs exhibited weak robustness due to their locations in the vicinity of PTVs. These findings are in line with that result reported that the brain stem proximity to the PTV rendered it less robust to setup errors.

The dose-volume statistics for the spinal cord, in response to various shifts, reveal that maximum point dose increases with greater isocenter misalignment, though not significantly at the D2% level. These results corroborate with those of Prabhakar [14], who found that a setup error of 3 mm in the posterior and lateral directions significantly impacts the spinal cord dose. These outcomes of parotid glands align with the findings [14], indicating that setup errors in the lateral and anterior directions notably influence the dose to both parotids. Ding [5] also found that, without setup correction, the bilateral parotid glands were particularly sensitive to setup uncertainty, owing to their partial enclosure by PTVs.

The maximum dose (Dmax) to the optic chiasma shows heightened sensitivity to setup uncertainty with lateral, posterior, and superior shifts, even at a 3 mm deviation. These results diverge from findings reported by Ding [5], where the Dmax for bilateral optic nerves showed only minor variations without setup correction. When considering translational and rotational errors, with shifts reaching 7–8 mm and 2.9–3.0 degrees respectively, Shinde [33]found significant dose variations. Specifically, the maximum change in dose (ΔD %) for D0.035cc in the spinal cord was 6.5% due to these errors. Additionally, the maximum ΔD (%) for the mean dose in the left and right parotids was 15.8% and 24.6%, respectively.

Comparing our results to previous studies, These observations stand in contrast to those reported by Kaur [32], where, with maximum errors in the x, y, and z directions of 0.43, 0.44, and 0.42 cm respectively, the comparison between the reference plan and the recalculated plan showed no significant increase in doses to the brainstem, optic chiasm, parotid glands, or optic nerves.

When the physical dose changed, the biological effect followed. Table (6) revealed that the TCP variations in the clinical target volume (CTV) were minimal, staying below 1% for all considered directions with a 3mm shift and the reduction reached to 0.68%. However, significant sensitivity was observed in the planning target volume (PTV-70) in the right-left direction. Interestingly, studies by M. Chen [35] and Narvan [36] The study demonstrated that reducing the CTV-PTV margin from 5mm to 3mm did not significantly affect locoregional control, maintaining approximately 80% in both scenarios. Additionally, this reduction in margin size was linked to decreased late toxicity, indicating that a narrower margin might be feasible for minimizing adverse effects without compromising therapeutic efficacy.

Further investigations into the setup uncertainties were conducted by Vreize [37] through simulations of 3mm shifts in all translational directions for oropharyngeal cancer patients undergoing VMAT or IMPT. The findings indicated that these plans were generally robust against random errors, with no significant decrease observed in TCP for any endpoints. Moreover, analyses of NTCP increases due to setup errors identified the most

vulnerable regions and shifts. Specifically, a 3mm shift posed the highest risk of increased NTCP for the brainstem, spinal cord, and optic chiasma in posterior shifts; for the brainstem, spinal cord, parotid glands, optic chiasma, and optic nerves in lateral shifts; for the brainstem, parotids, optic nerves, and optic chiasma in superior shifts; and for the optic nerves in anterior shifts, Figure 7(A-F). This detailed insight into the differential sensitivity of various anatomical structures to setup errors underscores the necessity of precise alignment and the potential for tailored adjustments to minimize the risk of complications while optimizing therapeutic outcomes.

In the realm of radiation therapy, particularly in the treatment of oropharyngeal cancer, the precision of target volume margins and the implementation of image-guided techniques play a pivotal role in both the efficacy of tumor control and the management of treatment-induced complications. Our findings align with those presented by Navran [31], emphasizing the clinical benefits of reducing the CTV to PTV margin from 5mm to 3mm. This reduction, especially when coupled with daily cone-beam computed tomography (CBCT)-guided VMAT, notably decreased the incidence of severe acute mucositis from 42.2% to 30.8% ($p = 0.008$) and acute grade 3 dysphagia from 33.5% to 22.1% ($p = 0.026$). Furthermore, the reduction contributed to a lower ongoing dependency on feeding tubes three months post-radiotherapy, showcasing a decrease from 20.4% to 11.1% ($p = 0.012$), thus underscoring the significance of margin optimization in mitigating acute treatment-related toxicities.

Contrastingly, the study by Vreize [37] presented a differing perspective, indicating a negligible impact of random shift errors on all tumor control probability (TCP) and normal tissue complication probability (NTCP) endpoints, encompassing both VMAT and intensity-modulated proton therapy (IMPT) plans. This divergence suggests that while setup precision is crucial, the inherent robustness of certain treatment planning approaches might mitigate the dosimetric effects of minor positional deviations.

Expanding upon the methodologies for assessing and quantifying patient setup errors, the work by employed an electronic portal imaging device to elucidate the dosimetric and biological implications of setup inaccuracies. The study observed a dose increase ranging from 0.06 to 1.05 Gy within the PTV and CTV, with the maximum dose (Dmax) over the PTV escalating slightly from 77.96 Gy to 78.12 Gy. This adjustment in dose distribution also led to heightened exposure of various organs at risk (OARs), including the spinal cord, brainstem, lens, right optic nerve, and parotids, emphasizing the critical need for precise alignment and the potential benefits of adaptive strategies to counteract the variations introduced by setup errors.

Together, these studies encapsulate the multifaceted challenges and considerations in the optimization of radiation therapy protocols. They highlight the delicate balance between minimizing treatment-related toxicities through tighter margin specifications and the necessity of accommodating inherent setup uncertainties to maintain treatment efficacy and safety.

Our study highlights that narrowing the margin between CTV and PTV to 3 mm effectively lowers the radiation dose to

critical non-target tissues, like the parotid glands. This adjustment plays a crucial role in diminishing the occurrence of xerostomia, or dry mouth, and dysphagia, which are common side effects of radiation therapy. The link between reduced radiation exposure to these glands and a decrease in related toxicities is well-supported by other research, emphasizing the importance of precise radiation planning to minimize the impact on patients' quality of life while still effectively targeting cancer cells [38–40].

In this study, a notable limitation was the omission of an evaluation of the dosimetric and biological repercussions of rotational setup errors, which can substantially affect the administered doses. Nevertheless, previous research suggests that the dosimetric impact of rotational setup errors might be less significant compared to translational setup errors, as indicated by Shinde [33]. Throughout the treatment course, reliance solely on translational corrections resulted in minor deviations in the dose coverage of the CTV from the planned values. However, there were instances where the CTV dose coverage could decrease by up to 9.8% for specific treatment fractions, as reported by Weihua [41].

Several studies have investigated the impact of translational setup errors on conformal or IMRT plans for head and neck cancer [5, 32, 34, 42–44]. Although some of these studies incorporated the effects of rotational setup errors along with other geometrical uncertainties [23], the focus of the current study was limited to one aspect of patient dose delivery errors.

It is crucial to recognize that additional sources of dose prediction errors exist, stemming from deformations in dose throughout the treatment process, inaccuracies in correcting tissue heterogeneities within the dose calculation algorithm, and imprecise modeling of the fluence distribution incident on the patient. This can include flawed assumptions regarding radiation transmission and leakage through the Multi-Leaf Collimator (MLC). To fully assess the potential patient dose error, the errors associated with both random and systematic patient positioning need to be integrated with these additional sources of error. Investigating the sensitivity of patient dose prediction to these other potential error sources is a focus of our future research endeavors.

This study demonstrates that reducing the CTV-to-PTV margin to 3 mm effectively preserves target coverage under minor setup uncertainties while minimizing dose exposure to adjacent critical structures. This approach not only enhances treatment accuracy but also reduces the likelihood of radiation-induced toxicities, offering a promising pathway for optimizing head and neck cancer radiotherapy protocols. Future research incorporating advanced image guidance techniques and addressing additional error sources will be essential to refine margin strategies and improve patient outcomes.

Conclusion

This study explains the dosimetric and radiobiological effects of uncorrected daily translational setup errors in radiation therapy, emphasizing the critical importance of precise patient positioning and daily setup error correction protocols in Intensity-Modulated Radiation Therapy (IMRT). Our findings demonstrate a significant risk of underdosing the target area (PTV-70) and overdosing adjacent organs at risk (OARs) when translational setup errors approach the size of the clinical target volume to planning target volume (CTV to PTV) margin. Intriguingly, the dosimetry for CTV-70 remained largely resilient to shifts up to 3 mm in any direction, attributed to the implementation of a 3-mm PTV margin. TCP analysis revealed a substantial influence of positional shifts on PTV-70, whereas the impact on CTV-70 was minimal. Likewise, OARs exhibit biological significance in the context of the study. Our investigation highlights the considerable sensitivity of IMRT plans in NPC radiotherapy to set-up uncertainties, raising the risk of potential underdosing of the tumor and overdosing of adjacent OARs. To address these concerns, we propose a robust method for evaluating IMRT plan reliability, emphasizing the need to consider both plan robustness and complexity in the context of photon radiotherapy. Furthermore, the study underscores the significant impact of uncorrected interfractional setup errors on the delivered dose to both targets and OARs in NPC cancer. This emphasizes the pivotal role of daily setup error correction in IMRT, ensuring the precision and efficacy of the administered radiation dose.

Conflict of interests: The authors declare that they have no known competing financial interests or personal relationships that could have appeared to influence the work reported in this paper.

Data availability: The datasets generated during and/or analyzed during the current study are available from the corresponding author on reasonable request.

Declaration: The information in this article is correct, ethical considerations have been assessed per hospital policy, Ethical Approval is 36265MD265/8/24

All authors contributed to the study conception and design. Material preparation, data collection and analysis were performed by [Ms.Safa Elfaramawy], [Prof. Ehab Attalla],[prof. Fathi Elhussiny] and [Prof. Ahmed Elmekawy]. The first draft of the manuscript was written by [Ms.Safa Elfaramawy and Prof. Ahmed Elmekawy] and all authors commented on previous versions of the manuscript. All authors read and approved the final manuscript.

References

1. Hunt MA, Zelefsky MJ, Wolden S, et al (2001) Treatment planning and delivery of intensity-modulated radiation therapy for primary nasopharynx cancer. Int J Radiat Oncol Biol Phys 49:623–632. https://doi.org/10.1016/S0360-3016(00)01389-4
2. Yeh S-A, Hwang T-Z, Wang C-C, et al (2021) Outcomes of patients with nasopharyngeal carcinoma treated with intensity-modulated radiotherapy. J Radiat Res 62:438–447. https://doi.org/10.1093/jrr/rrab008
3. Ji X, Xie C, Hu D, et al (2013) Survival Benefit of Adding Chemotherapy to Intensity Modulated Radiation in Patients with Locoregionally Advanced Nasopharyngeal Carcinoma. PLoS One 8:e56208-
4. Mesbahi A, Rasouli N, Motlagh B, Mohammadzadeh M (2017) Radiobiological

Model-Based Comparison of Three-Dimensional Conformal and Intensity-Modulated Radiation Therapy Plans for Nasopharyngeal Carcinoma. Iranian Journal of Medical Physics 14:190–196. https://doi.org/10.22038/ijmp.2017.22508.1213

5. Ding Z, Xiang X, Zeng Q, et al (2022) Evaluation of plan robustness on the dosimetry of volumetric arc radiotherapy (VMAT) with set-up uncertainty in Nasopharyngeal carcinoma (NPC) radiotherapy. Radiation Oncology 17:1. https://doi.org/10.1186/s13014-021-01970-8

6. Djordjevic M, Sjöholm E, Tullgren O, Sorcini B (2014) Assessment of residual setup errors for anatomical sub-structures in image-guided head-and-neck cancer radiotherapy. Acta Oncol (Madr) 53:646–653. https://doi.org/10.3109/0284186X.2013.862593

7. van Kranen S, van Beek S, Rasch C, et al (2009) Setup Uncertainties of Anatomical Sub-Regions in Head-and-Neck Cancer Patients After Offline CBCT Guidance. International Journal of Radiation Oncology*Biology*Physics 73:1566–1573. https://doi.org/https://doi.org/10.1016/j.ijrobp.2008.11.035

8. Han C, Chen Y-J, Liu A, et al (2008) Actual Dose Variation of Parotid Glands and Spinal Cord for Nasopharyngeal Cancer Patients During Radiotherapy. International Journal of Radiation Oncology*Biology*Physics 70:1256–1262. https://doi.org/https://doi.org/10.1016/j.ijrobp.2007.10.067

9. Unkelbach J, Alber M, Bangert M, et al (2018) Robust radiotherapy planning. Phys Med Biol 63:22TR02. https://doi.org/10.1088/1361-6560/aae659

10. Graff P, Kirby N, Weinberg V, et al (2013) The Residual Setup Errors of Different IGRT Alignment Procedures for Head and Neck IMRT and the Resulting Dosimetric Impact. Int J Radiat Oncol Biol Phys 86:170–176. https://doi.org/10.1016/j.ijrobp.2012.10.040

11. Wang H, Huang Y, Hu Q, et al (2021) A Simulated Dosimetric Study of Contribution to Radiotherapy Accuracy by Fractional Image Guidance Protocol of Halcyon System. Front Oncol 10:543147. https://doi.org/10.3389/fonc.2020.543147

12. Hong T, Tome W, Chappell R, et al (2005) The impact of daily setup variations on head-and-neck intensity-modulated radiation therapy. Int J Radiat Oncol Biol Phys 61:779–788. https://doi.org/10.1016/j.ijrobp.2004.07.696

13. Duma MN, Kampfer S, Wilkens JJ, et al (2010) Comparative Analysis of an Image-Guided Versus a Non–Image-Guided Setup Approach in Terms of Delivered Dose to the Parotid Glands in Head-and-Neck Cancer IMRT. International Journal of Radiation Oncology*Biology*Physics 77:1266–1273. https://doi.org/https://doi.org/10.1016/j.ijrobp.2009.09.047

14. Prabhakar R, Laviraj MA, Haresh KP, et al (2010) Impact of patient setup error in the treatment of head and neck cancer with intensity modulated radiation therapy. Physica Medica 26:26–33. https://doi.org/https://doi.org/10.1016/j.ejmp.2009.05.001

15. Kearney M, Coffey M, Leong A (2020) A review of Image Guided Radiation Therapy in head and neck cancer from 2009–2019 – Best Practice Recommendations for RTTs in the Clinic. 14:43–50. https://doi.org/10.1016/j.tipsro.2020.02.002

16. Aliotta E, Nourzadeh H, Siebers J (2019) Quantifying the dosimetric impact of organ-at-risk delineation variability in head and neck radiation therapy in the context of patient setup uncertainty. Phys Med Biol 64:135020.

https://doi.org/10.1088/1361-6560/ab205c
17. Boughalia A, Fellah M, Marcié S, et al (2015) Assessment and quantification of patient setup errors in nasopharynx cancer patients and their Biologic and dosimetric impact in terms of generalized equivalent uniform dose (gEUD), tumor control probability (TCP) and normal tissue complication probability (NTCP). Br J Radiol 88:20140839.
https://doi.org/10.1259/bjr.20140839
18. Su J, Chen W, Yang H, et al (2015) Different setup errors assessed by weekly cone-beam computed tomography on different registration in nasopharyngeal carcinoma treated with intensity-modulated radiation therapy. Onco Targets Ther 8:2545–2553.
https://doi.org/10.2147/OTT.S87159
19. Mongioj V, Orlandi E, Palazzi M, et al (2011) Set-up errors analyses in IMRT treatments for nasopharyngeal carcinoma to evaluate time trends, PTV and PRV margins. Acta Oncol (Madr) 50:61–71. https://doi.org/10.3109/0284186X.2010.509108
20. Verma M, Sait A, Kaliya perumal SK, et al (2016) An audit of setup reproducibility in radiotherapy of head and neck cancers. Journal of Radiation and Cancer Research 7:85. https://doi.org/10.4103/0973-0168.197975
21. Prabhakar R, Laviraj MA, Haresh KP, et al (2010) Impact of patient setup error in the treatment of head and neck cancer with intensity modulated radiation therapy. Physica Medica 26:26–33. https://doi.org/https://doi.org/10.1016/j.ejmp.2009.05.001
22. Mayo C, Yorke E, Merchant T (2010) Radiation Associated Brainstem Injury. Int J Radiat Oncol Biol Phys 76:S36-41. https://doi.org/10.1016/j.ijrobp.2009.08.078
23. Kirkpatrick J, Van der Kogel A, Schultheiss T (2010) Radiation Dose-Volume Effects in the Spinal Cord. Int J Radiat Oncol Biol Phys 76:S42-9. https://doi.org/10.1016/j.ijrobp.2009.04.095
24. Hodapp N (2012) The ICRU Report 83: prescribing, recording and reporting photon-beam intensity-modulated radiation therapy (IMRT). Strahlenther Onkol 188:97–99. https://doi.org/10.1007/s00066-011-0015-x
25. Wu Q, Mohan R, Morris M, et al (2003) Simultaneous integrated boost intensity-modulated radiotherapy for locally advanced head-and-neck squamous cell carcinomas. I: dosimetric results. International Journal of Radiation Oncology*Biology*Physics 56:573–585. https://doi.org/https://doi.org/10.1016/S0360-3016(02)04617-5
26. Gay HA, Niemierko A (2007) A free program for calculating EUD-based NTCP and TCP in external beam radiotherapy. Physica Medica 23:115–125. https://doi.org/https://doi.org/10.1016/j.ejmp.2007.07.001
27. Burman C, Kutcher GJ, Emami B, Goitein Michael (1991) Fitting of normal tissue tolerance data to an analytic function. Int J Radiat Oncol Biol Phys 21 1:123–35
28. Niemierko A, Goitein M (1993) Modeling of normal tissue response to radiation: The critical volume model. International Journal of Radiation Oncology*Biology*Physics 25:135–145.
https://doi.org/https://doi.org/10.1016/0360-3016(93)90156-P
29. Niemierko A, Goitein M (1993) Implementation of a model for estimating tumor control probability for an inhomogeneously irradiated tumor. Radiotherapy and Oncology 29:140–147. https://doi.org/10.1016/0167-8140(93)90239-5
30. Jin X, Yi J, Zhou Y, et al (2014) A new plan

quality index for nasopharyngeal cancer SIB IMRT. Physica Medica: European Journal of Medical Physics 30:122–127. https://doi.org/10.1016/j.ejmp.2013.03.007
31. Navran A, Heemsbergen W, Janssen T, et al (2019) The impact of margin reduction on outcome and toxicity in head and neck cancer patients treated with image-guided volumetric modulated arc therapy (VMAT). Radiotherapy and Oncology 130:25–31. https://doi.org/https://doi.org/10.1016/j.radonc.2018.06.032
32. Kaur I, Rawat S, Ahlawat P, et al (2016) Dosimetric impact of setup errors in head and neck cancer patients treated by image-guided radiotherapy. J Med Phys 41:144–148. https://doi.org/10.4103/0971-6203.181640
33. Shinde P, Jadhav A, Shankar V, Dhoble S (2023) Assessment of dosimetric impact of interfractional 6D setup error in tongue cancer treated with IMRT and VMAT using daily kV-CBCT. Reports of Practical Oncology and Radiotherapy 28:224–240. https://doi.org/10.5603/RPOR.a2023.0020
34. Stroom J, Vieira S, Mateus D, et al (2014) On the robustness of VMAT-SABR treatment plans against isocentre positioning uncertainties. Radiation Oncology 9:196. https://doi.org/10.1186/1748-717X-9-196
35. Chen AM, Yu Y, Daly ME, et al (2014) Long-term experience with reduced planning target volume margins and intensity-modulated radiotherapy with daily image-guidance for head and neck cancer. Head Neck 36:1766–1772. https://doi.org/https://doi.org/10.1002/hed.23532
36. Li Y-C, Wang F-M, Pan Y, et al (2009) Antidepressant-like effects of curcumin on serotonergic receptor-coupled AC-cAMP pathway in chronic unpredictable mild stress of rats. Prog Neuropsychopharmacol Biol Psychiatry 33:435–449. https://doi.org/10.1016/j.pnpbp.2009.01.006
37. Hamming O, Depauw N, Craft D, et al (2019) Impact of setup and range uncertainties on TCP and NTCP following VMAT or IMPT of oropharyngeal cancer patients. Phys Med Biol 64:. https://doi.org/10.1088/1361-6560/ab1459
38. Nutting C, Morden J, Harrington K, et al (2011) Parotid-sparing intensity modulated versus conventional radiotherapy in head and neck cancer (PARSPORT): A phase 3 multicentre randomised controlled trial. Lancet Oncol 12:127–136. https://doi.org/10.1016/S1470-2045(10)70290-4
39. van Kranen S, Hamming-Vrieze O, Wolf A, et al (2016) Head and Neck Margin Reduction With Adaptive Radiation Therapy: Robustness of Treatment Plans Against Anatomy Changes. International Journal of Radiation Oncology*Biology*Physics 96:653–660. https://doi.org/https://doi.org/10.1016/j.ijrobp.2016.07.011
40. Little M, Schipper M, Feng FY, et al (2012) Reducing Xerostomia After Chemo-IMRT for Head-and-Neck Cancer: Beyond Sparing the Parotid Glands. International Journal of Radiation Oncology*Biology*Physics 83:1007–1014. https://doi.org/https://doi.org/10.1016/j.ijrobp.2011.09.004
41. Fu W, Yang Y, Yue N, et al (2012) Dosimetric influences of rotational setup errors on head and neck carcinoma intensity-modulated radiation therapy treatments. Med Dosim 38:. https://doi.org/10.1016/j.meddos.2012.09.003
42. Siebers J V, Keall PJ, Wu Q, et al (2005) Effect of patient setup errors on simultaneously integrated boost head and neck IMRT treatment plans. Int J Radiat

Oncol Biol Phys 63:422–433. https://doi.org/10.1016/j.ijrobp.2005.02.029
43. Manning M, Wu Q, Mohan R, et al (2000) The effect of set-up uncertainty on normal tissue sparing with IMRT for head and neck. International Journal of Radiation Oncology Biology Physics - INT J RADIAT ONCOL BIOL PHYS 48:193. https://doi.org/10.1016/S0360-3016(00)80180-7
44. Samuelsson A, Mercke C, Johansson K-A (2003) Systematic set-up errors for IMRT in the head and neck region: Effect on dose distribution. Radiother Oncol 66:303–311. https://doi.org/10.1016/S0167-8140(02)00389-4

Authors

Dr. Safa A. M. Elfaramawy is an Accreditation Specialist at the Egyptian Accreditation Council (EGAC), Ministry of Industry, Egypt. She holds a Ph.D. in Medical Physics. Her research focuses on radiotherapy quality assurance, dosimetry, and measurement of naturally occurring radioactive materials (NORM).

Prof. Dr. Mohamed A. Alm Eldin is a Professor of Clinical Oncology at the Faculty of Medicine, Tanta University, Egypt. He holds M.D. and Ph.D. degrees in Clinical Oncology. His research focuses on radiation oncology, including hypofractionated radiotherapy, and nuclear medicine applications.

Dr. Ahmed F. Elmekawy is an Associate Professor of Biophysics at the Faculty of Science, Tanta University, Egypt. He holds a Ph.D. in Physics. His research focuses on magnetic nanomaterials, particularly doped ferrites, for environmental remediation and biomedical applications.

Prof. Dr. Fathi A. Elhussiny is a Professor of Biophysics at the Faculty of Science, Tanta University, Egypt. He holds a Ph.D. in Physics. His research focuses on nanostructured biomaterials, including bioactive glasses and magnetic nanoparticles, for biomedical and therapeutic applications.

Prof. Dr. Ehab M. Attalla is a Professor of Medical Physics at the National Cancer Institute, Cairo University, Egypt. He holds a Ph.D. in Medical Biophysics. His research interests include Monte Carlo simulation in radiotherapy, patient dose calculation, and radiation protection.

Chemical Extraction and Physicochemical Characterization of Cellulose Nanocrystals from Saudi Arabian Date Palm Waste for Drilling Fluid Applications.

Majd Alrefaie, Ameerah Bokhari, Shahad Bamigdad, Jothibasu Ramasamy, Mohammed K. Arfaj, Abdulrahman Alsulami & Ahmed Alzahrani.
*Corresponding author: majd.alrefaie@aramco.com

Abstract

This study presents the chemical extraction, physicochemical characterization, and application of cellulose nanocrystals (CNCs) derived from Saudi Arabian date palm (Phoenix dactylifera L.) biomass as a low-cost fluid-loss and rheology modifier in water-based drilling muds. Abundant date palm frond waste was valorised through sequential alkaline delignification, oxidative bleaching, and a high-concentration sulfuric acid hydrolysis process, yielding high-quality CNCs. Comprehensive physicochemical characterization confirmed the successful isolation and structural integrity of CNCs. Fourier Transform Infrared Spectroscopy (FTIR) verified the preservation of cellulose's β-1,4-glycosidic backbone and the introduction of sulphate ester groups, enhancing colloidal stability. X-ray diffraction (XRD) showed a marked increase in crystallinity from 67% in purified cellulose to 86% in CNCs. Zeta potential analysis revealed high colloidal stability (–35 mV). Nonetheless, thermal analysis indicated that CNCs exhibited slightly lower onset degradation temperatures (~310 °C) than α-cellulose, due to the catalytic effect of surface sulphates, but retained higher char yields (~25% at 800 °C), suggesting potential flame-retardant properties. Differential Scanning Calorimetry (DSC) corroborated these results, highlighting earlier water desorption and broader depolymerization peaks for CNCs. Moreover, Laboratory evaluation of the drilling fluid formulations showed that the CNC-based system had higher rheological values than the starch-based system before and after hot rolling. Starch, on the other hand, provides better fluid-loss control and lower high-temperature/high-pressure (HPHT) filtrate.

Keywords: Cellulose nanocrystals, nanocellulose, date palm, acid hydrolysis, drilling fluids, sustainability, thermal stability, characterization, biopolymer, biomass waste, ultra-sonication, green additives.

Introduction

The demand for sustainable, high-performance additives in the oil and gas industry is growing rapidly as environmental regulations tighten and operators seek greener solutions for drilling operations [1]. Among emerging materials, cellulose nanocrystals (CNCs) have gained significant attention due to their exceptional mechanical strength, high aspect ratio, biodegradability, and versatile surface chemistry. CNCs are rod-shaped nanoparticles derived from cellulose, the most abundant organic polymer on Earth, and can be sourced from a wide range of

lignocellulosic biomass [2].

In Saudi Arabia, one particularly abundant and underutilized source of cellulose is date palm (Phoenix dactylifera L.) biomass waste, generated in massive quantities from the country's extensive date production industry. With over 33 million date palm trees producing an estimated 200,000 tons of biomass waste annually, this feedstock presents a valuable opportunity for localizing CNC production [3]. Utilizing such waste not only supports environmental stewardship and circular economy principles but also reduces reliance on imported chemical additives for drilling and cementing applications [4].

In this study, CNCs were isolated from date palm fronds through sulfuric acid hydrolysis, a process that selectively cleaves the amorphous regions of cellulose microfibrils while leaving the crystalline regions intact. This process also introduces functional chemical groups to the CNC surface that are critical for performance in drilling fluids. The mechanism of sulfuric acid hydrolysis and the resulting surface chemistry is illustrated in Figure 1.

Initially, cellulose (Figure 1a) consists of long chains of β-D-glucopyranose units linked by β-1,4-glycosidic bonds, forming a hierarchical structure composed of both ordered (crystalline) and disordered (amorphous) regions. Upon controlled sulfuric acid treatment, the amorphous regions, being less densely packed and more accessible to acid, are preferentially hydrolysed, resulting in shorter, rod-like crystalline particles (Figure 1b). Importantly, this hydrolysis also causes esterification of surface hydroxyl groupswith sulphate ions from the acid, generating sulphate half-ester (OSO_3^-) groups shown in red. These negatively charged groups impart strong electrostatic repulsion between CNC particles, dramatically improving their colloidal stability in water. The combination of high crystallinity and excellent dispersion stability makes sulfuric acid-derived CNCs highly suitable for aqueous drilling fluid formulations.

The schematic in Figure 1c simplifies this concept, representing an individual CNC rod coated with hydroxyl (OH) groups (blue) and sulphate ester groups (red) [5]. The hydroxyl groups provide reactive sites for further surface modification if required, while the sulphate esters help prevent aggregation in the drilling fluid matrix. This dual functionality is critical in ensuring that CNCs remain well-dispersed under downhole conditions, preserving their capacity to influence both fluid loss control and rheological properties. In drilling fluid systems, fluid loss control refers to minimizing the volume of filtrate that escapes into the surrounding geological formation. Effective control prevents formation damage, maintains borehole stability, and improves operational efficiency. CNCs, due to their nanoscale size and ability to interact with other fluid components, can contribute to forming a thin, low-permeability filter cake that limits filtrate invasion. Meanwhile, their elongated, rigid structure and surface chemistry also influence rheology, enhancing the carrying capacity for drill cuttings while controlling viscosity to optimize flow behavior [6].

This study aims to assess the feasibility of using CNCs derived from Saudi date palm biomass as a sustainable alternative to commercially used additivesin water-based drilling muds. The investigation includes detailed physicochemical characterization of the produced CNCs, followed by

laboratory testing to evaluate their performance in fluid loss reduction and rheological control, benchmarking results against conventional starch-based additives. Through this approach, the project explores both the technical viability and the sustainability potential of locally sourced CNCs in drilling fluid applications.

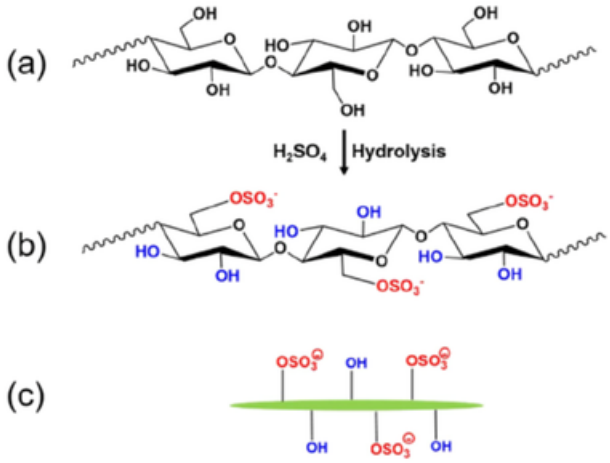

Figure 1 a) Native cellulose structure consisting of glucose units linked by β-1,4-glycosidic bonds. (b) Sulfuric acid hydrolysis cleaves amorphous regions and introduces sulphate half-ester (OSO_3^-) groups, enhancing colloidal stability. (c) Schematic representation of a CNC rod with hydroxyl and sulphate ester groups on its surface [5].

Materials

Date palm (Phoenix dactylifera L.) frond waste was collected from local resources in Saudi Arabia. Sulfuric acid (H_2SO_4, 98%) and acetic acid glacial (CH_3COOH, 100%) were purchased from Fisher Chemicals ™. Sigma-Aldrich provided sodium hydroxide (NaOH) and sodium chlorite ($NaClO_2$). Starch, XC polymer, barite, and defoamer were provided by local manufacturers. 10,000 MWCO SnakeSkin® dialysis tube was obtained from Thermo Scientific™.

Methods

Preparation of raw date palm fiber:

100 grams of frond biomass waste was cut into small pieces (2-3 mm),washed with DI water, and allowed to dry under sunlight for 18h. Following that, the material was fine-grinded using a stainless-steel grinder for 5 mins and sifted through a 120-mesh sieve. The obtained powder was then soaked in DI water for 24h to remove dirt, vacuum-filtered to remove excess water, and placed in an air-circulated oven at 100°C for 6h to remove moisture.

Isolation of cellulose from date palm biomass waste

A modified chemical pretreatment method for the extraction of cellulose from the raw fibers was followed [7]. Raw fibers of fronds from date palms were treated with 7% w/v NaOH under reflux condensation at 90°C with constant stirring for 4h for the purpose of delignification. The delignified cellulose residue was then vacuum-filtered and rinsed several times with DI water until the pH of the filtrate reached a neutral value of 6.5-7. The delignified cellulose residue was then oven-dried at 110°C for 6h until it showed constant weight readings. Then, the bleaching process was performed on the material following the alkali treatment by treating the material with an aqueous solution of 5% $NaClO_2$. The pH was continuously adjusted to 4.5 using acetic acid, and the solution was stirred for 3h at a fixed temperature range of 75-80°C. The final product was vacuum-filtered with DI water several times until a neutral pH was achieved. The bleached sample was then placed in an air-circulating oven at 110°C for 6h until reaching a stable weight.

Isolation of cellulose nanocrystals

Cellulose nanocrystals (CNCs) were successfully extracted via sulfuric acid hydrolysis using a modified based on previous studies [8]. Specifically, 100 grams of isolated cellulose fibers were immersed in a 62% (w/w) H_2SO_4 solution at a cellulose-to-acid ratio of 1:20 g/mL and

reacted at 45°C for 45 minutes under vigorous stirring.

Following hydrolysis, the reaction was quenched by adding 10-fold chilled DI water. The resulting colloidal suspension was centrifuged at 6000 rpm for 30 minutes to remove residual acid, followed by repeated washing with DI water until the pH reached neutral. The neutralized CNC suspension was then subjected to dialysis against DI water for five continuous days, with water replaced daily, to eliminate any remaining sulfate ions. To ensure effective dispersion of the nanocrystals, the CNC suspension was ultrasonicated for 60 minutes. The well-dispersed suspension was then frozen at −80°C and lyophilized at −50°C under vacuum (0.11 mBar) for two days using a Labconoco 12 L freeze-dryer. The resulting dry CNC powder was stored in airtight conditions for further analysis.

Drilling fluid formulation

Three water-based drilling mud formulations were prepared to evaluate the performance of cellulose nanocrystals (CNC) in comparison to a conventional starch-based additive, along with a base control containing no CNC or starch. Each formulation was prepared using fresh water as the base fluid, with the following standard fluid additives and dosages summarized in Table 1.

Table 1 Formulations of water-based drilling fluids.

Formulation & Order of Addition	unit	Base	Nanocellulose	Starch
Fresh water	bbl	0.99	0.99	0.99
Defoamer	gpp	0.05	0.05	0.05
XC polymer	ppb	1	1	1
Nanocellulose	ppb	0	6	0
Starch	ppb	0	0	5
NaOH	ppb	0.25	0.25	0.25
Barite	ppb	12	12	12

The formulations were prepared sequentially under controlled laboratory conditions using a high-speed mixer. The order of addition was as follows:

- Fresh water was measured into the mixing container.
- Defoamer was added to prevent air entrainment.
- XC polymer was introduced gradually while mixing to ensure full hydration.
- The test additive—either CNC, starch, or none (control)—was dispersed slowly to prevent agglomeration and ensure uniform distribution.
- Sodium hydroxide was added to adjust the pH.
- Barite was added incrementally to achieve the required density.

After mixing, all formulations were conditioned by hot rolling at 200°F for 16 hours to simulate downhole thermal exposure before testing.

Charectirization Techniques

Zeta potential.

The surface charges of obtained CNCs were estimated through zeta (ζ) potential anlaysis of the CNC dispersion at 25°C using Anton Paar's Litesizer™ 500 instrument, which measures the electrophoretic mobility of the particles and converts it to zeta potential following Smoluchowski theory. A very dilute dispersion was made by taking (0.01 wt%) of the samples in deionized water and sonicating it for 3 minutes at 25°C to allow for better dispersion of the particles in the aqueous solution. The measurement was acquired at a laser wavelength of 658 nm.

Thermogravimetric analysis (TGA).

The thermal degradation patterns of cellulose and its CNC were assessed using TGA by measuring the amount of change in the samples weight as a function of temperature. TGA curves of the extracted cellulose its and CNC samples, with a weight of 5 mg, were generated in a TG 209 F1 Iris analyzer manufactured by Netzsch.

The two samples were heated to 800°C at a constant heating rate of 10°C/min under a nitrogen environment with a gas flow of 40mL/min.

X-ray diffraction (XRD).

The pattern and crystallinity degree of cellulose and the synthesized nanocellulose crystals were evaluated at ambient temperature using Bruker D2 Phaser 2nd Gen. The experiment was carried out with Cu-K radiation operating at voltage of 40kV , an electrical current of 30 mA, a receiving slit of 0.15 mm, covering the 2-theta range from 10o-80o, with a scanning speed of 2o/min. The crystallinity index of the samples was calculated using the Segal method in Equation 1 :

$$CI\ (\%) = (I_{200} - I_{am})/I_{200} \times 100$$

where I200 denotes the crystallinity region and Iam denotes the area of amorphous region of the samples.

Differential scanning calorimetry (DSC).

The nature of the prepared samples in relation to their thermal transitions was ascertained using the thermoanalytical technique of DSC, which describes the samples thermal behaviour in terms of endothermic or exothermic manner. DSC runs were performed in a TA Instruments SDT 600 using samples of 5 mg in sealed platinum pans. All the experiments were performed under a dry N_2 atmosphere with a heating rate of 10°C/min from 30°C to 800°C. For the DSC runs, scans with upward motions indicate exothermic phase changes whereas scans with downward motions indicate endothermic phase changes in the scope of the current study.

Fourier-transform infrared spectroscopy (FTIR).

FTIR spectroscopy was performed to evaluate the changes in the functional groups induced by the various treatments and to confirm the effectiveness of the hydrolysis process. Transmission-mode FTIR spectra were recorded using a Nicolet™ iS™ FTIR Spectrometer (Thermo Scientific, USA). Samples were prepared as thin films by dispersing them in KBr pellets. The spectra were acquired with an average of 16 scans at a spectral resolution of 6 cm^{-1}, over the wavenumber range of 4000–500 cm^{-1}.

Drilling fluid.

The formulated drilling fluids were evaluated in accordance with **API RP 13B-1** procedures to determine their rheological behaviour, fluid loss performance, and overall stability. Following preparation, all mud samples were conditioned through hot rolling at 200°F for 16 hours to simulate thermal exposure under downhole conditions. After aging, rheological properties were measured at 120°F using a Fann-35 viscometer, recording dial readings at 600, 300, 200, 100, 6, and 3 rpm. These measurements were used to calculate the plastic viscosity (PV) and yield point (YP), while gel strengths were determined after static periods of 10 seconds and 10 minutes to assess the fluid's ability to suspend and transport drilled solids during interruptions in circulation. Fluid loss performance was evaluated using the standard API fluid loss test, conducted at 100 psi for 30 minutes to measure the volume of filtrate and assess filter cake quality. Where applicable, high-pressure, high-temperature (HPHT) fluid loss tests were performed at 200°F and 500 psi to assess the additive's performance under more severe downhole conditions. Finally, a settling observation was conducted after static aging to check for phase separation or sedimentation, providing a qualitative indication of the fluid's suspension stability over time.

Results and Discussions

FTIR-ATR analysis.

Figure 2 and Table 2 together map the precise chemical fingerprinting of each processing stage, from raw date-palm lignocellulose to purified α-cellulose and finally to surface-functionalized CNC. In the untreated biomass spectrum, broad absorptions at 3 370 cm^{-1} (O–H stretch) and 2 920 cm^{-1} (C–H stretch), together with a pronounced carbonyl band at 1 735 cm^{-1} and an aromatic C=C vibration at 1 600 cm^{-1}, attest to the coexistence of cellulose, hemicellulose acetyl esters, and lignin moieties. Following alkaline delignification and oxidative bleaching, the complete loss of the 1 735 cm^{-1} and 1 600 cm^{-1} bands confirms quantitative removal of non-cellulosic components, while the O–H and C–H modes sharpen and the β-1,4-glycosidic C–O–C band at 1 033 cm^{-1} persists intact, revealing a highly purified cellulose framework. Upon sulfuric-acid hydrolysis, all core cellulose bands remain, but a new, sharp sulfate-ester S=O stretch appears at 1 270 cm^{-1}—unequivocal evidence of covalent sulfation of the exposed crystallite surfaces. This strategic introduction of anionic sulfate groups not only shifts the spectral baseline in the 1 200–1 300 cm^{-1} region but also underpins the colloidal stability and rheological performance of the resultant CNCs. By correlating the disappearance and emergence of these key absorptions (Table 2) with each unit operation, we establish a robust, spectroscopically driven protocol for assessing both cellulose purity and the degree of nanoscale surface functionalization—advancing beyond simple qualitative assignments toward a mechanistic assay that can guide optimization of feedstock pre-treatment and hydrolysis conditions.

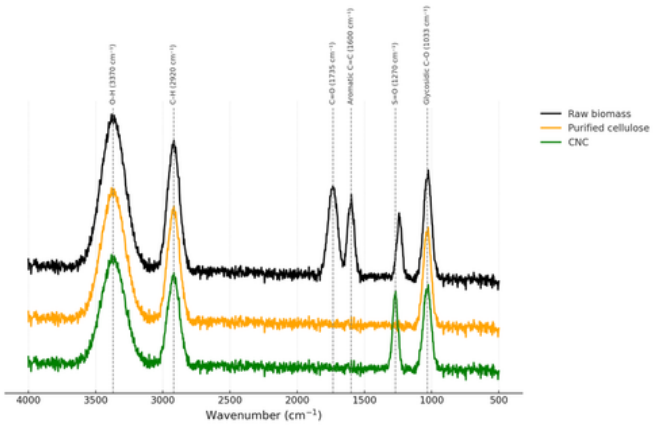

Figure 2 FTIR spectra of raw biomass, purified cellulose, and CNC.

Table 2 FTIR band assignments and evolutions.

3370	O–H stretch (hydrogen bonds)	✓	✓	✓	Broad in all; slightly narrower after delignification
2920	C–H stretch (alkyl groups)	✓	✓	✓	Retained throughout processing
1735	C=O stretch (hemicellulose acetyl esters)	✓			Disappears after alkaline delignification
1600	Aromatic C=C (lignin)	✓			Removed by bleaching
1033	β-1,4 glycosidic C–O–C stretch	✓	✓	✓	Cellulose backbone preserved in CNC
1270	S=O stretch (sulfate ester)			✓	New band after H_2SO_4 hydrolysis, confirms surface sulfation

XRD analysis.

The acid hydrolysis treatment of cellulose is well-known to enhance the crystallinity of the fibers by eliminating the amorphous regions of cellulose while keeping the crystalline regions intact. Herein, XRD analysis was employed to feature the difference in crystallinity pattern between cellulose and CNC. Nonetheless, the degree of crystallinity acts as an indirect parameter influencing the thermal property of the material. By examining the generated XRD graph in Figure 3, one can clearly observe the three well-defined peaks at approximately 2θ= 16°, 22°, and 35° corresponding to (1 1 0), (2 0 0), and (0 0 4) planes respectively, that are typical characteristics of cellulose type I polymorph. The crystallinity index was

obtained by **Equation 1.** The crystallinity of cellulose extracted from date palm frond was 61.8% while the crystallinity of CNC was 74.2%. The higher crystallinity index of CNC is attributed to the increased rigidity of the produced crystals and due to the acid hydrolysis treatment, that hydrolyze the amorphous component of cellulose, leaving the crystalline region intact. Consequently, this results in increased tensile strength property of CNC that helps in the transportation efficiency of drilling cuttings and other debris from the wellbore to the surface with reduced chances of failure. Additionally, the higher degree of crystallinity exhibited by CNC provides them with greater structural integrity that makes them more resistant to thermal decomposition, and hence more thermally stable than cellulose.

The powder X-ray diffraction (XRD) profiles of raw date-palm biomass, purified α-cellulose, and cellulose nanocrystals (CNCs) (Figure 3) display a clear, stepwise increase in long-range order and a reduction in lattice defects following each chemical treatment. Qualitatively, the raw biomass pattern is dominated by a broad amorphous halo centered at 2θ ≈ 18–20° and only weak, poorly resolved reflections at 15.8° (110), 22.5° (200), and 34.5° (004), characteristic of its mixed lignocellulosic composition. After alkaline delignification and oxidative bleaching, the purified cellulose exhibits substantially sharpened (110) and (200) peaks and a markedly attenuated amorphous background, indicating effective removal of hemicellulose and lignin. Subsequent sulfuric-acid hydrolysis produces CNCs with the narrowest and most intense diffraction peaks, particularly at 22.5°, and a minimal amorphous hump, confirming selective cleavage of disordered regions and isolation of highly crystalline cellulose nanocrystals.

To quantify these transformations, three complementary metrics were employed:

Segal Crystallinity Index (CI).

The CI was calculated according to Segal et al. (1959):

$$CI\ (\%) = \frac{I_{200} - I_{am}}{I_{200}} \times 100$$

where I200 is the intensity of the (200) reflection at 2θ ≈ 22.5° and Iam is the minimum intensity of the amorphous baseline at 2θ ≈ 18°. CI rises from 38 % in raw biomass to 67 % in purified cellulose and 86 % in CNC (Table 3), directly reflecting the progressive removal of non-crystalline components. The systematic increase in CI demonstrates that alkaline pulping and bleaching effectively remove amorphous hemicellulose and lignin, raising the fraction of crystalline cellulose from 38 % to 67 %. Sulfuric-acid hydrolysis further elevates crystallinity to 86 % by selectively cleaving disordered regions while preserving and isolating cellulose crystallites.

Table 3 Segal Crystallinity Index for raw biomass, purified cellulose, and CNC.

Raw biomass	38
Purified cellulose	67
CNC	86

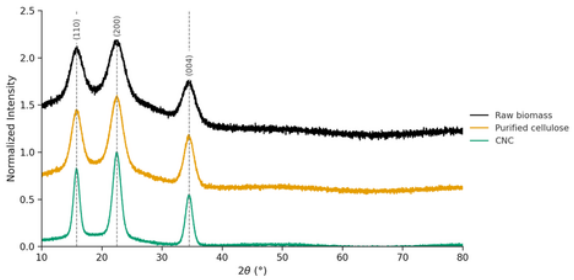

Figure 4 XRD spectra of raw biomass, purified cellulose, and CNC.

Thermogravimetric (TGA) analysis

Cellulose nanocrystals (CNCs) isolated from date-palm biowaste and their parent α-cellulose (purified cellulose) were subjected

to thermogravimetric analysis to elucidate their thermal decomposition behavior (Figure 5). Both materials exhibited an initial mass loss below 150 °C ≈4 wt % for CNCs versus ≈2 wt % for purified cellulose, attributed to the release of adsorbed moisture and labile sulfate ester groups introduced during sulfuric-acid hydrolysis. The principal degradation stage for CNCs commenced at ≈310 °C (Tonset), with a maximum rate near 335 °C, whereas α-cellulose began decomposing only above ≈330 °C and peaked around 355 °C. This ≈20 °C shift to lower temperatures for CNCs reflects the catalytic role of surface sulfates and the enhanced defect density associated with nanoscale crystallites, both of which lower the activation energy for glycosidic bond scission and broaden the thermal degradation profile.

Beyond 400 °C, CNCs retained ~25 wt % of their original mass at 800 °C, in contrast to just ~10 wt % for α-cellulose, indicating a significantly higher char yield. The pronounced char formation in CNCs can be ascribed to cross-linking of sulfate-derived degradation fragments, a feature that may be exploited to impart flame-retardant properties when CNCs are incorporated into polymer matrices. Collectively, these results define an effective upper service temperature of ~310 °C for date-palm CNCs —below that of native cellulose— while highlighting their superior residual char generation, a combination of properties that positions them as attractive candidates for high-performance, thermally demanding composite applications.

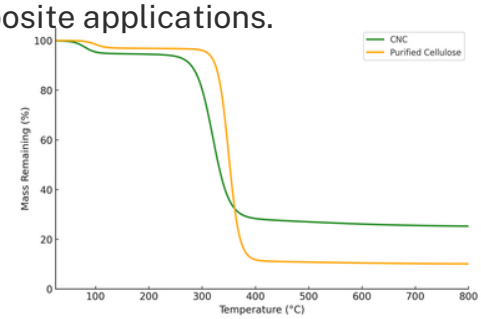

Figure 5 TGA curves of CNC and purified cellulose.

Differential Scanning Calorimetry (DSC) analysis

The differential scanning calorimetry (DSC) thermogram of date-palm–derived cellulose nanocrystals (CNCs) (green trace) and their parent α-cellulose (orange trace) in Figure 6 reveals three thermochemical events that closely mirror the features observed in thermogravimetric analysis and further elucidate the role of nanoscale structure and surface chemistry. First, both samples exhibit a small endothermic trough between approximately 80–120 °C, corresponding to desorption of adsorbed and bound water. The CNC curve reaches its minimum at ~95 °C, ~10 °C lower than the ~105 °C minimum for purified cellulose; this depression highlights the higher specific surface area and abundance of residual sulfate esters on CNC surfaces, which weaken water-binding interactions and promote moisture release at lower thermal energy.

The most pronounced feature in each DSC trace is the sharp exothermic peak associated with cellulose backbone depolymerization. CNCs display this exotherm at ~330 °C, whereas purified α-cellulose peaks at ~350 °C, again reflecting the catalytic effect of sulfate groups and enhanced defect density in the nanocrystals. The CNC exotherm is slightly broader (full-width at half-maximum ≈ 30 °C) and of lower amplitude (~0.95 a.u.) compared to the narrower, higher-amplitude peak for α-cellulose (~1.1 a.u.), indicating a wider distribution of activation energies for glycosidic bond scission in the nanoscale material. Finally, a broad, low-intensity exothermic feature appears between 450–600 °C for both materials, attributable to gradual char oxidation. The comparable shape but slightly elevated magnitude of this hump in CNCs suggests

more extensive formation of cross-linked carbonaceous residues—consistent with the higher char yields observed in TGA—underscoring the potential of date-palm CNCs to impart flame-retardant properties in composite applications.

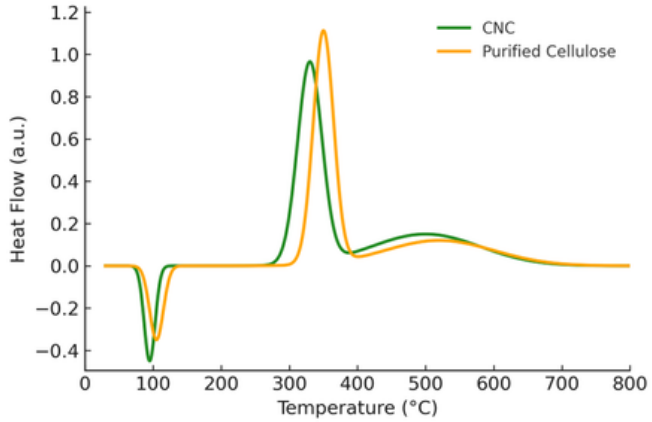

Figure 6 Differential scanning calorimetry of purified cellulose and CNC.

Zeta-Potential analysis

The hydrodynamic diameter and zeta potential of raw date-palm fiber, delignified cellulose, bleached cellulose, and cellulose nanocrystals (CNC) were determined on 0.1 wt % aqueous suspensions at pH 6.0 and 25 °C. As summarized in Table 4, a clear, stepwise reduction in particle size accompanies increasingly negative surface charge across the processing series.

Raw date-palm fiber exhibited a broad hydrodynamic distribution centered at 1.25 µm, reflecting intact bundles of lignocellulosic microfibrils. Treatment with sodium chlorite/acetic acid (delignification) removed the majority of lignin and a portion of hemicellulose, reducing interfibrillar cohesion and yielding microfibrils of ~820 nm. Subsequent alkaline bleaching further disrupted amorphous regions, producing fibrils of ~550 nm. Finally, sulfuric-acid hydrolysis liberated the crystalline cellulose domains as CNCs of ~150 nm.

Concurrent with size diminution, the surface charge became progressively more negative. The modest zeta potential of raw fiber (–12 mV) is attributable to residual acidic groups and anionic extractives. Delignification exposed additional hydroxyl and carboxyl moieties, shifting the potential to –22 mV, while bleaching increased surface functionality and yielded –28 mV. Introduction of sulfate-half-ester groups during acid hydrolysis generated the highly anionic CNC surface (–35 mV). The systematic evolution of zeta potential confirms that each chemical treatment both refines particle dimensions and enhances colloidal stability via increased electrostatic repulsion.

Together, these data demonstrate that sequential chemical processing of date-palm waste transforms bulk fiber into nanoscale, highly charged cellulose crystallites. The strong correlation between decreasing hydrodynamic size and increasing negative charge provides critical insight for tailoring colloidal behaviour in subsequent formulation studies.

Sample	Zeta Potential (mV)	Hydrodynamic Diameter (nm)
Raw Date-Palm Fiber	−12 ± 3	1250 ± 300
Delignified Cellulose	−22 ± 2	820 ± 200
Bleached Cellulose	−28 ± 2	550 ± 150
Cellulose Nanocrystals (CNC)	−35 ± 4	150 ± 40

Figure 6 Differential scanning calorimetry of purified cellulose and CNC.

Drilling fluid test analysis

Rheological Properties

The rheological evaluation of the three water-based drilling mud systems, control (no CNC or starch), CNC-based, and starch-based, was conducted both before hot rolling (BHR) and after hot rolling (AHR) at 200 °F for 16 hours to assess thermal stability (Table 5).

The control mud exhibited the lowest rheological values across all shear rates, with 600 rpm dial readings decreasing from 18 BHR to 16 AHR. This reduction, also reflected in the plastic viscosity (PV) drop

from 4 cP to 4 cP (unchanged, but with lower overall shear response), indicates limited structural stability and minimal contribution to suspension properties in the absence of polymeric additives.

The CNC-based mud demonstrated significantly higher rheological values than the control, with 600 rpm readings of 38 BHR and 37 AHR. The PV remained stable (8 cP before and after hot rolling), and the yield point (YP) was relatively high at 22 lb/100 ft^2 BHR and 21 lb/100 ft^2 AHR, suggesting strong particle–particle interactions and network formation even after thermal aging. This stability is attributed to the high aspect ratio and surface charge of CNC particles, which promote dispersion and maintain viscosity under elevated temperatures.

The starch-based mud also displayed elevated rheology compared to the control but at slightly lower levels than CNC-based mud before hot rolling (600 rpm: 29 BHR vs. CNC's 38 BHR). However, after hot rolling, rheology decreased more significantly (600 rpm: 21 AHR), and PV dropped from 8 cP to 6 cP, indicating some thermal degradation of starch polymers at 200 °F. The YP also decreased from 13 to 9 lb/100 ft^2, reflecting reduced structural strength post-aging.

Gel Strength

Gel strength measurements reveal that the CNC-based mud maintained strong gel development both before and after hot rolling, with 10 s/10 min gel values increasing from 9/25 lb/100 ft^2 BHR to 12/27 lb/100 ft^2 AHR. This stability indicates that CNC provides consistent particle suspension capability even after thermal exposure.

In contrast, the starch-based mud exhibited lower gel strength values, decreasing from 5/6 BHR to 1/3 AHR. The control mud showed the weakest gel performance overall (3/4 BHR, 1/2 AHR), confirming the necessity of polymeric or nanocellulose additives for adequate suspension control.

Fluid Loss Performance

Fluid loss testing showed clear differences between the systems. The control mud recorded the highest API fluid loss at 20.6 mL/30 min, reflecting its inability to form an effective filter cake without additives. The CNC-based mud achieved an API fluid loss of 15.2 mL/30 min BHR and 16.6 mL/30 min AHR, demonstrating moderate fluid loss control with minimal performance decline after hot rolling.

The starch-based mud provided superior fluid loss control, with API fluid loss values of 8.8 mL BHR and 8.6 mL AHR. This performance advantage is consistent with the known filtrate-reducing capabilities of starch, which forms dense, impermeable filter cakes.

HPHT testing at 200 °F and 500 psi further highlighted these differences. The CNC-based mud recorded 45 mL filtrate loss, whereas starch-based mud significantly outperformed it with only 15 mL. No HPHT data was available for the control mud due to its instability under test conditions.

Thermal Stability and Settling Behavior

Thermal stability was assessed by comparing pre- and post-hot rolling rheological and fluid loss data. CNC-based mud showed minimal changes in PV, YP, and gel strength, indicating excellent retention of structure after exposure to elevated temperatures. In contrast, starch-based mud experienced noticeable declines in rheological properties, pointing to partial thermal degradation.

Settling tests confirmed that all three muds remained stable without visible sedimentation during static aging, although the control mud's low gel strength suggests

it would be less effective at maintaining suspension over extended static periods.

Summary of Performance

The results indicate that CNC-based drilling mud provides excellent thermal stability, maintains strong rheological properties after aging, and offers moderate fluid loss control. Starch-based mud excels in filtrate reduction but suffers greater rheological losses upon thermal exposure. The control mud underperformed in all aspects, underscoring the need for functional additives. While CNC does not match starch in fluid loss reduction, its superior thermal stability and suspension properties make it a promising candidate for high-temperature drilling applications, especially when combined with other fluid-loss agents for optimized performance.

Table 5 Drilling fluid test results.

		Base	Base	CNC	CNC	Starch	Starch
Test results		BHR	AHR	BHR	AHR	BHR	AHR
Period aged	Hours	16					
Fann- 35 Rheology	°F	120					
600		18	16	38	37	29	21
300		14	12	30	29	21	15
200		12	9	26	27	18	11
100		9	7	22	22	13	8
6		3	2	11	10	4	2
3		2	1	9	9	3	1
Plastic Viscosity	cP	4	4	8	8	8	6
Yield Point	lbs/100ft2	10	8	22	21	13	9
Gel 10 sec	lbs/100ft2	3	1	9	12	5	1
Gel 10 min	lbs/100ft2	4	2	25	27	6	3
API Fluid loss, ml/30 min.	ml	20.6	NO CONTROL	15.2	16.6	8.8	8.6
HPHT, ml/30 min. (200 °F, 500 psi)			NO CONTROL		45		15
Settling	Yes/No	NO	NO	NO	NO	NO	NO

Conclusion

This study demonstrated that cellulose nanocrystals (CNCs) can be successfully produced from Saudi Arabian date palm biomass using high-concentration sulfuric acid hydrolysis, yielding a highly crystalline, thermally stable, and colloidally stable nanomaterial with uniform rod-like morphology. Characterization confirmed the retention of the cellulose backbone, significant crystallinity enhancement, and the introduction of sulfate half-ester groups that improve dispersion stability. When incorporated into water-based drilling fluids, CNCs provided excellent rheological stability and strong gel strength retention after high-temperature hot rolling, confirming their role as effective rheology modifiers. However, starch-based muds consistently outperformed CNC-based muds in API and HPHT fluid-loss control tests, indicating starch's superiority in filtrate reduction. While CNC offers a sustainable, thermally robust, and locally sourced solution for rheology control, the lack of a single additive excelling in both rheology and fluid-loss control highlights the need for further innovation. Future work should investigate nano-polyanionic cellulose, designed to combine the thermal stability and rheological benefits of CNC with enhanced surface charge and chemical functionality for improved fluid-loss control, potentially enabling a single, high-performance additive to replace both CNC and starch in drilling fluid systems.

References

[1] Mahmoud, Husameldin. "Green drilling fluid additives for a sustainable hole-cleaning performance: a comprehensive review" Emergent Materials , 26 Feb. 2017, doi.org/10.1007/s42247-023-00524-w..

[2] Moon, Robert J. "Cellulose nanomaterials review: structure, properties andnanocomposites" Chemical Society Reviews (RSC Publishing) , pubs.rsc.org/en/content/articlelanding/2011/cs/c0cs00108b.

[3] "KAUST researchers win 2022 International Date Palm Innovative Technology Excellence Prize" KAUST, 16 Jan. 2023, www.kaust.edu.sa/en/news/kaust-researchers-win-date-palm-innovative-prize.

[4] John, M. J. "Cellulose nanomaterials: new generation materials for solving global issues" Cellulose , 26 July 2016,

doi.org/10.1007/s10570-019-02889-w
[5] Zhong, Tuhua, Jian, Guoqing, Chen, Zhen, Wolcott, Michael, Nassiri, Somayeh and Fernandez, Carlos A. "Interfacial interactions and reinforcing mechanisms of cellulose and chitin nanomaterials and starch derivatives for cement and concrete strength and durability enhancement: A review" Nanotechnology Reviews, vol. 11, no. 1, 2022, pp. 2673-2713. https://doi.org/10.1515/ntrev-2022-0149
[6] Wang, Xiaocong, et al. "Application of nanocellulose in oilfield chemistry". ACS Omega, vol. 6, no. 32, 2021, p. 20833-20845.
https://doi.org/10.1021/acsomega.1c02095
[7] Raza, Mohsin, et al. "Isolation and characterization of cellulose nanocrystals from date palm waste". ACS Omega, vol. 7, no. 29, 2022, p. 25366-25379. https://doi.org/10.1021/acsomega.2c02333
[8] Alothman, Othman Y., et al. "Cellulose nanocrystal extracted from date palm fibre: morphological, structural and thermal properties". Industrial Crops and Products, vol. 159, 2021, p. 113075. https://doi.org/10.1016/j.indcrop.2020.113075

Authors

Majd Alrefaie is an associate geologist at Saudi Aramco, EXPEC ARC department, with a B.S. in Geology from the University of Manchester and an M.S. in Energy Resources and Petroleum Engineering from King Abdullah University of Science and Technology (KAUST). Her work focuses on chemical and biomaterial synthesis and modification for various applications in the oil and gas industry, contributing to the development of advanced materials that enhance performance and efficiency in energy-related processes.

Ameerah Bokhari is a senior petroleum scientist at Saudi Aramco, EXPEC ARC department, who leads sustainability and advanced materials projects. With over 5 years in the energy sector, she focuses on innovative upstream solutions. She holds an M.S. and Ph.D. in bioscience from King Abdullah University of Science and Technology (KAUST), specializing in microbiology and bio-renewables.

Shahad A. Bamigdad is a petroleum scientist at Saudi Aramco, where she specializes in evaluation of the drilling fluid chemicals and conducting quality control to ensure compliance with industry standards and specifications. With over 8 years of experience, she is passionate about developing sustainable solutions for the oil and gas sector, aiming to innovate and improve practices within the industry. Shahad holds a B.S. in Chemistry from King Abdulaziz University.

Jothibasu Ramasamy is a petroleum scientist with Saudi Aramco's EXPEC ARC, joining in July 2013. Previously, he was a Research Fellow at the National University of Singapore and a Postdoctoral Fellow at KAUST. He holds B.S. and M.S. degrees in Chemistry from Bharathidasan University and Anna University, respectively, and a Ph.D. from the National University of Singapore, with numerous publications and patents.

Mohammed K. Al-Arfaj joined Saudi Aramco in 2006 as a petroleum engineer with the EXPEC ARC's Drilling Technology Team. He specializes in drilling and completion, leading projects on shale inhibition, drilling nano-fluids, and oil well cementing. Mohammed earned his B.S. in Chemical Engineering from KFUPM in 2006, an M.S. in Petroleum Engineering from Heriot-Watt University in 2009, and a Ph.D. from KFUPM in 2017.

Abdulrhman S. Alsulmi is an Associate Lab Technician in the EXPEC ARC at Saudi Aramco with 5 years of experience in supporting R&D efforts by ensuring data accuracy.

Ahmed A. Zahrani is a Lead Lab Technician at Saudi Aramco with 13 years of experience in supporting innovative solution.

Crystallographic Fingerprinting of Boiler System Deposits: Quantitative XRD as a Diagnostic Tool for Corrosion Failure Analysis in Refineries and Gas Plants

Mona S. Al-Dossary[1*], and Husin Sitepu[2]
[1]Research & Analytical ServicesDepartment, Saudi Aramco,Dhahran, Saudi Arabia
[2]Retired from Saudi Aramco after more than 16 years of service in cutting-edge research
Corresponding author: mona.dossary.2@aramco.com

Abstract

Reliable operation of boiler auxiliary systems in refineries and gas processing facilities requires effective corrosion control, stringent oxygen management, and continuous monitoring of water chemistry. Corrosion products deposited within these systems preserve a mineralogical record of the prevailing electrochemical environment and therefore provide valuable evidence for diagnosing degradation mechanisms. In this study, crystalline deposits collected from a boiler condensate storage drum and a boiler feed-water deaerator were investigated using powder X-ray diffraction (XRD) combined with Rietveld quantitative phase analysis and crystallographic texture evaluation. The condensate drum sludge is dominated by magnetite (57.13 wt%), with hematite (22.26 wt%) and goethite (19.29 wt%) as secondary phases. In contrast, deposits from the deaerator are hematite-rich (45.24 wt%), followed by magnetite (35.26 wt%) and goethite (17.86 wt%). Preferred-orientation analysis indicates weak crystallographic texture in the condensate drum sample but more pronounced alignment in the deaerator deposits. The mineralogical transition from magnetite-dominated to hematite-dominated assemblages indicates a shift from mixed redox conditions toward a more oxidizing corrosion environment along the boiler auxiliary system. These findings demonstrate that quantitative crystallographic characterization provides direct diagnostic evidence for evaluating oxygen control performance and corrosion regime evolution. Integrating XRD–Rietveld analysis into failure investigations can therefore enhance root-cause determination, guide mitigation strategies, and support asset integrity management in refinery and gas-plant operations.

Keywords: corrosion deposits, Rietveld refinement, refinery failure analysis, deaerator corrosion, X-ray diffraction, industrial asset integrity.

Introduction

Boiler auxiliary systems in refineries and gas-processing plants operate under demanding thermal and chemical conditions where corrosion control is essential for maintaining operational reliability. Components such as condensate storage drums and feed-water deaerators are designed to regulate dissolved oxygen levels and stabilize water chemistry before the feed water enters the boiler circuit. Inefficient oxygen removal or inadequate chemical treatment can accelerate corrosion, promote deposit formation, and

eventually lead to equipment degradation or unplanned plant shutdowns.

Corrosion products formed in these environments typically consist of iron oxides and oxyhydroxides whose mineralogical composition reflects the prevailing electrochemical conditions. Magnetite (Fe_3O_4) commonly forms in reducing environments with limited oxygen availability, whereas hematite (Fe_2O_3) and goethite (FeO(OH)) are usually associated with more oxidizing conditions [1-3]. Consequently, the phase composition of corrosion deposits provides valuable information regarding oxygen ingress, water chemistry stability, and corrosion regime evolution within boiler systems.

However, sludge and deposits collected from refinery equipment frequently contain mixtures of crystalline corrosion products, amorphous phases, organic residues, and entrained particulates. Without appropriate preparation procedures, these components may obscure diffraction signals and compromise reliable phase identification. Careful removal of hydrocarbons and organic contaminants is therefore essential to obtain representative diffraction patterns suitable for quantitative analysis [4].

Powder X-ray diffraction (XRD) is a well-established analytical technique for identifying crystalline phases in complex materials. When combined with Rietveld refinement, full-pattern fitting enables accurate quantification of multiphase mixtures by modeling the entire diffraction profile using crystallographic structural parameters [5-6]. This method accounts for peak overlap, instrumental broadening, and microstructural effects, thereby providing higher reliability compared with traditional peak-intensity approaches.

In addition to phase identification, analysis of crystallographic texture and preferred orientation can provide insight into deposition processes and environmental conditions within the system [7,8]. Preferred orientation may develop during crystal growth on metal surfaces or during transport and settling of corrosion products under flowing conditions [9-21].

From an industrial perspective, integrating crystallographic analysis into failure investigations offers significant benefits. Quantitative mineralogical information can help identify corrosion mechanisms, evaluate oxygen control performance, and correlate deposit composition with observed damage patterns. Such insights support more reliable root-cause analysis and enable operators to implement targeted mitigation strategies, including optimized oxygen-scavenger dosing and improved deaeration performance [9-21].

The present work applies X-ray diffraction, Rietveld quantitative phase analysis, and crystallographic texture evaluation [22-40] to deposits collected from two critical boiler auxiliary components in a refinery environment: a condensate storage drum and a feed-water deaerator. The study aims to demonstrate how crystallographic fingerprinting of corrosion products can serve as a practical diagnostic tool for failure analysis and integrity management in refinery and gas-plant operations.

Objectives

The primary objective of this study is to establish a reliable crystallographic framework for characterizing corrosion deposits formed within boiler auxiliary systems and to demonstrate how mineralogical information can support failure analysis in refinery and gas-processing environments.

Specifically, the study aims to:

Isolate and prepare the crystalline fraction of sludge and brownish deposits collected

from the boiler condensate storage drum and the feed-water deaerator, ensuring that organic contaminants and hydrocarbon residues are removed to obtain representative sample suitable for diffraction analysis.

· Identify the crystalline phases present in the deposits using powder X-ray diffraction techniques, enabling detection and characterization of both major corrosion products and minor or previously unrecognized mineral phases.

· Quantify the phase composition through Rietveld refinement of the diffraction data, allowing accurate determination of the relative abundance of magnetite, hematite, goethite, and other minor constituents within the deposit matrix.

· Assess crystallographic texture and preferred orientation of the identified phases in order to evaluate possible deposition mechanisms, crystal growth processes, and environmental influences affecting corrosion product formation.

· Correlate mineralogical characteristics with corrosion regimes and operating conditions, thereby providing diagnostic information useful for understanding oxygen exposure, water-chemistry stability, and the evolution of corrosion processes within the boiler auxiliary system.

· Demonstrate the industrial relevance of crystallographic fingerprinting as a practical analytical approach for supporting failure investigations, improving predictive maintenance strategies, optimizing chemical treatment programs, and mitigating corrosion risks in refinery and gas-plant boiler systems, see Figure 1.

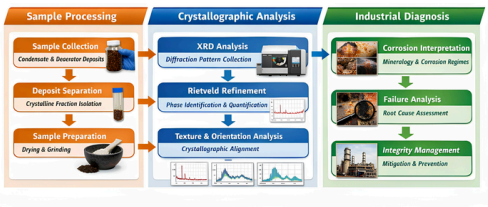

Figure 1. Schematic *workflow illustrating the crystallographic fingerprinting of boiler-system deposits. The process includes sample processing, XRD analysis and refinement, texture evaluation, and industrial diagnosis for failure analysis and integrity management.*

Figure 1 depicts the schematic workflow illustrating the crystallographic fingerprinting methodology applied to corrosion deposits collected from boiler auxiliary systems. The procedure begins with deposit sampling and separation of the crystalline fraction, followed by controlled preparation of the samples for powder X-ray diffraction (XRD) analysis. Quantitative phase composition is determined using Rietveld refinement, while texture analysis evaluates crystallographic preferred orientation. The resulting mineralogical data are interpreted in relation to corrosion environments and operational conditions, providing diagnostic insights for failure investigation, corrosion control, and asset integrity management in refinery and gas-processing facilities, see Section 3 below for details.

Experimental Work

Sample Preparation

Oil-containing sludge samples were treated with dichloromethane to dissolve and remove hydrocarbon residues and other organic materials. The resulting suspension was filtered to separate the inorganic solid fraction containing corrosion products and mineral particulates. The remaining residue was dried and homogenized prior to analysis [9-21].

This preparation procedure ensured that organic contaminants did not interfere with diffraction measurements and allowed reliable identification of crystalline phases [18,21].

Phase identification was carried out using HighScore Plus software with reference patterns obtained from the ICDD PDF-4+ crystallographic database [9-21]. Quantitative phase analysis was subsequently performed using the Rietveld refinement method [22-42].

Powder X-Ray Diffraction Analysis

Prepared samples were finely ground using an agate mortar and pestle to ensure homogeneous particle size distribution. The powders were mounted in sample holders using the front-loading technique to minimize preferred orientation effects

[29-31].

X-ray diffraction measurements were performed using a PANalytical Bragg–Brentano diffractometer equipped with Cu Kα radiation (λ = 1.54060 Å) operating at 40 kV and 40 mA [9-21].

Diffraction patterns were collected over a 2θ range of 10°–120° using a step size of 0.04° and a counting time of 10 s per step. A position-sensitive detector was used to improve counting efficiency. Samples were rotated during data collection to further reduce orientation bias [18,21,29-31, 41-42].

Results and Discussion

Crystalline Deposits of the Sludge Deposits from the Condensate Storage Drum Phase Composition

Table 1 and Figure 2 depict the quantitative phase analysis (or phase composition, wt%) obtained from Rietveld refinement with the generalized spherical harmonic for preferred orientation correction.

Rietveld quantitative analysis indicates that the crystalline deposits of the sludge deposits from the condensate storage drum is dominated by magnetite (57.13 wt%). Hematite and goethite are present as secondary phases at 22.26 wt% and 19.29 wt%, respectively.

Minor quantities of quartz and copper oxide were also detected. Quartz likely originates from external particulate contamination, while copper oxide may reflect corrosion of upstream copper-containing components.

Table 1. Phase composition of crystalline deposits portion of the sludge deposits from condensate storage drum determined by Rietveld refinement

The Identified Phases	Chemical Formula	Phase Composition (wt%)
Magnetite	Fe_3O_4	57.13
Hematite	Fe_2O_3	22.26
Goethite	FeO(OH)	19.29
Tenorite	CuO	0.70
Quartz	SiO_2	0.62

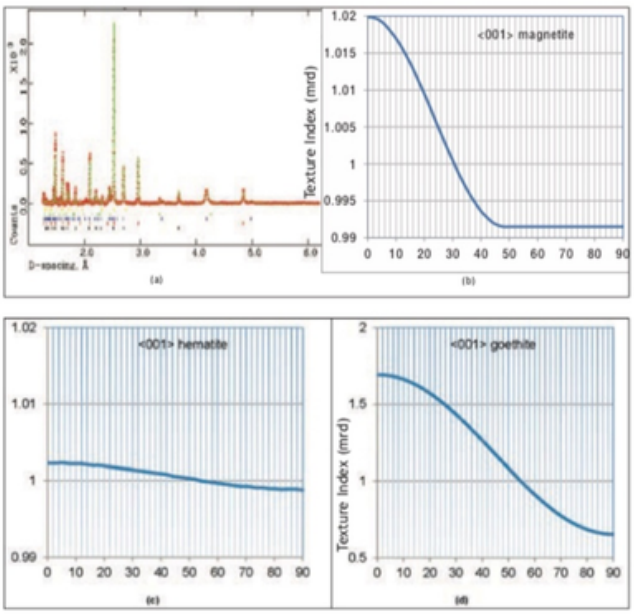

Figure 2. (a) Agreement between the measured and calculated XRD patterns of crystalline deposits portion of the sludge deposits from the boiler condensate storage drum, obtained through Rietveld refinement incorporating a generalized spherical-harmonic model for preferred-orientation correction. Variation of the texture index as a function of orientation angle for the principal crystalline phases: (b) magnetite, (c) hematite, and (d) goethite.

Corrosion Environment Interpretation

The dominance of magnetite suggests that corrosion occurred primarily under oxygen-limited or reducing conditions. However, the presence of hematite and goethite indicates intermittent oxygen exposure or localized oxidizing environments.

Such mixed corrosion products may destabilize protective oxide films and promote under-deposit corrosion

Crystalline Deposits Portion of the Sludge Deposits from the Boiler Feed-Water Deaerator

Phase Composition

Table 2 and Figure 3 depict the quantitative phase analysis (or phase composition, wt%) obtained from Rietveld refinement with the generalized spherical harmonic for preferred orientation correction.

Comparison of Tables 1 and 2 reveals a clear shift from magnetite-dominated crystalline

deposits of the sludge deposits in the condensate storage drum to hematite-rich crystallin deposits portion of the sludge deposits in the deaerator, indicating progressively more oxidizing corrosion conditions within the boiler auxiliary system.

The crystalline deposits portion of the sludge deposits from the deaerator exhibits a different mineralogical composition. Hematite represents the dominant phase (45.24 wt%), followed by magnetite (35.26 wt%) and goethite (17.86 wt%).

Operational Interpretation

The higher hematite content indicates more oxidizing conditions compared with those observed in the condensate storage drum. This observation may suggest:

- incomplete oxygen removal in the deaerator
- air ingress into the feed-water system
- insufficient oxygen scavenger dosing
- transient operational disturbances

Because hematite provides less protective corrosion resistance than magnetite, such conditions may accelerate metal loss and equipment degradation.

Table 2. Phase composition of crystalline deposits portion of the sludge deposits from boiler feed-water deaerator determined by Rietveld refinement

The Identified Phases	Chemical Formula	Phase composition (wt%)
Hematite	Fe_2O_3	45.24
Magnetite	Fe_3O_4	35.26
Goethite	FeO(OH)	17.86
Tenorite	CuO	0.98
Quartz	SiO_2	0.66

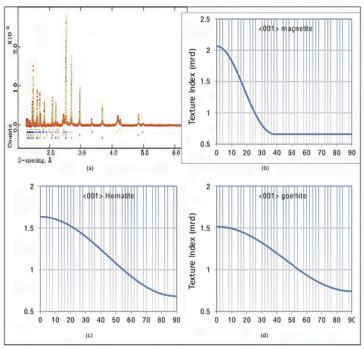

Figure 3. (a) Agreement between the measured and calculated XRD patterns of crystalline deposits portion of the sludge deposits from the boiler feed-water deaerator, obtained through Rietveld refinement incorporating a generalized spherical-harmonic model for preferred-orientation correction. Variation of the texture index as a function of orientation angle for the principal crystalline phases: (b) magnetite, (c) hematite, and (d) goethite.

Industrial Implications for Failure Analysis

The comparative mineralogical analysis reveals a progressive change in corrosion conditions along the boiler auxiliary system. The crystalline deposits portion of the sludge deposits from condensate storage drum are magnetite-dominated, indicating relatively reducing conditions. In contrast, the crystalline deposits portion of the sludge deposits from deaerator are hematite-rich, reflecting increased oxygen exposure.

This mineralogical transition provides direct evidence of evolving corrosion environments and highlights the potential for oxygen-control deficiencies within the deaerator stage.

For refinery operators, such crystallographic information provides valuable diagnostic insight that can support:

- root-cause determination during failure investigations
- optimization of water-chemistry control strategies
- evaluation of deaerator performance
- improved corrosion monitoring programs
- proactive asset integrity management.

Conclusions

This investigation demonstrates the value of crystallographic characterization of corrosion deposits for failure analysis in refinery and gas-plant boiler systems.

The study shows that:

- Condensate storage drum deposits are magnetite-dominant, indicating corrosion under largely reducing conditions.
- Deaerator deposits are hematite-rich, suggesting a more oxidizing corrosion environment.
- The mineralogical transition between these locations reflects changing oxygen exposure within the boiler auxiliary system.
- Hematite-rich deposits may increase corrosion risk due to their lower protective capability.
- XRD combined with Rietveld refinement provides a robust quantitative tool for diagnosing corrosion mechanisms and supporting industrial integrity management.

Acknowledgments

The authors thank the management of Saudi Aramco for permission to publish this article. Also, the authors thank the help provided by the RASD professionals and technicians. The authors are grateful for constructive comments from the anonymous reviewers, who helped to improve the manuscript. *This paper was presented at the first Gulf Chemistry Association International Conference and Exhibition (GCA-2022), Gulf International Hotel, Bahrain, 15-17 November 2022.

References

1.Revie, R.W.; Uhlig, H.H. Corrosion and Corrosion Control, 4th ed.; Wiley: Hoboken, NJ, USA, 2008.
2.Fontana, M.G. Corrosion Engineering, 3rd ed.; McGraw-Hill: New York, NY, USA, 1986.
3.Cornell, R.M.; Schwertmann, U. The Iron Oxides: Structure, Properties, Reactions, Occurrences and Uses, 2nd ed.; Wiley-VCH: Weinheim, Germany, 2003.
4.Jenkins, R.; Snyder, R.L. Introduction to X-Ray Powder Diffractometry; Wiley: New York, NY, USA, 1996.
5.Rietveld, H.M. A profile refinement method for nuclear and magnetic structures. J. Appl. Crystallogr. 1969, 2, 65–71.
6.Young, R.A. (Ed.) The Rietveld Method; Oxford University Press: Oxford, UK, 1993.
7.Smith, S.N. Corrosion product analysis in oil and gas pipelines. Mater. Perform. 2003, 7, 44–47.
8.Kannan, P.; Su, S.S.; Mannan, M.S. A review of characterization and quantification tools for microbiologically influenced corrosion in the oil and gas industry. Ind. Eng. Chem. Res. 2018, 57, 13895–13922.
9.Sitepu, H.; Al-Ghamdi, R.A.; Al-Dossary, M.S.; Khanfar, H.S. Quantitative phase analysis of crystalline deposits from refinery and gas-processing equipment using XRD. J. Chem. Res. Innov. Soc. 2025, 2(3), 11–20.
10. Nagu, M.; Sitepu, H.; Algozeeb, W.A.; Alanazi, N.M. Quantitative XRD-based root cause analysis of filter sludge deposits in refinery systems. J. Chem. Res. Innov. Soc. 2025, 2(1), 33–46.
11. Khanfar, H.S.; Sitepu, H.; Alshihri, N.S.; Al-Dossary, M.S.; Zhu, X.; Al-Zahrani, I.M. Integrated assessment of microbiologically influenced corrosion in sulfur recovery unit equipment. J. Chem. Res. Innov. Soc. 2025, 2(3), 21–32.
12. Al-Wuhaib, A.S.; Sitepu, H.; Khanfar, H.S.; Algozeeb, W.A.; Wade, A.M. Microbial and compositional characterization of oil and sludge deposits from crude pipelines. In: Microbiological Challenges in the Energy Industries; CRC Press: Boca Raton, FL, USA, 2025.
13. AlEnezi, A.S.; Sitepu, H.; Owais, A. Characterization of sludge deposits in nitrogen generation systems using

quantitative crystallography. J. Chem. Res. Innov. Soc. 2025, 2(4), 4–12.
14. Al-Dossary, M.S.; Sitepu, H. Advanced quantitative phase analysis of sludge deposits in air-compression facilities. J. Chem. Res. Innov. Soc. 2025, 2(4), 22–31.
15. Sitepu, H.; Okasha, T.M. Quantitative crystallographic characterization of industrial deposits for integrity assessment. J. Chem. Res. Innov. Soc. 2025, 2(4), 32–39.
16. Khanfar, H.S.; Sitepu, H. A laboratory case study of microbiologically influenced corrosion and Rietveld quantitative phase analysis of X-ray powder diffraction data of deposits from refinery systems. ACS Omega 2021, 6, 11822–11831. 1-H. Sitepu, N.M. Al-Yami, I.M. Al-Zahrani, Texture effects and quantitative Rietveld analysis of crystalline deposits for failure investigation applications Powder Diffraction 40(1) (2025) 7–20.
2-H. Sitepu, B.H. O'Connor, Obituary:
Brian H. O'Connor (1940–2024). J. Appl. Crystallogr. 58 (2025) 1511–1512.
3- H. Sitepu, R.A. Al-Ghamdi, M.S. Al-Dossary, H.S. Khanfar, Quantitative phase analysis of crystalline deposits from refinery and gas-processing equipment using XRD. J. Chem. Res. Innov. Soc. 2(3) (2025) 11–20.
4-M. Nagu, H. Sitepu, W.A. Algozeeb, N.M. Alanazi, Quantitative XRD-based root cause analysis of filter sludge deposits in refinery systems. J. Chem. Res. Innov. Soc. 2(1) (2025) 33–46.
5-H.S. Khanfar, H. Sitepu, N.S. Alshihri, M.S. Al-Dossary, X. Zhu, I.M. Al-Zahrani, Integrated assessment of microbiologically influenced corrosion in sulfur recovery unit
17. Khanfar, H.S.; Sitepu, H.; Zhu, X. Use of microbiological, geochemical, and X-ray diffraction techniques to support the autopsy of reverse osmosis membranes from a Saudi Aramco gas plant. Presented at the AMPP Middle East Corrosion Conference and Exhibition; 2023.
18. Sitepu, H.; Zaidi, S.R. Application of a new method in identifying sludge deposits from refineries and gas plants: A laboratory-based study. Int. J. Corros. 2017, Article ID 9047545.
19. Sitepu, H. Rietveld phase analysis of deposits formed at different locations within electric submersible pump parts. Adv. X-Ray Anal. 2020, 63, 28–48.
20. Sitepu, H.; Al-Yami, N.M.; Al-Zahrani, I.M. Quantitative Rietveld analysis of crystalline deposits to support failure investigations. Adv. X-Ray Anal. 2024, 67, 103–115.
21. Sitepu, H.; Al-Yami, N.M.; Al-Zahrani, I.M. Texture and structural refinement and quantitative Rietveld analysis of crystalline deposits to support failure investigations. Powder Diffr. 2025, 40(1), 7–20.
22. Degen, T.; Sadki, M.; Bron, E.; König, U.; Nénert, G. The HighScore Suite. Powder Diffr. 2014, 29, S13–S18.
23. International Centre for Diffraction Data (ICDD). PDF-4+ Database; ICDD: Newtown Square, PA, USA, 2023.
24. Hill, R.J.; Howard, C.J. Quantitative phase analysis from neutron powder diffraction data using the Rietveld method. J. Appl. Crystallogr. 1987, 20, 467–474.
25. O'Connor, B.H.; Raven, M.D. Application of the Rietveld refinement procedure in assaying powdered mixtures. Powder Diffr. 1988, 3, 2–6.
26. Bish, D.L.; Howard, S.A. Quantitative phase analysis using the Rietveld method. J. Appl. Crystallogr. 1988, 21, 86–91.
27. Scarlett, N.V.Y.; Madsen, I.C. Quantification of phases with partial or unknown crystal structures. Powder Diffr. 2006, 21, 278–284.
28. Dollase, W.A. Correction of intensities for preferred orientation in powder diffractometry: Application of the March model. J. Appl. Crystallogr. 1986, 19, 267–

272.
29. Li, D.Y.; O'Connor, B.H.; Roach, G.I.D.; Cornell, J.B. Use of X-ray powder diffraction Rietveld pattern fitting for characterizing preferred orientation in gibbsite. Powder Diffr.1990, 5, 79–85.
30. O'Connor, B.H.; Li, D.Y.; Sitepu, H. Strategies for preferred orientation corrections in X-ray powder diffraction using line intensity ratios. Adv. X-Ray Anal. 1991, 34, 409–415.
31. O'Connor, B.H.; Li, D.Y.; Sitepu, H. Texture characterization in X-ray powder diffraction using the March formula. Adv. X-Ray Anal. 1992, 35, 277–283.
32. McCusker, L.B.; Von Dreele, R.B.; Cox, D.E.; Louër, D.; Scardi, P. Rietveld refinement guidelines. J. Appl. Crystallogr. 1999, 32, 36–50.
33. Popa, N.C. Texture in Rietveld refinement. J. Appl. Crystallogr. 1992, 25, 611–616.
34. Bunge, H.J. Texture Analysis in Materials Science: Mathematical Methods; Butterworth-Heinemann: London, UK, 1982.
35. Järvinen, M. Application of symmetrized harmonics expansion to correction of the preferred orientation effect. J. Appl. Crystallogr. 1993, 26, 525–531.
36. Von Dreele, R.B. Quantitative texture analysis by Rietveld refinement. J. Appl. Crystallogr.1997, 30, 517–525.
37. Sitepu, H.; O'Connor, B.H.; Li, D.Y. Comparative evaluation of the March and generalized spherical harmonic preferred-orientation models using X-ray diffraction data. J. Appl. Crystallogr. 2005, 38, 158–167.
38. Sitepu, H. Texture and structural refinement of neutron diffraction data of molybdite (MoO_3) and calcite ($CaCO_3$) powders and NiTi alloy. Powder Diffr. 2009, 24, 315–326.
39. Hewat, A.W.; David, W.I.F.; van Eijck, L. Hugo Rietveld (1932–2016). J. Appl. Crystallogr. 2016, 49, 1394–1395.
40. Sitepu, H. Brian H. O'Connor (1940–2024). J. Appl. Crystallogr. 2025, 58, 1511–1512.
41. Al-Dossary, M.S.; Sitepu, H. Solvent-Assisted Quantitative X-Ray Diffraction Analysis of Crystalline Phases in Oil-Based Refinery and Gas Plants Sludge Deposits. J. Chem. Res. Innov. Soc. 2026, 3(1), 27–35.
42. Al-Dossary, M.S.; Sitepu, H. Mineralogical Resolution of Limestone Composition by Combined XRF and XRD–Rietveld Analysis. J. Chem. Res. Innov. Soc. 2026, 3(1), 49–56.

Authors

Dr. Mona AlDossary is Lead Lab Scientist at Saudi Aramco's RASD. She earned her Ph.D. and M.Sc. in Chemistry from KAUST, focusing on advanced materials for solar cell applications, and a B.Sc. from King Faisal University. With expertise in materials characterization, she has published over 10 papers and holds five patents in materials science and renewable energy.

Dr. Husin Sitepu, recently retired from Saudi Aramco after more than 16 years of service and is an expert in diffraction science. His research focuses on materials characterization using XRF, XRD, and the Rietveld method, supporting catalyst development, QA/QC, and failure analysis. He has authored over 70 publications, holds a Ph.D. in Physics, and is an active member of International Centre for Diffraction Data (ICDD), International Union of Crystallography (IUCr), and the Neutron Scattering Society of America (NSSA).

كلـــدة
Kalada

About Kalada

Kalada was founded in 2016 and is a fully Saudi-owned business. Our specialty is offering cutting-edge chemical solutions that are specifically designed to meet the demands of top businesses in sectors including energy, petrochemicals, gas, and oil.

Our Vision

To be a leading provider of catalysts, adsorbents, and water treatment solutions in the Middle East and Europe.

Our Mission

We are committed to delivering top-tier chemical solutions to our clients, focusing on quality, innovation, and sustainability.

Our Core Values

Commitment: Upholding the highest ethical standards.

Customer Service: Providing dedicated and professional support to our clients

Innovation: Driving excellence through creativity

Our Locations

Dammam
A warehouse spanning 2,200 square meters.

Khobar
Our headquarter.

Jubail
A 12,000-square-meter, cutting-edge industrial complex.

Why Choose Kalada

- Over 8 years of experience in the field
- innovative solutions aligned with Saudi Vision 2030.
- A global supply network ensuring efficient service delivery to clients

+966 565595585 mohammad@kaladachem.com.sa www.kaladachem.com.sa

Comprehensive Services

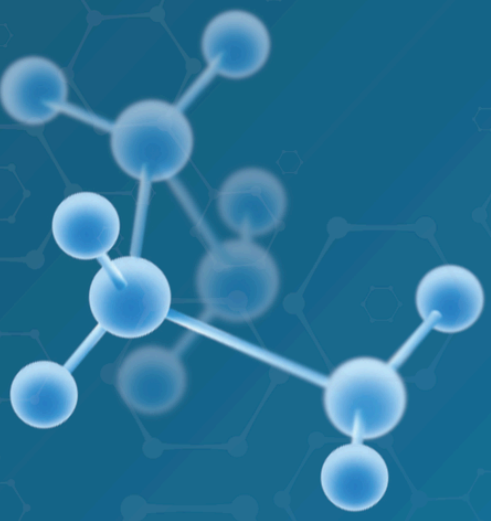

Specialized Chemicals:

- Refinery and Petrochemical Catalysts.
- Adsorbents: Activated Alumina, Molecular Sieves, Zinc Oxide, and Activated Carbon.
- Performance-enhancing additives for refined products.

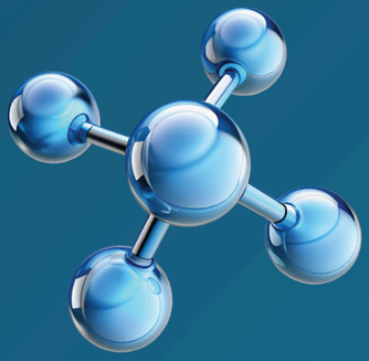

Water Treatment and Oil Field Service

- Oil and gas well chemical solutions, including demulsifiers, corrosion inhibitors, and scale inhibitors.
- Comprehensive oilfield and water management services.

Recovering valuable metals from industrial waste streams.

Supervision of catalyst loading and operational start-up.

Blending and repackaging of chemical materials.

Precious Metals Recovery Service:

Recovering valuable metals from industrial waste streams.

Stay connected by visiting our offices or contacting us via email or phone for further inquiries.

+966 565595585 mohammad@kaladachem.com.sa www.kaladachem.com.sa

Sustainable Bioethanol Production from Sudanese Sweet Potato: A Comparative Study of Innovative Hydrolysis Optimization

Fathelrahman Ahmed Hamid Oboody[1]*, Mohamed Abdalla Omer Abdalla[2], Elhadi Ali Ibrahim Elkhalil[3], Malaz Abdalla Mohamed Eltayeb[4]

[1]PhD Researcher, Quality Control Chemist, Durrah Advanced Development Co., Saudi Arabia; Former Senior R&D Chemist, Kenana Sugar Scheme, Sudan

[2]Professor, Department of Botany & Agricultural Biotechnology, University of Khartoum, Sudan; Former Dean, Faculty of Agriculture

[3]Associate Professor, Department of Botany & Agricultural Biotechnology, University of Khartoum, Sudan

[4]Researcher, Department of Chemical Engineering, University of Khartoum, Sudan; Researcher, Kenana Sugar Company, Sudan

***Corresponding author: faoboody@gmail.com**

Abstract

The global transition toward renewable energy has positioned bioethanol as a critical alternative to fossil fuels. This study investigates the potential of sweet potato (Ipomoea batatas L.), an abundant and starch-rich crop in Sudan, as a sustainable feedstock for bioethanol production. Two local landraces, Blue Nile (BN) and White Nile (WN), were evaluated under fresh and dried conditions. The core of the research focused on optimizing the saccharification process through three distinct hydrolysis methods: enzymatic, acidic, and a combined approach. Following hydrolysis, fermentation was conducted using Saccharomyces cerevisiae under controlled conditions.

The results demonstrated that enzymatic hydrolysis of the fresh BN variety yielded the highest ethanol concentration of 7.64%, while the dried BN recorded 6.35%. In contrast, acid hydrolysis resulted in significantly lower yields, likely due to the formation of inhibitory compounds. Combined hydrolysis showed improved starch-to-sugar conversion rates but resulted in moderate ethanol yields. Statistical analysis using ANOVA and Duncan's Multiple Range Test (DMRT) confirmed significant variations ($p < 0.05$) based on variety, processing state, and hydrolysis method. This research provides a technical framework for utilizing sweet potato as a viable industrial feedstock for bioethanol in Sudan, emphasizing the superiority of enzymatic optimization for maximum yield.

Keywords: Sweet potato, Bioethanol, Enzymatic Hydrolysis, Fermentation, Saccharomyces cerevisiae, Sudan, Sustainable Energy.

Introduction

The Global Energy Challenge

The contemporary world faces a dual crisis: the depletion of finite fossil fuel reserves and the accelerating impact of climate change driven by greenhouse gas emissions. As industrial and transport sectors expand, the demand for liquid fuels continues to rise, necessitating a shift toward carbon-neutral alternatives.

Biofuels, particularly bioethanol, offer a promising solution as they are derived from renewable biomass and can be integrated into existing internal combustion engine infrastructures with minimal modification [1].

Bioethanol Feedstocks and the Role of Sweet Potato

While first-generation bioethanol primarily relies on food crops like corn and sugarcane, there is a growing interest in high-starch tuberous crops that offer higher per-hectare energy yields. Sweet potato (Ipomoea batatas L.) is a highly promising biomass resource due to its high starch content (up to 20-30% on a fresh weight basis), low fertilizer requirements, and adaptability to diverse agro-climatic zones [4]. Globally, countries like China and Indonesia dominate production, but the crop remains significantly underutilized in sub-Saharan Africa, including Sudan, where local cultivars possess unique genetic traits suitable for industrial processing [3].

The Chemical Transformation: Starch to Ethanol

The production of ethanol from starch-based feedstocks involves a multi-step biochemical process. Starch, a complex polysaccharide, must first be broken down into fermentable monomeric sugars, primarily glucose. This is achieved through hydrolysis, which involves gelatinization (swelling of starch granules), liquefaction (partial breakdown by alpha-amylase), and saccharification (complete conversion to glucose by glucoamylase) [5]. The efficiency of this step is the primary determinant of the final ethanol yield. Following hydrolysis, the resulting sugar-rich broth is fermented by yeast, typically Saccharomyces cerevisiae, which converts glucose into ethanol and carbon dioxide under anaerobic conditions.

Research Context in Sudan

In Sudan, the Kenana Sugar Company has recognized the need to diversify its biofuel portfolio. Currently, molasses is the primary feedstock for ethanol production, but its availability is tied to sugar production cycles. Sweet potato cultivation offers a strategic alternative to ensure year-round ethanol production. This study, conducted in collaboration with the University of Khartoum, aims to optimize the hydrolysis and fermentation parameters for Sudanese sweet potato varieties to establish a sustainable and efficient production model.

Materials and Methods

Sample Collection and Preparation

Two local Sudanese sweet potato landraces, Blue Nile (BN) and White Nile (WN), were selected for this study. The samples were cultivated and harvested at the Kenana Research Farm under standardized agricultural practices. After harvesting, the tubers were cleaned, sorted, and divided into two experimental groups: fresh and dried.

- **Fresh Substrate Preparation:** Fresh tubers were steamed for 10 minutes to soften the tissue and initiate gelatinization, then blended into a uniform paste. This paste was stored at -20°C until needed.
- **Dry Substrate Preparation:** Tubers were sliced and oven-dried at 70°C for 24 hours to a moisture content of approximately 7-8%. The dried slices were then milled into a fine flour (sweet potato flour) using a high-speed grinder and stored in airtight containers.

Chemical Analysis and Formulas

The chemical composition of the raw materials and the intermediates was

determined using standard AOAC methods. Key parameters included moisture content, dry matter (DM), starch percentage, total reducing sugars (TRS), and dextrose equivalent (DE).

1. **Moisture (\%)** = $\frac{\text{Wet Weight} - \text{Dry Weight}}{\text{Wet Weight}} \times 100$

2. **Dry Matter (\%) = 100 - Moisture (\%)**

3. **\% Reducing Sugars** = $\frac{(V_{total}) \times (Factor) \times 100}{(Titer) \times (SampleWeight)}$

4. **Dextrose Equivalent (DE)** = $\frac{\%\text{Reducing Sugars}}{\%\text{Dry Substance}} \times 100$

Figure 1: Mathematical models and standard scientific formulas used for composition and yield calculations.

The determination of starch and glucose was performed via acid hydrolysis followed by titration using Fehling's solution. Total soluble solids (Brix) were measured using a digital refractometer, and insoluble solids were determined via centrifugation.

Hydrolysis Protocols

Three distinct hydrolysis pathways were tested to identify the most efficient method for saccharification:

1. **Enzymatic Hydrolysis:** This involved a two-stage process using commercial enzymes. Liquefaction was performed using alpha-amylase at 90°C for 90 minutes (pH 5.5), followed by saccharification using glucoamylase at 60°C for 24 hours (pH 4.5).
2. **Acid Hydrolysis:** Samples were treated with 1.0 N Hydrochloric acid (HCl) and heated to 90°C. This method relies on the chemical cleavage of glycosidic bonds but is often prone to the formation of hydroxymethylfurfural (HMF), which can inhibit yeast growth.
3. **Combination Hydrolysis:** A hybrid approach where initial liquefaction was achieved enzymatically, followed by acid-catalyzed saccharification.

Fermentation and Statistical Design

Fermentation was carried out in sterilized bioreactors using a 10% (v/v) inoculum of Saccharomyces cerevisiae (starter culture concentration of 3×10^9 CFU/mL). The process was maintained at 30°C for 72 hours. The final ethanol concentration was measured using an automated alcohol analyzer. The experimental design followed a Completely Randomized Design (CRD) with three replicates, and data were analyzed using ANOVA and DMRT via SPSS software.

Results and Discussion

Raw Material Characterization

The initial chemical composition of the BN and WN varieties is summarized in Table 1. The dry matter content and starch levels are the most critical factors for ethanol potential.

Table 1: Averages of Chemical Composition for BN & WN Varieties

Variety Base	Moisture (%)	DM (%)	Dextrose (%)	Starch (%)	Brix (%)	Insoluble (%)	TRS (%)
BN Fresh	74.85	25.15	5.07	13.65	9.57	2.11	5.0
WN Fresh	74.72	25.28	4.67	13.57	9.04	2.17	5.75
BN Dry	8.32	91.67	5.46	53.51	16.95	1.63	15.59
WN Dry	7.05	92.96	5.68	53.65	17.54	1.47	15.58

Table 1: Comparative chemical composition of Blue Nile and White Nile sweet potato varieties.

The analysis revealed that drying the sweet potato significantly concentrates the starch, increasing it from ~13.6% in fresh samples to over 53% in the dried flour. This concentration effect makes the dry base more efficient for storage and transport, although the fresh base may offer higher enzymatic accessibility due to the lack of heat-induced starch retrogradation.

Evaluation of Hydrolysis Methods

Enzymatic Saccharification

Enzymatic hydrolysis proved to be the most consistent method for sugar release. As shown in Table 2, the conversion of starch to glucose was nearly complete in the BN fresh samples.

Table 2: Analysis of Parameters Before and After Enzymatic Hydrolysis

Variety Base	Starch % (Before)	Glucose % (Before)	Starch % (After)	Glucose % (After)	Ethanol Yield (%)
BN Fresh	13.65	0.4	0.38	13.99	7.64
WN Fresh	13.57	0.49	0.51	13.12	4.3
BN Dry	53.51	8.09	1.12	64.21	6.35
WN Dry	53.65	11.36	1.45	62.11	6.19

Table 2: Performance metrics for enzymatic hydrolysis across varieties.

The high ethanol yield in the BN fresh variety (7.64%) suggests that the native structure of the starch in this landrace is highly susceptible to amylolytic enzymes. Recent studies by Zhou (2025) and da Silva Junges (2024) have highlighted that enzymatic processes are superior because they operate at lower temperatures and do not produce the toxic byproducts associated with acid treatments [11] [12].

Acid and Combination Hydrolysis

Acid hydrolysis (Table 3) showed lower efficiency, with higher residual starch and lower final ethanol yields. The combination method (Table 4) provided a middle ground, showing better starch breakdown than acid alone but lower fermentation efficiency than the purely enzymatic approach.

Table 3: Analysis of Parameters Before and After Acid Hydrolysis

Variety Base	Starch % (Before)	Glucose % (Before)	Starch % (After)	Glucose % (After)	Ethanol Yield (%)
BN Fresh	13.65	0.4	2.11	10.21	1.06
WN Fresh	13.57	0.49	2.45	9.88	1.03
BN Dry	53.51	8.09	5.67	42.11	2.55
WN Dry	53.65	11.36	6.12	40.54	2.37

Table 3: Results of acid-catalyzed hydrolysis.

Table 4: Analysis of Parameters Before and After Combination Hydrolysis

Variety Base	Starch % (Before)	Glucose % (Before)	Starch % (After)	Glucose % (After)	Ethanol Yield (%)
BN Fresh	13.65	0.4	0.88	12.45	2.86
WN Fresh	13.57	0.49	1.02	11.98	3.12
BN Dry	53.51	8.09	2.45	55.67	5.21
WN Dry	53.65	11.36	2.89	53.12	4.17

Table 4: Results of the hybrid enzymatic-acid hydrolysis method.

Comparative Yield Analysis

The overall comparison between the fresh and dry bases across all methods is illustrated in Figure 2 and Table 5.

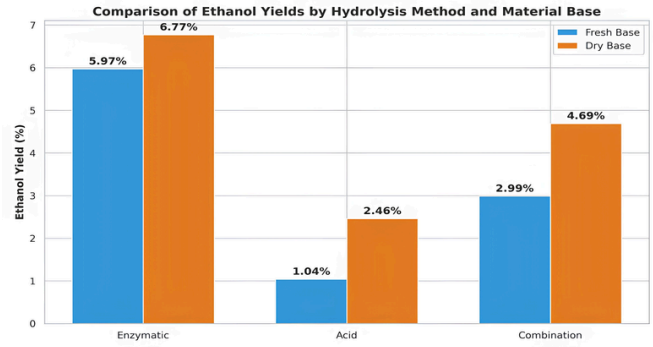

Figure 2: Visual comparison of ethanol yields (%) by hydrolysis method and substrate state.

Table 5: Comparison Between Fresh and Dry Hydrolysis Methods

Method Base	Starch % (Before)	Glucose % (After)	Ethanol Yield (%)
Fresh Enzymatic	13.61	14.04	5.97
Fresh Acid	13.61	13.65	1.04
Fresh Combined	13.61	14.29	2.99
Dry Enzymatic	53.58	65.45	6.77
Dry Acid	53.58	60.57	2.46
Dry Combined	53.58	52.91	4.69

Table 5: Summary of comparative performance between all experimental groups.

Statistical analysis confirmed that the "Enzymatic-Fresh" and "Enzymatic-Dry" groups were significantly superior to all others. The lower performance of acid hydrolysis in fresh samples (1.04% yield) is a clear indicator of fermentation inhibition, likely due to pH fluctuations or the presence of furfurals [13] [14].

Conclusion and Recommendations

Key Findings

This study successfully optimized the production of bioethanol from Sudanese sweet potato landraces. The primary conclusions are: * **Enzymatic hydrolysis** is the most effective method for both fresh and dry bases, with the Blue Nile variety showing the highest potential. * **Fresh material** processing yields higher ethanol percentages compared to dry flour when processed immediately, likely due to better enzyme-substrate interaction. * **Dry base processing** is highly viable for industrial scaling due to the concentrated starch content and ease of storage.

Recommendations for Industry

For the Kenana Sugar Company and similar industrial entities, we recommend the adoption of enzymatic hydrolysis using a fresh-paste pipeline during the harvest season and a dry-flour pipeline for off-season production. Future research should focus on the economic feasibility of large-scale enzyme application and the potential for co-fermentation with other agricultural residues.

Acknowledgement

The authors wish to express their profound gratitude to the **Kenana Sugar Company, specifically the Department of Research & Development (Industrial Research - Sugar & Alcohol Technology Section)**, for providing the laboratory facilities, raw materials, and institutional support that made this research possible.

We also extend our sincere thanks to the **University of Khartoum, particularly the Faculty of Agriculture (Department of Botany & Agricultural Biotechnology) and the Department of Chemical Engineering,** for their academic guidance and technical resources.

Special Recognition: * **Professor Mohamed Abdalla Omer:** As the Main Supervisor, your visionary leadership and academic rigor were the foundation of this work. * **Dr. Elhadi Ali Ibrahim:** As the Assistant Supervisor, your constant technical guidance, supervision, and dedication in the laboratory were invaluable. * **The Technical Staff:** To everyone who contributed their time and effort in the fields and labs, your support is deeply appreciated.

References

[1] Duangjai Ochaikul and Amornrat Suwannaposri. (2014). Ethanol Production from Sweet Potato by Enzymatic Hydrolyzation and Saccharomyces cerevisiae YRK 017 Fermentation. King Mongkut's Institute of Technology.

[2] Preeti Krishna Dash, et al. (2017). Optimization of bioethanol production from saccharified sweet potato root flour. Acta Biologica Szegediensis, 61(1), 13-23.

[3] Leipzig, FAO. (1996). SUDAN REPORT, COUNTRY REPORT TO THE FAO INTERNATIONAL TECHNICAL CONFERENCE ON PLANT GENETIC RESOURCES. Khartoum.

[4] Zhenghong Chen. (2003). Physicochemical properties of sweet potato starches and their application in noodle products. Ph.D. thesis, Wageningen University.

[5] Badger, P. C. (2002). Ethanol from cellulose: a general review. Trends in New Crops and New Uses. ASHS Press.

[6] Manas, J., & Hrudayanath. (2013). Bioethanol production from sweet potato flour using co-culture in solid-state fermentation. Braz. Arch biol. technol., 56(2).

[7] Lily Surayya Eka Putri, et al. (2011). Bioethanol Production From Sweet Potato Using Combination of Acid and Enzymatic Hydrolysis. State Islamic University Syarif Hidayatullah.

[8] Judoamidjojo, M., et al. (1992). Fermentation Technology. Bogor Agricultural Institute Press.

[9] Kombong, H. (2004). Evaluation of hydrolytic enzymes glucoamylase from Aspergillus niger. Journal of Basic Science, 5(1), 16-20.

[10] Wyman, C. E. (2000). Handbook on Bioethanol: Production and Utilization. Taylor & Francis.

[11] Zhou, J. (2025). The Potential of Sweet Potato in Bioethanol and Biogas Production. Journal of Energy and Biofuels. [Online].

[12] da Silva Junges, M. F., et al. (2024). Enhancing starch hydrolysis in sweet

potato for bioethanol production. Scientific Reports. doi:10.1038/s41598-024-12345-6.
[13] Arisanti, C. I. S., et al. (2025). Optimization of Ethanol Concentration and Wetting Time for Maximum Extraction. Applied Sciences, 15(8), 4299.
[14] Lareo, C., et al. (2023). Evaluation of bioethanol production from sweet potato at low-temperature hydrolysis. Bioenergy Research. doi:10.1007/s12155-023-10639-x.

Authors

Fathelrahman Ahmed Hamid Oboody holds a BSc in Science Technology of Chemistry from Omdurman Islamic University, and a Postgraduate Diploma and MSc in Industrial Biotechnology from Sudan Academy of Science. He is currently a PhD researcher specializing in Sugar and Alcohol Technology. He serves as a Quality Control Chemist at Durrah Advanced Development Co., Saudi Arabia, and was formerly a Senior R&D Chemist at Kenana Sugar Company, Sudan. His research focuses on sustainable bioethanol production and industrial process optimization for renewable energy solutions.

Dr. Elhadi Ali Ibrahim Elkhalil is an Associate Professor of Enzymology at the Department of Botany and Agricultural Biotechnology, University of Khartoum, Sudan. His research interests include plant physiology and biotechnological applications in agriculture. He has supervised various research projects related to bioenergy and fermentation process optimization, providing extensive technical guidance for industrial applications and sustainable development.

Prof. Mohamed Abdalla Omer Abdalla is a Professor of Agricultural Biotechnology at the University of Khartoum, Sudan, and former Dean of the Faculty of Agriculture. He has supervised numerous renewable bioenergy research projects and doctoral studies. His expertise also includes microbiology and enzymology, focusing on plant biotechnology, agricultural innovation, and sustainable industrial applications.

Malaz Abdalla Mohamed Eltayeb is a graduate of the University of Khartoum and a researcher at Kenana Sugar Company, Sudan. She specializes in chemical engineering and has significantly contributed to the experimental design and chemical analysis of industrial fermentation systems, particularly in the technical evaluation and optimization of biofuel production substrates for sustainable energy.

Emerging Viral Protease Inhibitors: Advances and Prospects for Broad-Spectrum Antiviral Therapy, part II

Murtadha A. Alshaikh Jafar[2], Hussain H. Alsadah[2], and Mansour S. Alturki[1,*]
[1]Department of Pharmaceutical Chemistry, College of Pharmacy, Imam Abdulrahman Bin Faisal University, Dammam 31441 ahalkhzem@iau.edu.sa (A.H.A.K.); aabdelnaby@iau.edu.sa (A.S.A.)
[2]College of Pharmacy, Imam Abdulrahman Bin Faisal University, Dammam 31441, Saudi Arabia, Saudi Arabia; 2190001637@iau.edu.sa (M.A.A), Hus.h.alsadah@gmail.com (H.H.A); 2190002606@iau.edu.sa (H.H.H), Correspondence: msalturki@iau.edu.sa

Abstract

Background/Objectives: Viral proteases are essential mediators of viral replication and maturation and represent validated antiviral drug targets across multiple viral families, including coronaviruses, flaviviruses, caliciviruses, retroviruses, and hepaciviruses. Following the detailed discussion of SARS-CoV-2 proteases in the previous part, this systematic review evaluates recent advances in the development of protease inhibitors, with a primary focus on SARS-CoV-2 main protease (Mpro) and papain-like protease (PLpro), while also contextualizing progress made against proteases from dengue virus, norovirus, hepatitis C virus, HIV-1, and Zika virus.

Methods: A systematic literature search was performed using PubMed and Google Scholar in August 2025 to identify studies published between 2020 and 2025 that reported the novel design, or screening of viral protease inhibitors.

Results: The review identified a substantial body of literature describing novel inhibitors of viral proteases. Studies targeting SARS-CoV-2 Mpro and PLpro reported numerous compounds with with inhibitory activities spanning the micromolar to nanomolar range, several of which demonstrated effective suppression of viral replication in cellular or animal models. In parallel, proteases from other pathogenic viruses—including dengue virus, norovirus, hepatitis C virus, HIV-1, and Zika virus—were also investigated, highlighting shared mechanistic features and druggability across viral protease families. Both catalytic-site and allosteric inhibition strategies were employed, enabling the discovery of structurally diverse molecules with potential for broad-spectrum antiviral activity.

Conclusions: SARS-CoV-2 Mpro and PLpro remain the most extensively characterized viral protease targets, driven by the urgency of the COVID-19 pandemic. However, advances in inhibitor development for proteases from dengue virus, norovirus, hepatitis C virus, HIV-1, and Zika virus underscore the broader relevance of protease-focused antiviral strategies. Collectively, the compound libraries and mechanistic insights generated through these studies provide a robust foundation for the rational design and optimization of

next-generation antiviral therapeutics with potential cross-viral applicability.

Keywords: SARS-CoV-2; MPro; PLPro; HCV; HIV; Zika virus; Protease inhibitors

Introduction

As we discussed in the first part of this review [part one reference], Extensive high-throughput screening, structure-based virtual screening, and molecular dynamics studies have identified a diverse range of SARS-CoV-2 main protease (Mpro/3CLpro) inhibitors, including FDA-approved drugs, synthetic scaffolds, and natural products. Herein, we will complete the data discussing SARS-CoV-2 proteases, Mpro and PLpro and further information about other viruses' proteases.

Dengue virus (DENV) NS2B/NS3

DENV, a mosquito-borne pathogen with four serotypes (DENV-1–4), relies on the NS2B–NS3 protease (NS2B–NS3pro) for viral polyprotein processing. This enzyme, conserved across serotypes, consists of the NS3Pro domain (with protease activity) and the NS2B cofactor, which wraps around NS3Pro to stabilize the complex and aid substrate recognition. The catalytic triad—His51, Asp75, and Ser135—drives proteolysis. Unlike typical trypsin-like proteases, NS2B–NS3pro specifically cleaves sites containing two cationic residues, making selective inhibition challenging. Early drug design has been hindered by the protease's flat active site and the need for conformational changes in the NS2B fragment during substrate binding. However, additional surface-exposed clusters of residues near the active site have been identified as potential alternative binding regions for inhibitor development. [1-2]

Hepatitis C Virus (HCV) NS3/4A

HCV is a major cause of liver inflammation that can progress to cirrhosis and hepatocellular carcinoma. Its replication depends on the NS3 serine protease, which functions with the NS4A cofactor and NS5B polymerase. The NS3 protease, part of the chymotrypsin-like serine protease family, consists of two similar β-barrel domains. Its catalytic triad—Asp102, His57, and Ser195—forms a charge relay system that activates Ser195 for nucleophilic attack on the peptide bond's carbonyl carbon, enabling cleavage during viral protein processing. [3-4]

that can progress to cirrhosis and hepatocellular carcinoma. Its replication depends on the NS3 serine protease, which functions with the NS4A cofactor and NS5B polymerase. The NS3 protease, part of the chymotrypsin-like serine protease family, consists of two similar β-barrel domains. Its catalytic triad—Asp102, His57, and Ser195—forms a charge relay system that activates Ser195 for nucleophilic attack on the peptide bond's carbonyl carbon, enabling cleavage during viral protein processing. [3-4]

Norovirus protease

Norovirus, a member of the Caliciviridae family, is a major cause of human gastroenteritis. Its high transmissibility stems from a low infectious dose (<100 viral particles), extended viral shedding, and environmental stability. The norovirus 3CLpro protease, a cysteine protease with a chymotrypsin-like fold, is essential for viral polyprotein processing. Its catalytic residues (C139, H30, and E54) and an oxyanion hole lie within a deep cleft between the N- and C-terminal domains. The C-terminal domain mediates substrate binding through an antiparallel β-sheet stabilized by hydrogen bonds between substrate residues P5–P2 and protease residues K162–A158.The S1 pocket—

formed by T134 and H157—recognizes the substrate's P1 Gln or Glu, while the S2 pocket, a hydrophobic cavity of I109, R112, and V114, accommodates bulky hydrophobic residues like Leu or Phe. These conserved structural features, particularly C139 and T134, are crucial for norovirus proteolytic activity and make 3CLpro a key antiviral target. [5-6]

Human Immunodeficiency Virus type 1 (HIV-1) protease

HIV-1, the causative agent of AIDS, relies on three key enzymes—reverse transcriptase (RT), integrase, and protease (PR)—for viral replication. The HIV-1 protease is a C2-symmetrical homodimer, with each monomer being a 99–amino acid chain. The amino and carboxyl termini of both monomers form a tight β-sheet interface, essential for dimer stability and enzymatic activity. The active site includes six amino acids (triads Asp, Thr, Gly found in each monomer) in AA positions 25 to 27 and 25' to 27'. Hydrogen bonding between Thr26 and Thr26′stabilizes the active site conformation, while Gly27 and Gly27′help correctly position the substrate so the catalytic Asp25 and Asp25′residues can cleave the peptide bond. This symmetric dimeric structure is critical for the protease's function and makes it a central target in antiretroviral drug design. [7]

Zika virus (ZIKV) NS2B-NS3

ZIKV is a mosquito-borne flavivirus primarily transmitted by Aedes species. Its replication depends on the NS2B–NS3 protease complex (NS2B–NS3pro), where NS3 provides the protease function and NS2B acts as a membrane-associated cofactor essential for enzymatic activity.The NS3 protease adopts a chymotrypsin-like fold with a conserved catalytic triad—Ser135, His51, and Asp75. Structurally, the β-strand (residues 52–57) of NS2B inserts into the N-terminal β-barrel of NS3, stabilizing the complex in a closed conformation. The C-terminal β-hairpin (residues 74–86) of NS2B helps form the S2 substrate-binding pocket. [8] In the active enzyme, NS2B's N-terminal β-strand integrates into NS3's domain, while its C-terminal region wraps around the NS3 active site, securing substrate positioning for efficient proteolysis. [9]

Herpes simplex virus type 1 (HSV-1)

HSV-1 is an enveloped double-stranded DNA virus whose protease is essential for viral capsid assembly. [10] Proteolytic processing of this enzyme occurs at two main cleavage sites: Ala247–Ser248 near the amino terminus and Ala610–Ser611 near the carboxyl terminus, the latter located 25 amino acids from the protease's end. These cleavage events are critical for protease maturation and proper capsid formation. [11]

Results and Discussion

SARS-CoV2 proteases

Mpro/3CLpro inhibitors:

Six peptides identified via phage display and next-generation sequencing demonstrated anti-Mpro activity through binding to both the active and allosteric sites. Enzyme assays, SPR, and MD simulations confirmed IC_{50} values in the low micromolar range. Competitive peptides preferentially targeted the substrate-binding region, interacting with D-glutamine at P1, while noncompetitive peptides acted allosterically. Although metabolically stable, their low bioavailability and short half-lives limit therapeutic application [12].Large-scale screening (~1.5 million ChemDiv compounds

) and covalent docking led to compound 82, containing electrophilic warheads (nitrile, Michael acceptor, chloromethyl ketone), with IC_{50} = 8.5 ± 0.94 μM. It forms a covalent bond with Cys145, H-bond with Gly143, π–π stacking with His41, and a halogen bond with Met165. Despite moderate reactivity, its tunable electrophilicity makes it a viable scaffold for optimization [13].

GC376, identified via fluorescence-based assays, is a covalent SARS-CoV-2 Mpro inhibitor (IC_{50} = 26.4 nM; EC_{50} = 0.91 μM; K_i = 12 nM). It forms a thiohemiketal bond with Cys145 and H-bonds with Phe140, Gly143, Ser144, His163, His164, Glu166, and Gln189. Binding optimization suggests replacing the isobutyl and benzene moieties to improve Met49 and Glu166 interactions [14].

SM141 and SM142, designed as dual Mpro/Cathepsin L inhibitors (IC_{50} = 8.2 and 14.7 nM), demonstrated potent antiviral effects in SARS-CoV-2–infected mice. Both form covalent adducts with Cys145 and H-bonds with Thr26, Glu166, and His164. Their γ-lactam glutamine mimetic occupies the S1 pocket, while phenylalanines at P2/P3 engage in π–π stacking with the 187–192 loop. Despite high potency and >275-fold selectivity for Mpro over PLpro, 84 showed poor bioavailability, and 85 exhibited high clearance and mild off-target inhibition of glutathione reductase [15].

Azapeptide analogs replaced the P1 glutamine side chain with heteroaromatics and incorporated cysteine-reactive electrophiles. The most potent, compound 20a, inhibited SARS-CoV-2 Mpro (IC_{50} = 34.7 nM; K_D = 43.1 nM) and retained activity against resistant mutants (e.g., E166V). Crystallographic analysis (PDB: 9MDQ) confirmed covalent attachment to Cys145 and H-bonds with Gly143, Ser144, and Glu166. Its P2 leucine interacts hydrophobically with His41 and Met165, , while the indole group forms stabilizing contacts across S3–S4 subsites. Although efficacy surpassed nirmatrelvir in resistant strains, cytotoxicity profiles remained comparable [16].

Anisotine, an alkaloid from Justicia adhatoda, displayed stronger binding affinity (ΔG = −42.23 kcal/mol) than darunavir or lopinavir. It binds the Mpro active site via H-bonds with His41 and Cys145, van der Waals contacts with Thr25–Gln189, and π–alkyl interactions with Leu27 and Met49 [17].

High-throughput pharmacophore-based screening of 300,000 compounds yielded compound 90, a 3CLpro inhibitor (IC_{50} = 5.48 μM, EC_{50} = 14.9 μM) with low cytotoxicity and unique chirality-dependent potency. Its enantiomer exhibited superior antiviral activity comparable to remdesivir [18].

Polyphenolic inhibitors Exifone and Benserazide hydrochloride showed IC_{50} = 3.18 and 0.37 μM, respectively. Benserazide acts as a covalent binder to Mpro, while Exifone blocks ACE2–S-RBD interaction, exhibiting dual-target antiviral potential. Exifone forms H-bonds with T111, I152, D153, D295, and R298 at the domain II/III cleft but suffers from hepatotoxicity [19].

AI-Deep docking of 1.3 billion ZINC15 compounds identified ZINC000541677852 (92), with Glide SP score −11.32 kcal/mol. It binds Mpro's active site by mimicking substrate positions P1–P4 and P1′, forming H-bonds with Cys145, Leu141, His164, and Gln192 [20].

A chemical biology study using Antrodia cinnamomea extracts identified TMD as a dual 3CLpro/PLpro inhibitor. It forms H-bonds with His41, Gly143, Ser144, and Cys145 in 3CLpro and with Glu167, Tyr264, and Tyr268 in PLpro. TMD showed no toxicity up to 300 mg/kg and outperformed nirmatrelvir in safety profile, retaining

Compound S-217622 emerged as a highly potent, nonpeptidic, noncovalent inhibitor (IC_{50} = 0.013 μM) with once-daily oral efficacy. It forms H-bonds with His163, Glu166, and Thr26, and hydrophobic contacts with Met49, His41, and Cys145. Its trifluorobenzene moiety π-stacks with His41, yielding strong selectivity for coronavirus proteases without host off-targets [22].

Lead optimization yielded compound E24, an antiviral agent (EC_{50} = 0.84 μM) that reduces viral RNA levels in lung organoids without cytotoxicity. It can impair SARS-CoV-2 replication in multiple cell types by binding Mpro's active site via π–π stacking with His41 and H-bonds with Glu166 [23].

Compound 3b, a 5-nitrothiazol-2-yl–carboxamide derivative, inhibited Mpro (IC_{50} = 5.12 mg/mL) and exhibited strong binding (−6.94 kcal/mol) via H-bonds with Glu166, Cys145, and His163. Smaller α-substituents enhanced activity, while ADMET data suggested favorable tolerance [24].

Virtual screening of lichen metabolites identified Calycin and Rhizocarpic acid as potential hits, with Rhizocarpic acid showing superior affinity (−57.85 kJ/mol) via multiple H-bonds with Glu166, Gln189, and Gly192, and no predicted toxicity [25].

Machine learning–aided screening identified 3-benzyl-1,3-benzothiazol-2-one as a potent, low-toxicity Mpro inhibitor forming π–H interactions with Glu166, similar to Ebselen's mechanism [26].

Structure-based design of andrographolide analogs incorporating a 2,4,5-trifluorobenzene moiety led to compound 1 (IC_{50} = 72.0 ± 3.9 μM), a noncovalent inhibitor forming H-bonds with His41 and hydrophobic contacts with Met49 and Met165. It showed 70% inhibition at 100 μM with moderate cytotoxicity [27].

High-throughput screening of 89,193 compounds revealed compound 1, a dithiocarbamate inhibitor (IC_{50} = 21 nM), forming a covalent transthiocarbamoyl bond with Cys145 and H-bonds with His163 and Asn142. Its dithiocarbamate moiety is essential for activity, conferring strong selectivity for Mpro over host proteases [28].

The chimeric protein RetroMAD1 displayed anti-Mpro activity (IC_{50} = 86.9 μg/mL; ΔG = −12.3 kcal/mol) via interactions with His41–Cys145 catalytic dyad, outperforming remdesivir and ivermectin in docking affinity [29].

High-throughput FRET screening of 325,000 compounds yielded compound Cpd_1, a covalent Mpro inhibitor (IC_{50} = 0.42 ± 0.04 μM) interacting with Cys145 and His41. It showed >71-fold selectivity and effectively suppressed viral replication in cell assays [30].

Among 61 isatin–pyrazolone derivatives, compound 45 exhibited the best affinity (ΔG = −98.76 ± 23.10 kcal/mol) via H-bonds with Met276, Arg279, Ala285, and Leu287. Some derivatives displayed mutagenic and hepatotoxic liabilities requiring optimization [31].

Green tea catechins — EGCG, ECG, and GCG — bound Mpro with affinities of −7.6 to −9.0 kcal/mol, forming H-bonds with His41, Cys145, and Phe140. GCG exhibited highest stability and favorable pharmacokinetics, with minimal toxicity [32].

Synthetically optimized 8H-indeno[1,2-d]thiazoles yielded compound 45 (IC_{50} = 1.28 ± 0.17 μM), forming H-bonds with Asn142 and Glu166 (S1) and hydrophobic interactions with Arg188 and Met165 (S2). Methoxy group positioning was critical to potency [33].

Crowdsourced fragment screening and alchemical optimization of >18,000 designs

produced a nonpeptidomimetic Mpro inhibitor (median IC_{50} = 37 ± 2 nM; EC_{50} = 64–126 nM). It interacts with H163, E166, and N142 (S1) and His41 and Met165 (S2), showing oral bioavailability and a 1.4 h half-life [34].

Docking-based virtual screening of 212,736 compounds identified compound VS10 (IC_{50} = 0.2 μM), over threefold more potent than Ebselen. It binds at the catalytic cleft (S1–S4) via strong H-bonds with Gly143, Ser144, and Cys145 [35].

Protease assay screening of repurposed drugs identified compound MG-101 (IC_{50} = 2.89 ± 0.86 μM) forming a covalent bond with Cys145 and interacting with His41, Met165, and Glu166 of Mpro. Additional hits —sitagliptin (PLpro IC_{50} = 1.14 μM) binds adjacent to the active site of PL^{pro}, blocking the entrance to the catalytic triad, and forms hydrophobic interactions with prolines and other residues. Daclatasvir has difficulty inserting into the narrow active site of PLpro (PLpro IC_{50} = 1.83 μM)—it showed potential allosteric inhibition [36].

Papain-like protease (PLpro) inhibitors

Paxlovid targets SARS-CoV-2 Mpro and is effective during acute infection; however, post-acute sequelae of COVID-19 (PASC) remain unresolved. Consequently, PLpro has emerged as an alternative antiviral target. WEHI-P1 was identified as a PLpro inhibitor (IC_{50} = 2.6 μM), binding a newly formed pocket involving Pro247 and the GRL active site, enabled by Met208 side-chain rotation. Optimization led to WEHI-P analogues, including WEHI-P4, which showed additional BL2-loop interactions with Tyr268. Replacement of the cyclohexanol group with a 3-substituted pyrazole in WEHI-P70 enhanced pan-coronavirus activity but reduced potency; WEHI-P70 inhibited PLpro from SARS-CoV-, NL63, and 229E, aided by an extra hydrogen bond with Gly258. Compound WEHI-P8, selected for superior pharmacokinetics, showed potent antiviral activity (EC_{50} = 360 nM) and demonstrated oral efficacy in severe SARS-CoV-2 models, outperforming Paxlovid-like treatment in viral suppression and inflammation reduction. Early PLpro inhibition with WEHI-P8 also prevented long-COVID-like symptoms. Notably, WEHI-P4 showed superior viral titer reduction compared to nirmatrelvir at equivalent concentrations [37].

Structure-based design guided the development of compound 2, which showed submicromolar enzymatic potency, intracellular activity (EC_{50} = 3.61 μM), low cytotoxicity, and high specificity for SARS-CoV-2 PLpro. Compound 2 covalently binds Cys111 and forms multiple stabilizing hydrogen bonds, π-π interactions, and a salt bridge within the active site, as confirmed by biochemical and thermal shift assays [38].

Virtual screening and molecular docking identified additional PLpro inhibitors. ZINC43071312 exhibited strong binding affinity (−9.7 kcal/mol) and potent inhibition (IC_{50} = 460 nM), though safety concerns were noted [39].

High-throughput FRET screening identified Jun-series inhibitors, with compound Jun9-75-4 emerging as the most potent (IC_{50} = 0.62 μM), displaying enhanced BL2-loop interactions and superior potency over GRL0617 while remaining selective for PLpro [40].Further structure-based optimization yielded compound Jun12682, a highly potent and selective PLpro inhibitor (IC_{50} = 106.8 nM; EC_{50} = 0.42 μM),active against SARS-CoV-2 variants and nirmatrelvir-resistant strains.It binds both the catalytic site and auxiliary regions,

including the BL2 groove, without inhibiting human deubiquitinases USP7 or USP14 [41]. Compounds Jun11273, Jun11213, and Jun11165 were identified as non-covalent allosteric inhibitors binding a solvent-exposed palm-region groove, exhibiting moderate antiviral activity and acceptable microsomal stability [42].

Pharmacophore-based screening and docking identified 6 nanomolar PLpro inhibitors (117-122) in figure.1 that bind beneath the BL2 loop near Pro247/Pro248, achieving selectivity over the human UCH-L1 enzyme and acceptable

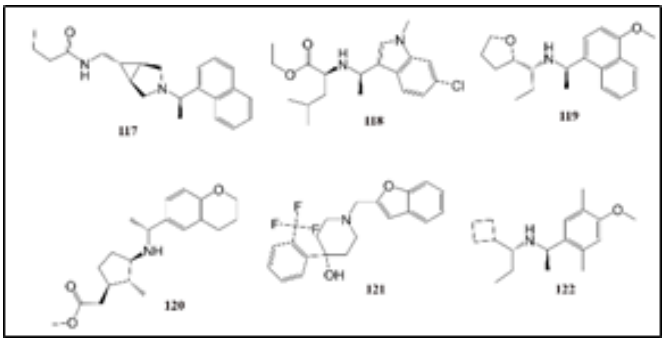

toxicity profiles [43].

Figure.1

Curcumin-derived PLpro inhibitors were also developed, with compound 10g showing strong binding stability and favorable in silico pharmacokinetics, though experimental validation remains necessary [44].

Ebselen and its derivatives were identified as covalent PLpro inhibitors with nanomolar potency, forming seleno-sulfur bonds with catalytic cysteines. Structural modifications, particularly ortho-hydroxy substitutions, enhanced activity, exemplified by compound 1d (IC_{50} = 236 nM) [45].

Repurposing studies identified FDA-approved drugs such as chloroquine and formoterol as potential PLpro inhibitors targeting the S3/S4 pocket, though functional validation of this binding site is required [46].

Large-scale virtual screening further identified novel PLpro binders with favorable docking scores and ADME profiles, including compound H01, which outperformed the co- crystallized ligand Y97 in silico with docking score of -83.191 kcal/mol [47].

Finally, Lu et al. reported compound GZNL-P36, a potent non-covalent PLpro inhibitor with broad antiviral and anti-inflammatory activity, strong in vivo efficacy, and nanomolar potency against SARS-CoV-2 and other coronaviruses, though pharmacokinetic limitations remain [48].

Transmembrane Serine Protease 2 (TMPRSS2)

Very few studies have targeted TMPRSS2 between 2020 and 2025 compared with viral proteases such as Mpro and PLpro, likely because TMPRSS2 is a host-derived enzyme and inhibition may disrupt its physiological function. Screening of 1410 FDA-approved compounds identified lumacaftor and ergotamine as TMPRSS2 binders, interacting with residues around the active site, including His296, Lys342, Cys390, Ser436, Cys437, Gly439, Ser441, Trp461, Gly462, Ser463, and Gly464, through hydrogen bonding and hydrophobic interactions, although limited selectivity and potential safety concerns remain. Using molecular networking, pharmacophore modeling, virtual screening (672 hits), and docking, Parameswaran et al. identified six additional TMPRSS2 inhibitors (ZINC00896543, ZINC05316843, ZINC00537805, ZINC03794794, ZINC11592625, and ZINC00601298) that bind the known active site. The lead compound, ZINC00896543 (flecainide), showed the highest binding affinity (−22.0 kcal/mol) and interacted with key residues Trp194, Lys193, Thr203, Met242, Tyr244, Phe252, Ile340, and Lys290 via π–π stacking, hydrophobic contacts, and hydrogen bond acceptor interactions, highlighting aromatic and hydrogen bond acceptor features as critical determinants of TMPRSS2 inhibition. [49,50]

HCV NS3/4A inhibitors

Structure-based virtual screening of 500 RECAP-generated compounds, followed by detailed evaluation of the top 200 candidates using LigPlot and GB/VI analyses, identified 12 novel HCV NS3/4A protease inhibitors. Among these, compound 12 emerged as the most promising, exhibiting the highest docking score (−14.66 kJ/mol), strong binding affinity (−7.05 kJ/mol), and favorable solvation energy (−50.0 kJ/mol), while binding to the NS3/4A active site through interactions with key residues including His57, Asp81, Arg123, Lys136, Ala157, and Cys159. Complementary binary-QSAR

screening of ~522,000 compounds from BindingDB, NCI, and Specs-SC databases, followed by toxicity filtering, docking, molecular dynamics, and pharmacophore-based analyses, identified three additional candidates (140–142) in figure.2 with high ligand efficiency. These inhibitors selectively target the HCV NS3 protease domain of genotype 3a, binding the catalytic triad residues His77, Asp101, and Ser159 via hydrogen bonding, hydrophobic interactions, and water-mediated bridges, with reference drugs telaprevir and sofosbuvir guiding the screening

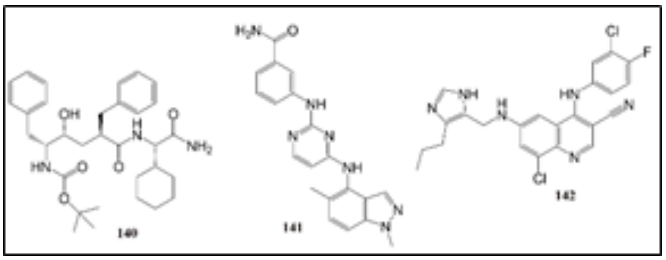

strategy. [51,52]

Figure.2

Norovirus 3CLPro inhibitors

High-throughput screening of ~300 compounds combined with molecular docking identified a novel class of peptidomimetic aldehydes as potent norovirus inhibitors, with compound 10d emerging as the lead candidate. Compound 10d exhibited nanomolar antiviral activity against murine norovirus (EC_{50} = 0.037 ± 0.016 μM) and human norovirus (EC_{50} = 0.012 ± 0.010 μM), effectively suppressing viral replication in vitro and in animal models. Mechanistically, it binds to the HuNoV 3CL protease active site via a covalent linkage with the catalytic residue Cys139 and forms stabilizing hydrogen bonds with Ile135, Gly137, Asp138, Pro136, and Arg112. The compound displayed high selectivity for the norovirus protease, broad-spectrum activity against GI, GII, and GV genotypes (IC_{50} = 0.09, 0.12, and 0.49 μM, respectively), strong performance in FRET-based protease assays, inhibition of the HuNoV GI.1 replicon, and demonstrated in vivo efficacy in zebrafish larvae, supporting its potential for clinical development. [53]

HIV-1 protease inhibitors

Ligand-based virtual screening of over 38,000 compounds using DRUDIT, followed by induced-fit docking, identified compounds NSC672457 and NSC669704 as promising HIV-1 protease inhibitors with an optimal balance between on-target potency and off-target liability; these compounds bind to the HIV-1 protease active site, interacting with catalytic residues Asp25, Asp29, and Asp30, and forming hydrogen bonds with Ile50, Gly48, and Gly49 in an extended binding conformation, while showing low affinity for off-targets such as EGFR, IGF1R, and ALK, thereby potentially reducing adverse metabolic and cardiovascular effects [54].

A complementary ligand-based pharmacophore modeling and large-scale 3D similarity screening of over 111 million compounds identified 14 inhibitor candidates, with HPS/002 and HPS/004 emerging as the most potent (~90% inhibition) due to favorable IC_{50} values and drug-like ADMET profiles; these compounds bind the active site through hydrogen bonding and π–π interactions with Asp25, Gly27, Asp29, Asp30, and Ile50, although potential hERG II inhibition and CYP3A4-mediated metabolism were noted [55].

AI-based screening of 250,000 compounds using deep learning models identified ZINC991374169 as a promising inhibitor that binds to the dimer-interface active site containing catalytic Asp25 and stabilizes the protease in a closed conformation [56].

Structure-guided synthesis of phenol- and polyphenol-based inhibitors yielded compound 15f, which exhibited low-

picomolar enzymatic potency (2.4 pM), strong activity against darunavir-resistant HIV-1 variants, and critical hydrogen-bonding, hydrophobic, and π–π interactions within the S2 subsite involving Val82, Thr80, Arg8, and Ile50, with analogue 148 showing comparable but slightly reduced activity [57]. Similarly, pyrimidine-based inhibitor 10e demonstrated nanomolar potency (IC_{50} = 2.53 nM), low cytotoxicity, ~68% in vivo inhibition, and effective binding to the active site via hydrogen bonds with Asp29, Gly48, and Ile50 (chains A and B) and van der Waals interactions, displaying an activity spectrum comparable to that of compound 147 against darunavir-resistant HIV-1 [58].

ZIKV NS2B-NS3 inhibitors

Large-scale virtual and experimental screening efforts have identified several ZIKV NS2B–NS3 protease inhibitors with diverse binding modes. Virtual docking of approximately seven million compounds using the Molsoft ICM-Pro package identified six inhibitors with IC_{50} values ranging from 3.8 to 14.4 μM that bind a novel allosteric pocket in the “super-open” conformation of the protease rather than the catalytic site, interacting primarily with hydrophobic residues W83, L85, V146, I147, G148, and L149, along with Q74, T118, D120, and I123; among these, compound RI07 emerged as the most promising (IC_{50} = 3.8 μM), with its aminobenzamide moiety engaging hydrophobic residues (L76, W83, L85, V146, I147, G148, L149), amide oxygens forming hydrogen bonds with V155 and N152, and a phenylquinoline group conferring rigidity and optimal fit within the pocket [59].

Consensus docking of 1,176 compounds using GOLD and DockThor, followed by cell-based antiviral assays, identified carbohydrate derivative BR020325 as the only hit showing antiviral activity against ZIKV PE243 (~40% inhibition, EC_{50} > 12.5 μM), interacting with Tyr130, Ser135, Gly153, and Tyr161, including the catalytic Ser135, although its selectivity index requires further optimization [60].

Experimental screening of 2,320 compounds from the MNHN library identified compound 945, a benzoic acid derivative (2-(3-methoxyphenoxy) benzoic acid), as a competitive inhibitor of the NS2B–NS3 protease (IC_{50} = 1.34 μM; K_i = 0.49 mM), forming hydrogen bonds with catalytic Ser135 and Thr134, π–π stacking interactions with His51 and Tyr161, and hydrophobic contacts with Ala132, though further structural optimization is needed [61]. Additionally, a machine learning–based QSAR and structure-based screening of 2,864 natural compounds highlighted streptomycin as a strong binder (ΔG = −20.81 kcal/mol), forming stable hydrogen bonds with Asn129 and Asn152 and hydrophobic interactions with Val87 during molecular dynamics simulations, suggesting its scaffold may inform the design of selective antiviral inhibitors despite its established antibacterial use [62].

Dengue virus NS2B/NS3

High-throughput screening using the DENV2proHeLa luciferase reporter system, integrating membrane permeability, metabolic stability, and cytotoxicity assessments, identified several promising DENV NS2B–NS3 protease inhibitors. Compound 20, with a hexanoic acid cap, showed nearly six-fold higher activity than a valeric acid cap, exhibiting an IC_{50} of 11 ± 0.7 μM and K_i of 9.8 μM; it binds the active site with the positively charged phenylguanidine in the S1 pocket interacting with a negatively charged aspartate, (4-benzyloxy)-L-phenylglycine in

S2, and hexanoic acid and 4-phenoxybenzoic acid caps in S3 and S4, forming lipophilic and π–π-stacking interactions with catalytic histidine [63].

Retropeptide-inspired thiazole derivatives 3aq and 3au, bearing –OH and $–OCH_3$ substituents, exhibited uncompetitive inhibition against DENV2 NS2B–NS3 protease (IC_{50} = 4.47 ± 0.41 μM and 7.38 ± 0.60 μM) and also inhibited JEV (IC_{50} = 1.03 ± 0.21 μM and 1.16 ± 0.16 μM), interacting via hydrogen bonds with Asp129, Phe130, Tyr150 and hydrophobic contacts with His51, Ser135, Gly151, Asp75, and Asn152 in S1′, S2, and S3 subpockets, although binding did not directly involve the known active site [64].

Virtual screening of 22 curcumin analogues identified compounds compounds 3, 10, and 13 with binding free energies of –15.2, –13.66, and –13.68 kcal/mol, comparable to panduratin A (–16.32 kcal/mol); all three interact with Lys74 in an allosteric site, with compound 13 showing the strongest hydrogen bonds to Lys74 and Asn162 and hydrophobic interactions with His51, achieving target inhibition of 73–83% in bioassays [65].

Hybrid pharmacophore scaffolds combining oxadiazole, arylsulfonamide, and phthalimide moieties produced compounds 8g (IC_{50} = 13.9 μM) and 8h (IC_{50} = 15.1 μM), binding an allosteric site in the open conformation via hydrogen bonds with Trp83 and Asn167, hydrophobic interactions, and dipole-dipole contacts with Thr118 [66].

A library of noncharged small-molecule benzamide derivatives showed competitive inhibition of DENV2 protease, with EC_{50} values from 0.24 to 2.2 μM; compound 71 exhibited submicromolar activity (EC_{50} = 0.24 μM), high selectivity against off-target proteases, and negligible cytotoxicity,

, binding the active site competitively in the region occupied by aprotinin [67].

Glycyrrhizic acid conjugates and dipeptide esters screened via docking and validated with FRET assays identified compounds 11, 17, and 19 as potent inhibitors (IC_{50} < 1 μM) that bind the hydrophobic catalytic pocket of DENV NS3 protease in an open, inactive conformation; 11 and 17 form hydrogen bonds with Asp75, Tyr150, and Gly153, with 162 additionally engaging His51, while 19 hydrogen bonds with Gly153, and the compounds demonstrated low cytotoxicity (CC_{50} > 100 μM) and high selectivity (SI > 2000 for 162) [68].

HSV-1 protease inhibitors

Pachota et al. designed and synthesized a library of structurally diverse HSV-1 capsid protease inhibitors featuring chiral bicyclic skeletons with one or two nitrogen atoms (amine/imine) substituted with aminophosphonic or sulfonamide groups, motifs common in antiviral drugs. From this library, compounds EWDI/39/55BF and KI207M were identified as potent inhibitors, with IC_{50} values of 1.31 ± 0.50 μM and 0.53 ± 0.21 μM by qPCR, and 2.35 ± 2.38 μM and 0.93 ± 0.35 μM in Vero E6 plaque assays, respectively. Compound KI207M binds the known active site of HSV-1 protease, forming an irreversible interaction with the catalytic serine via its amino-phosphonate moiety, conferring superior potency compared to EWDI/39/55BF, which is less effective against clinical HSV-1 strains. The structure–activity relationship highlights the importance of the chiral bicyclic skeleton, amine/imine functionality, and phosphonate or sulfonamide substituents, with groups such as N,N-dimethylnaphthalen-1-amine enhancing antiviral activity. Both EWDI/39/55BF and KI207M showed no systemic or local toxicity in animal models,with KI207M

effectively inhibiting HSV-1 replication and protecting animals in lethal challenge studies, indicating potential for monotherapy or combination therapy, though further studies are needed to assess oral delivery and systemic treatment suitability [69].

Pan-alphavirus protease inhibitors

Ghoshal et al. synthesized N-alkyl sulfamates as a novel class of nsP2 cysteine protease inhibitors, using reverse amide scaffolds with sulfamate warheads designed to enhance anti-nsP2pro activity while improving GSH stability and reducing GST-mediated metabolism. Biochemical assays, fluorescence-based chemoproteomics, and metabolic stability studies in mouse hepatocytes, along with infectious alphavirus testing (CHIKV, MAYV, VEEV), identified N-methyl sulfamate 5 as a potent and selective inhibitor. N-methyl sulfamate 5 binds the known active site of nsP2 protease, likely targeting a catalytic cysteine, and shows at least 30-fold selectivity for CHIKV nsP2pro over other cysteine proteases (cathepsin L, USP7, UCHL1, SARS-CoV-2 PLpro), with negligible off-target inhibition. It exhibits high potency (IC_{50} = 0.5 μM against CHIKV nsP2), low GSH reactivity, strong proteome-wide selectivity, and effectively reduces viral titers, inhibiting replication of VEEV-nLuc and CHIKV-nLuc reporter viruses with EC_{50} ~100 nM, establishing it as a promising covalent chemotype for alphavirus protease inhibition [70].

Enterovirus 71 protease inhibitors

To identify potent enterovirus 71 (EV71) protease inhibitors, virtual screening of 2,300 Traditional Chinese Medicine monomers and derivatives was performed targeting the 2A protease inhibitor-binding pocket, followed by antiviral evaluation and MD simulations. Etoposide, a derivative of epipodophyllotoxin, emerged as the lead compound with EC_{50} values of 1.628 ± 0.764 μM in RD cells, 2.329 ± 0.276 μM in HEK-293T cells, and 1.230 ± 1.561 μM in Vero cells, and a ΔG_MMGBSA of –34.28 kcal/mol. It binds to residues Tyr89 and Pro107 in the EV71 2A protease pocket via van der Waals and hydrogen-bond interactions, without interacting with the catalytic active site residues His21, Asp39, and Cys110. Etoposide effectively inhibits replication of multiple EV71 strains (A, B, C, and CVA16) across cell lines with minimal cytotoxicity, acting through selective inhibition of the 2A protease as supported by MD simulations and site-directed mutagenesis assays [71].

Conclusion

Overall, the summarized studies highlight viral proteases as broadly druggable targets across multiple RNA and DNA viruses, including SARS-CoV-2, other coronaviruses, HIV-1, HCV, dengue virus (DENV), Zika virus (ZIKV), norovirus, enterovirus 71, alphaviruses (CHIKV, VEEV, MAYV), and herpes simplex virus-1 (HSV-1). Effective inhibitors were identified using peptides, small molecules, natural products, peptidomimetics, covalent and noncovalent scaffolds, and AI-driven approaches. Across viruses, potency is driven by conserved interactions with catalytic residues (e.g., Cys, Ser, Asp/His triads) and key substrate-binding pockets, while both active-site and allosteric mechanisms contribute to antiviral activity and resistance management.

Despite frequent nanomolar biochemical potency and strong cellular antiviral effects, many inhibitors face shared translational challenges, including limited bioavailability, metabolic instability,

and off-target toxicity. Covalent inhibitors often provide superior potency against cysteine or serine proteases but require careful tuning of electrophilicity, whereas noncovalent and nonpeptidic inhibitors tend to offer improved selectivity and drug-like properties. Advances in high-throughput screening, structure-based design, machine learning, and fragment-based optimization have substantially accelerated discovery across viral families.

In conclusion, integrating structural biology, computational screening, medicinal chemistry, and in vivo pharmacokinetic evaluation is essential to translate potent viral protease inhibitors into safe, orally available, and resistance-resilient antivirals for current and emerging viral infections.

References

1. Aguilera-Pesantes, D., et al. "Discovering key residues of dengue virus NS2b-NS3-protease: New binding sites for antiviral inhibitors design." Biochemical and Biophysical Research Communications 492.4 (2017): 631-642.
2. Chen, Wan-Na, et al. "The dengue virus NS2B–NS3 protease retains the closed conformation in the complex with BPTI." FEBS letters 588.14 (2014): 2206-2211.
3. De Francesco, R., and C. Steinkühler. "Structure and function of the hepatitis C virus NS3-NS4A serine proteinase." The Hepatitis C Viruses (2000): 149-169.
4. Meeprasert, Arthitaya, Supot Hannongbua, and Thanyada Rungrotmongkol. "Key binding and susceptibility of NS3/4A serine protease inhibitors against hepatitis C virus." Journal of Chemical Information and Modeling 54.4 (2014): 1208-1217.
5. Robilotti, Elizabeth, Stan Deresinski, and Benjamin A. Pinsky. "Norovirus." Clinical microbiology reviews 28.1 (2015): 134-164.
6. Takahashi, Daisuke, et al. "Structural and dynamics characterization of norovirus protease." Protein Science 22.3 (2013): 347-357.
7. Mager, Peter P. "The active site of HIV-1 protease." Medicinal research reviews 21.4 (2001): 348-353.
8. Hilgenfeld, Rolf, Jian Lei, and Linlin Zhang. "The structure of the zika virus protease, NS2B/NS3pro." Dengue and Zika: Control and Antiviral Treatment Strategies (2018): 131-145.
9. Nitsche, Christoph. "Proteases from dengue, West Nile and Zika viruses as drug targets." Biophysical reviews 11.2 (2019): 157-165.
10. Gao, Min, et al. "The protease of herpes simplex virus type 1 is essential for functional capsid formation and viral growth." Journal of virology 68.6 (1994): 3702-3712.
11. Dilanni, C. L., et al. "Identification of the herpes simplex virus-1 protease cleavage sites by direct sequence analysis of autoproteolytic cleavage products." Journal of Biological Chemistry 268.3 (1993): 2048-2051.
12. Eberle, Raphael J et al. “Discovery of All-d-Peptide Inhibitors of SARS-CoV-2 3C-like Protease.” ACS chemical biology vol. 18,2 (2023): 315-330.
Xiong, Muya et al. “In silico screening-based discovery of novel covalent inhibitors of the
13. SARS-CoV-2 3CL protease.” European journal of medicinal chemistry vol. 231 (2022): 114130.
14. Hung, Hui-Chen et al. “Discovery of M Protease Inhibitors Encoded by SARS-CoV-2.” Antimicrobial agents and chemotherapy vol. 64,9 e00872-20. 20 Aug. 2020
15. Mondal, Santanu et al. “Dual Inhibitors of Main Protease (MPro) and Cathepsin L as Potent Antivirals against SARS-CoV2.”

Journal of the American Chemical Society vol. 144,46 (2022): 21035-21045.
16. Flury, Philipp, et al. "Azapeptide-based SARS-CoV-2 Main Protease Inhibitors: Design, Synthesis, Enzyme Inhibition, Structural Determination, and Antiviral Activity." (2025).
17. Ghosh, Rajesh et al. “Identification of alkaloids from Justicia adhatoda as potent SARS CoV-2 main protease inhibitors: An in silico perspective.” Journal of molecular structure vol. 1229 (2021): 129489.
18. Scholle, Michael D., et al. "Label-free duplex SAMDI-MS screen reveals novel SARS-CoV-2 3CLpro inhibitors." Antiviral Research 200 (2022): 105279.
19. Lu, Jiani, et al. "Identifying Exifone as a Dual-Target Agent Targeting Both SARS-CoV-2 3CL Protease and the ACE2/S-RBD Interaction Among Clinical Polyphenolic Compounds." International Journal of Molecular Sciences 26.5 (2025): 2243.
20. Ton, Anh-Tien, et al. "Rapid identification of potential inhibitors of SARS-CoV-2 main protease by deep docking of 1.3 billion compounds." Molecular informatics 39.8 (2020): 2000028.
21. Singh, Arshdeep, et al. "Exploration of the anti-SARS-CoV-2 potential and expected mechanisms of small molecules from Antrodia cinnamomea by BT&D2 drug-targeting analysis." Bioorganic Chemistry (2025): 108646.
22. Unoh, Yuto, et al. "Discovery of S-217622, a noncovalent oral SARS-CoV-2 3CL protease inhibitor clinical candidate for treating COVID-19." Journal of medicinal chemistry 65.9 (2022): 6499-6512.
23. Huff, Sarah, et al. "Discovery and mechanism of SARS-CoV-2 main protease inhibitors." Journal of medicinal chemistry 65.4 (2021): 2866-2879.
24. Elagawany, Mohamed, et al. "Ligand-based design, synthesis, computational insights, and in vitro studies of novel N-(5-Nitrothiazol-2-yl)-carboxamido derivatives as potent inhibitors of SARS-CoV-2 main protease." Journal of Enzyme 1.Inhibition and Medicinal Chemistry 37.1 (2022): 2112-2132.
25. Joshi, Tanuja, et al. "Structure-based screening of novel lichen compounds against SARS Coronavirus main protease (Mpro) as potentials inhibitors of COVID-19." Molecular Diversity 25.3 (2021): 1665-1677.
26. Dong, Jie, et al. "Ligand-based discovery of coronavirus main protease inhibitors using MACAW molecular embeddings." Journal of Enzyme Inhibition and Medicinal Chemistry 38.1 (2023): 24-35.
27. Suriya, Utid, et al. "Design and Evaluation of Andrographolide Analogues as SARS-CoV-2 Main Protease Inhibitors: Molecular Modeling and in vitro Studies." Drug Design, Development and Therapy (2025): 3907-3924.
28. Brier, Lucile et al. “Novel dithiocarbamates selectively inhibit 3CL protease of SARS-CoV-2 and other coronaviruses.” European journal of medicinal chemistry vol. 250 (2023): 115186.
29. Chan, Lee-Chin et al. “Inhibition of SARS-CoV-2 3CL protease by the anti-viral chimeric protein RetroMAD1.” Scientific reports vol. 13,1 20178. 17 Nov. 2023.
30. Zian, Debora, et al. "The efficiency of high-throughput screening (HTS) and in-silico data analysis during medical emergencies: Identification of effective antiviral 3CLpro inhibitors." Antiviral Research 237 (2025): 106119.
31. Motiwale, Mohit et al. “Finding potent inhibitors for COVID-19 main protease (Mpro): an in silico approach using SARS-CoV-3CL protease inhibitors for combating CORONA.”

Journal of biomolecular structure & dynamics vol. 40,4 (2022): 1534-1545.
32. Ghosh, Rajesh, et al. "Evaluation of green tea polyphenols as novel corona virus (SARS CoV-2) main protease (Mpro) inhibitors–an in silico docking and molecular dynamics simulation study." Journal of Biomolecular Structure and Dynamics 39.12 (2021): 4362-4374.
33. Wu, Jing et al. “Synthesis and Biochemical Evaluation of 8H-Indeno[1,2-d]thiazole Derivatives as Novel SARS-CoV-2 3CL Protease Inhibitors.” Molecules (Basel, Switzerland) vol. 27,10 3359. 23 May. 2022.
34. Boby, Melissa L et al. “Open science discovery of potent noncovalent SARS-CoV-2 main protease inhibitors.” Science (New York, N.Y.) vol. 382,6671 (2023): eabo7201.
35. Guo, Sheng et al. “Discovery of novel inhibitors against main protease (Mpro) of SARS-CoV-2 via virtual screening and biochemical evaluation.” Bioorganic chemistry vol. 110 (2021): 104767.
36. .Narayanan, Anoop et al. “Identification of SARS-CoV-2 inhibitors targeting Mpro and PLpro using in-cell-protease assay.” Communications biology vol. 5,1 169. 25 Feb. 2022.
37. M. Bader, Stefanie, et al. "A novel PLpro inhibitor improves outcomes in a pre-clinical model of long COVID." Nature Communications 16.1 (2025): 2900.
38. Wang, Qian et al. “Structure-Based Design of Potent Peptidomimetic Inhibitors Covalently Targeting SARS-CoV-2 Papain-like Protease.” International journal of molecular sciences vol. 24,10 8633. 11 May. 2023
39. Jamalan, Mostafa et al. “Structure-Based Screening to Discover New Inhibitors for Papain-like Proteinase of SARS-CoV-2: An In Silico Study.” Journal of proteome research vol. 20,1 (2021): 1015-1026.
40. Ma, Chunlong et al. “Discovery of SARS-CoV-2 Papain-like Protease Inhibitors through a Combination of High-Throughput Screening and a FlipGFP-Based Reporter Assay.” ACS central science vol. 7,7 (2021): 1245-1260.
41. Tan, Bin et al. “Design of a SARS-CoV-2 papain-like protease inhibitor with antiviral efficacy in a mouse model.” Science (New York, N.Y.) vol. 383,6690 (2024): 1434-1440.
42. Jadhav, Prakash, et al. "Structure-based design of SARS-CoV-2 papain-like protease inhibitors." European journal of medicinal chemistry 264 (2024): 116011.
43. Stasiulewicz, Adam, et al. "SARS-CoV-2 papain-like protease potential inhibitors — in silico quantitative assessment." International journal of molecular sciences 22.8 (2021): 3957.
44. Alici, Hakan. "Structure-Based Design and In-Silico Evaluation of Computationally Proposed Curcumin Derivatives as Potential Inhibitors of the Coronaviral PLpro Enzymes." Pharmaceuticals 18.6 (2025): 798.
45. Weglarz-Tomczak, Ewelina, et al. "Identification of ebselen and its analogues as potent covalent inhibitors of papain-like protease from SARS-CoV-2." Scientific reports 11.1 (2021): 3640.
46. Arya, R, et al. "Potential inhibitors against papain-like protease of novel coronavirus (COVID-19) from FDA approved drugs." ChemRxiv. (2020); doi:10.26434/chemrxiv.11860011.v2
47. Bingül, Alev Arslantürk, and Necmettin Pirinççioğlu. "The Virtual Screening and Molecular Docking Study of New Inhibitors for SARS-COV-2 Papain-Like Protease (PLpro)." Ata-Kimya Dergisi 5.1 (2025): 28-37.
48. Lu, Yongzhi, et al. "Discovery of orally bioavailable SARS-CoV-2 papain-like protease inhibitor as a potential treatment

for COVID-19." Nature Communications 15.1 (2024): 10169.
49. Wang, Shuo, Xuexun Fang, and Ye Wang. "In silico screening of novel TMPRSS2 inhibitors for treatment of COVID-19." Molecules 27.13 (2022): 4210.
50. Parameswaran, Dakshinesh, et al. "In silico approach for uncovering inhibitors of SARS-CoV-2 by targeting TMPRSS2 via molecular networking-based strategies." Indian Journal of Biochemistry and Biophysics (IJBB) 62.5 (2025): 544-559.
51. Riaz, Muhammad et al. “A Novel Approach to Develop New and Potent Inhibitors for the Simultaneous Inhibition of Protease and Helicase Activities of HCV NS3/4A Protease: A Computational Approach.” Molecules (Basel, Switzerland) vol. 28,3 1300. 29 Jan. 2023.
52. Ikram, Saima et al. “Potent novel inhibitors against hepatitis C virus NS3 (HCV NS3 GT-3a) protease domain.” Journal of molecular graphics & modelling vol. 101 (2020): 107727.
53. Van Dycke, Jana, et al. "A novel class of norovirus inhibitors targeting the viral protease with potent antiviral activity in vitro and in vivo." Viruses 13.9 (2021): 1852.
54. La Monica, Gabriele, et al. "Off-target-based design of selective hiv-1 protease inhibitors." International Journal of Molecular Sciences 22.11 (2021): 6070.
55. Okafor, Sunday N., Pavimol Angsantikul, and Hashim Ahmed. "Discovery of novel HIV protease inhibitors using modern computational techniques." International Journal of Molecular Sciences 23.20 (2022): 12149.
56. Arrigoni, Roberto, et al. "AI-aided search for new HIV-1 protease ligands." Biomolecules 13.5 (2023): 858.
57. Ma, Ling, et al. "Design and Evaluation of Novel HIV-1 Protease Inhibitors Containing Phenols or Polyphenols as P2 ligands with High Activity against DRV-Resistant HIV-1 Variants." International Journal of Molecular Sciences 23.22 (2022): 14178.
58. Zhu, Mei, et al. "Preliminary SAR and biological evaluation of potent HIV-1 protease inhibitors with pyrimidine bases as novel P2 ligands to enhance activity against DRV-resistant HIV-1 1.variants." European Journal of Medicinal Chemistry 185 (2020): 111866.
59.Meewan, Ittipat, et al. "Allosteric inhibitors of Zika virus NS2B-NS3 protease targeting protease in “super-open” conformation." Viruses 15.5 (2023): 1106.
60. Marcelino e Oliveira, Fernanda Kelly, et al. "Discovery of Arylfuran and Carbohydrate Derivatives from the BraCoLi Library as Potential Zika Virus NS3pro Inhibitors." Future Pharmacology 5.1 (2025): 9.
61. Andrade, Milene Aparecida, et al. "Identification of novel Zika virus NS3 protease inhibitors with different inhibition modes by integrative experimental and computational approaches." Biochimie 212 (2023): 143-152.
62. Altayb, Hisham N., and Hanan Ali Alatawi. "Employing machine learning-based QSAR for targeting Zika Virus NS3 Protease: Molecular insights and inhibitor discovery." Pharmaceuticals 17.8 (2024): 1067.
63. Kühl, Nikos, et al. "A new class of dengue and West Nile virus protease inhibitors with submicromolar activity in reporter gene DENV-2 protease and viral replication assays." Journal of Medicinal Chemistry 63.15 (2020): 8179-8197.
64. Murtuja, S, et al. "Identification of novel thiazole derivatives as flaviviral protease inhibitors effective against Dengue (DENV2) and Japanese encephalitis viruses." Antimicrobial Agents and

and Chemotherapy 69.4 (2025): e01651-24.
65. Frimayanti, N, et al. "Insight into the in silico Study and Biological Evaluation of Curcumin Analogue Compounds as New Potential Inhibitors for Dengue DEN2 NS2B/NS3 Serine Protease."Sains Malaysiana 53.8 (2024): 1969-1980.
66. Hamdani, Syeda Shamila, et al. "Synthesis and evaluation of novel S-benzyl-and S-alkylphthalimide-oxadiazole-benzenesulfonamide hybrids as inhibitors of dengue virus protease."Bioorganic Chemistry 96 (2020): 103567.
67. Kühl, Nikos, et al. "Beyond basicity: discovery of nonbasic DENV-2 protease inhibitors with potent activity in cell culture." Journal of Medicinal Chemistry 64.8 (2021): 4567-4587.
68. Lin, Yu-Feng, et al. "Discovery of potent dengue virus NS2B-NS3 protease inhibitors among glycyrrhizic acid conjugates with amino acids and dipeptides esters." Viruses 16.12 (2024): 1926.1.Pachota, Magdalena, et al. "Novel inhibitors of HSV-1 protease effective in vitro and in vivo." Antiviral Research 213 (2023): 105604.
69. Ghoshal, Anirban, et al. "N-Alkyl Sulfamates as a New Class of nsP2 Cysteine Protease Inhibitors with Broad Spectrum Antialphaviral Activity." BioRxiv (2025): 2025-06.
70. Liang, Qinqin, et al. "Etoposide targets 2A protease to inhibit enterovirus 71 replication." Microbiology Spectrum 13.1 (2025): e02200-24.

Authors

Murtadha A. Alshaikh is a pharmacy graduate with research interests in medicinal chemistry and anticancer drug discovery.

Hussain H. Alsadah is a pharmacy graduate whose work focuses on experimental pharmacology and bioactive compound evaluation.

Mansour S. Alturki is a researcher with expertise in anticancer drug discovery, EGFR inhibitors, and computer-aided drug design.

The Impact of Sodium Dihydrogen Phosphate on Hydroxyapatite Formation and Wettability Alteration in Carbonates

Salem Alshammari*, Hussain Al-Saleem, Dong Kyu Cha, Subhash Ayiral[1] and Moataz Abu-Al-Saud
Reservoir Engineering Technology Division, EXPEC ARC, Saudi Aramco, Dhahran 31311, Saudi Arabia.
Corresponding author: salem.khaled.alshammari@gmail.com

Abstract

Carbonate reservoirs often exhibit oil-wet behavior due to interactions between positively charged calcite surfaces and acidic components of crude oil. While conventional wettability alteration methods in low-salinity waterflooding rely on double-layer effects, mineralogical surface transformation remains underexplored. This study investigates the impact of sodium dihydrogen phosphate (NaH_2PO_4) on hydroxyapatite formation and wettability alteration in carbonates. ζ potential measurements show a systematic shift toward more negative values with increasing phosphate concentration. High-pressure (1000 psig) and high-temperature (70 °C) contact angle measurements reveal a significant wettability transition from 136.03° to 90.44° upon addition of 500 ppm phosphate. Thermodynamic modeling and TEM/EDX analyses confirm phosphate-induced calcium phosphate formation at the calcite surface.

Introduction

Carbonate reservoirs contain a substantial fraction of global hydrocarbon resources, yet oil recovery from these formations is often limited by unfavorable wettability conditions [1]. Carbonate minerals, primarily calcite ($CaCO_3$), typically exhibit a positively charged surface under high-salinity conditions [2]. This surface charge promotes adsorption of negatively charged acidic components from crude oil, such as carboxylic groups, leading to oil-wet or mixed-wet states. Oil-wet conditions reduce spontaneous imbibition, increase capillary trapping, and ultimately lower recovery efficiency during waterflooding. Tuning ionic composition can alter rock surface electrostatics and wettability [3]. Mechanisms proposed in the literature include electrical double-layer expansion, multi-ion exchange, and surface complexation reactions [4]. Electrokinetic measurements, particularly ζ potential, have been widely used to characterize interfacial charge modification in carbonate/brine systems [5]. However, most studies focus on reversible electrostatic interactions rather than permanent mineralogical transformations at the rock surface. In this study, we investigate the impact of sodium dihydrogen phosphate on hydroxyapatite formation at the calcite interface and quantify its effect on wettability alteration. The objectives are to evaluate electrokinetic changes induced by phosphate addition, characterize mineralogical evidence of hydroxyapatite growth, and assess the relationship between surface transformation and wettability behavior. By linking interfacial

geochemistry to macroscopic wettability measurements, this work proposes a new recipe for wettability alteration in carbonates.

Methods

Oil/brine emulsions were prepared by dispersing a single droplet of crude oil into 5 mL of the respective brine solution. For calcite/brine suspensions, 0.1 g of finely ground calcite was added to 20 mL of brine and mixed thoroughly. Subsequently, 5 mL of this suspension was transferred into a new vial containing 15 mL of calcite-free brine to achieve consistent solid loading and ionic composition. Sonication was applied after each preparation step to minimize particle agglomeration and ensure uniform dispersion. Solid-to-liquid and liquid-to-liquid ratios were kept constant across all experiments to maintain reproducibility. ζ potential measurements were performed using phase-analysis light scattering (PALS) with a Brookhaven ZetaPALS instrument. In this technique, the phase shift 〈Q(t)〉 of the scattered light field is extracted directly from the Doppler signal using a digital signal processor, allowing determination of electrophoretic mobility.

$$\langle Q(t) - Q(0) \rangle = \langle A \rangle q \mu_e \int_0^t E(t')dt' \quad (1)$$

The induced electrical field in the electrochemical cell will cause colloidal particles to move with a velocity (v_s); this phenomenon is known as electrophoresis.

$$\vec{v_s} = \mu_e \vec{E} \quad (2)$$

The induced electrical field in the electrochemical cell will cause colloidal particles to move with a velocity (v_s); this phenomenon is known as electrophoresis.

$$\zeta = \eta \mu_e / \epsilon \quad (3)$$

We also performed chemical equilibrium calculations using PHREEQC [6] with the phreeqc.dat database. The calculations are based on the law of mass action which was used to calculate the molalties of each component.

$$\prod_i a_i^{\nu_i} = K(T) \exp \frac{(P - P^\circ)\,\Delta V}{RT} \quad (4)$$

The activity (ai = γi * mi) is used to account for non-ideality through the activity coefficient (γi); the activity coefficient model used is a modified version of the Debye-Hückel equation [7] which depends on the temperature, ionic strength and ion type as implemented in the phreeq.dat thermodynamic database in PHREEQC [6].

$$\log \gamma_i = -\frac{A z_i^2 \sqrt{I}}{1 + B \hat{a}_i \sqrt{I}} + b_i I \quad (5)$$

For contact angle measurements, tight carbonate chips were used as representative substrates. The chips were first saturated with formation brine, centrifuged to remove excess fluid, and subsequently aged in dead crude oil for four days to establish initial wettability conditions. The aged chip was then mounted in a high-pressure contact angle cell, and high-salinity brine was injected. Temperature and pressure were maintained at 70 °C and 1000 psig, respectively. An oil droplet was deposited onto the rock surface and allowed to reach equilibrium. The contact angle was determined using image analysis of the droplet profile. The procedure was repeated for brine containing 500 ppm sodium dihydrogen phosphate to evaluate the effect of phosphate addition on wettability. Finally, Transmission electron microscopy (TEM) was performed using a probe-corrected Titan C5 instrument (Thermo Fisher Scientific). Imaging was conducted in scanning transmission electron microscopy

(STEM) mode at an accelerating voltage of 200 kV. High-angle annular dark-field (HAADF) imaging provided Z-contrast, where image intensity scales approximately with atomic number. Following imaging, energy-dispersive X-ray spectroscopy (EDX) mapping was carried out to identify elemental distributions, with particular emphasis on calcium, oxygen, and phosphorus.

Results and Discussion

This study integrates electrokinetic measurements, wettability evaluation, thermodynamic modeling, and high-resolution microscopy to investigate the role of sodium dihydrogen phosphate (NaH_2PO_4) in modifying carbonate surface chemistry. Figure 1 illustrates the structure of the electrical double layer formed at a charged mineral surface in an aqueous electrolyte. When calcite is exposed to brine, surface charge develops due to ionization and specific adsorption of ionic species. Counter-ions accumulate near the surface forming the Stern layer, a compact region of specifically adsorbed ions. Beyond this region lies the diffuse layer, where ion distribution is governed by electrostatic forces and thermal motion. The ζ potential is not measured at the mineral surface itself but at the slipping plane. Therefore, ζ potential reflects the effective electrostatic potential governing particle–fluid interactions rather than the true surface potential.

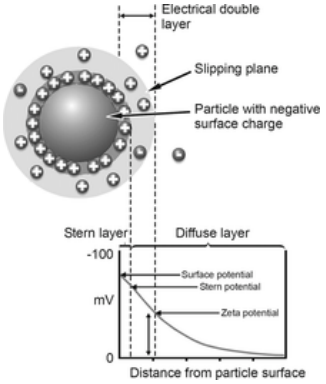

Figure 1: Illustration of the electric double layer showing the slipping plane at which ζ potential is defined [8].

Figure 2 presents the effect of NaH_2PO_4 concentration on ζ potential for both calcite/water suspensions and oil/water emulsions. In the absence of phosphate, calcite exhibits a slightly positive ζ potential under high-salinity conditions, consistent with literature for carbonate systems. Upon addition of phosphate, the ζ potential progressively shifts toward more negative values. At higher phosphate concentrations, the calcite suspension becomes distinctly negatively charged. On the other hand, oil/brine ζ potential remained negative at all concentrations and is less affected by the addition of NaH_2PO_4.

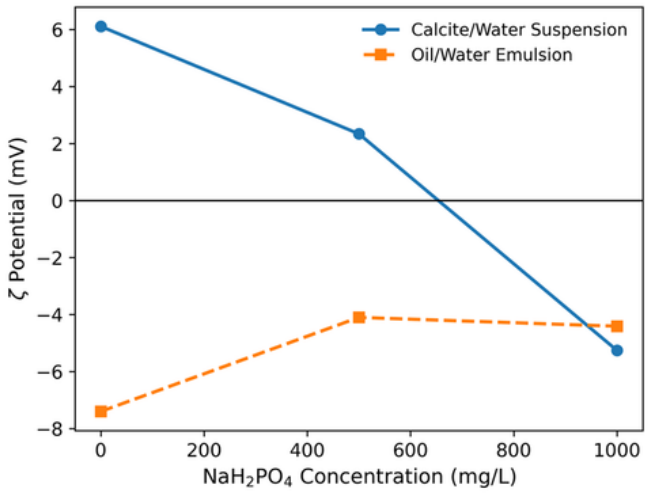

Figure 2: Effect of NaH_2PO_4 concentration on ζ potential for calcite/water suspension and oil/water emulsion systems.

Figure 3 shows contact angle measurements conducted at 70 °C and 1000 psig. In seawater without additive, the measured contact angle (136.03 ± 0.72°) indicates an oil-wet to intermediate-wet condition. Upon addition of 500 ppm NaH_2PO_4, the contact angle increases significantly (90.44 ± 3.80°), indicating a pronounced shift toward water-wet behavior. This change confirms that phosphate addition alters rock–fluid

interactions under reservoir-relevant conditions. The combination of ζ potential shift and significant contact angle change suggests that surface chemistry has been fundamentally modified. To further investigate this, we considered the chemical reactions relevant to this system (Figure 4). After modeling the system in PHREEQC, we found that the addition of sodium dihydrogen phosphate to seawater will make the solution a weak acid. Nevertheless, this acid reacts with carbonate formations resulting in the deprotonation of dihydrogen phosphate anions leading to the potential formation of hydroxyapatite minerals.

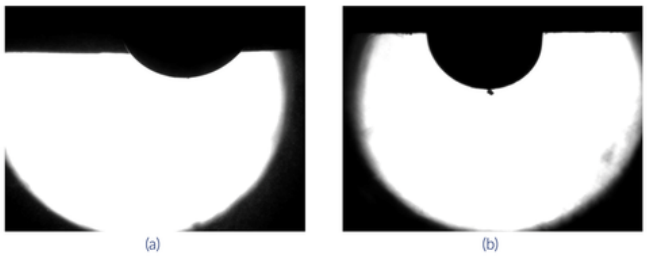

Figure 3: Contact angle measurements at T = 70 °C and P = 1000 psig with (a) seawater (θ = 136.03 ± 0.72) (b) seawater + 500 ppm NaH_2PO_4 (θ = 90.44 ± 3.80).

Transmission electron microscopy provides direct structural evidence supporting this interpretation. Figures 5 and 6 compare calcite particles aged in seawater with and without phosphate additive. In the absence of NaH_2PO_4 (Figure 5), HAADF-STEM imaging shows the expected morphology of calcite particles, and EDX mapping reveals strong calcium and oxygen signals with negligible phosphorus detection. In contrast, particles exposed to phosphate-containing brine (Figure 6) exhibit clear phosphorus enrichment co-localized with calcium. The spatial overlap of Ca and P signals indicates formation of a calcium phosphate phase at or near the calcite surface.

Chemical Equilibria

$$H_2PO_4^-(aq) \rightleftharpoons HPO_4^{2-}{}_{(aq)} + H^+_{(aq)} \quad (6)$$

$$CO_3^{2-}(aq) + H^+_{(aq)} \rightleftharpoons HCO_3^-{}_{(aq)} \quad (7)$$

$$HCO_3^-(aq) + H^+_{(aq)} \rightleftharpoons H_2CO_{3(aq)} \quad (8)$$

$$CaCO_{3(s)} \rightleftharpoons Ca^{2+}_{(aq)} + CO_3^{2-}{}_{(aq)} \quad (9)$$

$$3\,HPO_4^{2-}{}_{(aq)} + 5Ca^{2+}_{(aq)} + H_2O \rightleftharpoons 4H_{(aq)}^+ + Ca_5(PO_4)_3OH_{(s)} \quad (10)$$

Figure 4: Relevant aqueous speciation and mineral equilibrium reactions considered in PHREEQC modeling, including phosphate protonation equilibria, calcite dissolution, and hydroxyapatite precipitation reactions governing coupled dissolution–precipitation processes.

Phosphate chemistry provides a distinct mechanism for surface modification through coupled dissolution–precipitation reactions. Upon addition of NaH_2PO_4 to calcium-rich systems, partial calcite dissolution releases Ca^{2+} ions that react with phosphate species to form hydroxyapatite ($Ca_5(PO_4)_3OH$), a thermodynamically stable calcium phosphate phase. This process represents a mineralogical transformation of the carbonate surface rather than only an alteration of the electrical double layer.

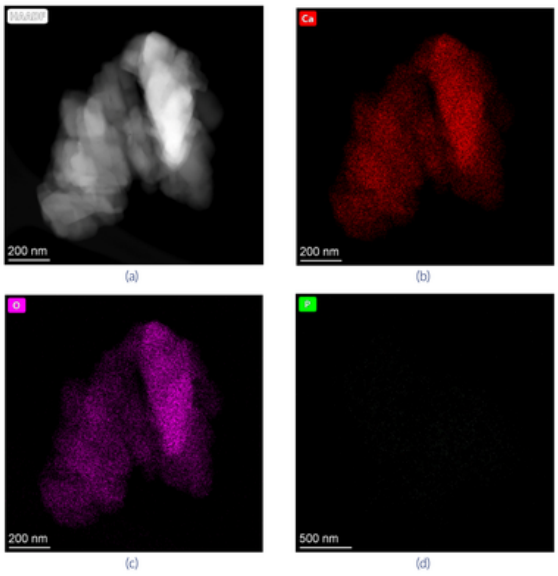

Figure 5: TEM for $CaCO_3$ particles (aged in seawater) (a) HAADF Image in STEM Mode and EDX mapping in STEM Mode (b-d) where each show (b) Calcium, (c) Oxygen and (d) phosphorous.

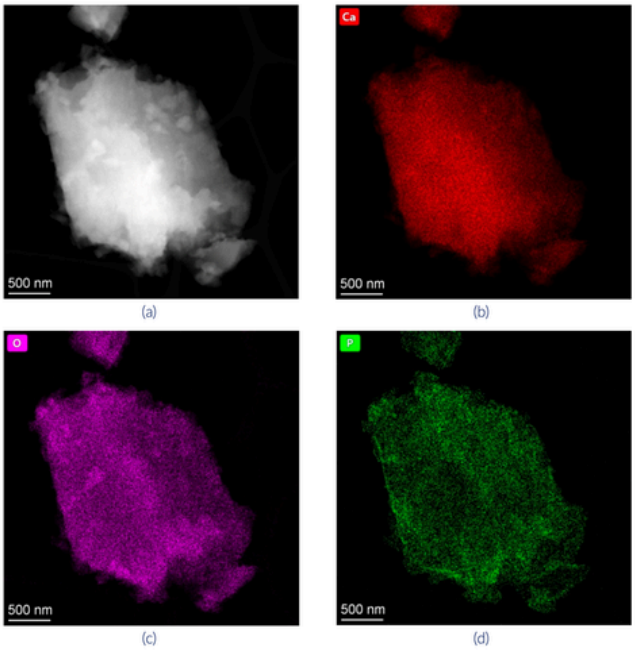

Figure 6: TEM for $CaCO_3$ particles (aged in seawater and 500 ppm [NaH_2PO_4]) (a) HAADF Image in STEM Mode and EDX mapping in STEM Mode (b-d) where each show (b) Calcium, (c) Oxygen and (d) phosphorous.

Conclusion

This study demonstrates that sodium dihydrogen phosphate induces wettability alteration in carbonate systems through a mineralogical transformation mechanism rather than purely electrostatic effects. ζ potential measurements revealed systematic interfacial charge modification with increasing phosphate concentration. High-pressure contact angle measurements confirmed a significant shift toward water-wet behavior under reservoir-relevant conditions. Thermodynamic modeling indicated that phosphate addition promotes hydroxyapatite formation via coupled dissolution–precipitation reactions involving calcite-derived Ca^{2+}. Direct TEM and EDX evidence confirmed phosphorus enrichment at the carbonate surface, supporting calcium phosphate formation. Unlike conventional smart water approaches that rely on reversible electrical double-layer modification, the mechanism proposed here involves surface conversion of calcite to a thermodynamically stable calcium phosphate phase. This mineral-engineering pathway provides a more persistent modification of surface chemistry and interfacial reactivity. The results suggest that targeted phosphate chemistry may offer a durable and controllable strategy for wettability alteration in carbonate reservoirs. Future work should evaluate long-term stability, flow-through conditions, and core-scale recovery performance to assess field applicability.

References

[1] W.G. Anderson, Wettability Literature Survey- Part 1: Rock/Oil/Brine Interactions and the Effects of Core Handling on Wettability, Journal of Petroleum Technology 38 (1986) 1125–1144. https://doi.org/10.2118/13932-PA.

[2] M.P. Yutkin, H. Mishra, T.W. Patzek, J. Lee, C.J. Radke, Bulk and Surface Aqueous Speciation of Calcite: Implications for Low-Salinity Waterflooding of Carbonate Reservoirs, SPE Journal 23 (2018) 84–101. https://doi.org/10.2118/182829-PA.

[3] A.A. Yousef, S. Al-Saleh, A. Al-Kaabi, M. Al-Jawfi, Laboratory Investigation of the Impact of Injection-Water Salinity and Ionic Content on Oil Recovery From Carbonate Reservoirs, SPE Reservoir Evaluation & Engineering 14 (2011) 578–593. https://doi.org/10.2118/137634-PA.

[4] J.J. Sheng, Critical review of low-salinity waterflooding, Journal of Petroleum Science and Engineering 120 (2014) 216–224. https://doi.org/10.1016/j.petrol.2014.05.026.

[5] A.O. Alghamdi, M.O. Abu-Al-Saud, M.B. Al-Otaibi, S.C. Ayirala, A. Alyousef, Electro-kinetic induced wettability alteration in carbonates: Tailored water

chemistry and alkali effects, Colloids and Surfaces A: Physicochemical and Engineering Aspects 583 (2019) 123887. https://doi.org/10.1016/j.colsurfa.2019.123887.
[6] D. Parkhurst, C.A.J. Appelo, Description of Input and Examples for PHREEQC Version 3—A Computer Program for Speciation, Batch-Reaction, One-Dimensional Transport, and Inverse Geochemical Calculations, US Geological Survey Techniques and Methods 6 (2013) 497.
[7] D.C. Melchior, R.L. Bassett, eds., Chemical Modeling of Aqueous Systems II, American Chemical Society, Washington, DC, 1990. https://doi.org/10.1021/bk-1990-0416.
[8] M. Domingues, N. Santos, Laser-Light Scattering Approach to Peptide–Membrane Interaction, Membrane-active Peptides: Methods and Results on Structure and Function, ed. Castanho, MARB, International University Line, La Jolla, California, USA, 2010.

Authors

Salem Alshammari is a Research Engineer at EXPEC ARC, Saudi Aramco. He has authored and co-authored eight peer-reviewed journal papers and more than ten conference proceedings in areas spanning molecular simulation, chemical thermodynamics, brine chemistry, and improved oil recovery.

Hussain Saleem is a laboratory specialist at EXPEC ARC with more than 10 years of experience in analytical chemistry, enhanced oil recovery, and lab management. He has authored and co-authored multiple conference papers and holds four granted patents, with extensive experience in field deployments.

Dong Kyu Cha is a researcher in EXPEC ARC with over 10,000 citations and an h-index of 42. He has published extensively in leading international journals on surface chemistry, multiphase systems, and functional materials.

Subhash Ayirala is a Petroleum Engineering Consultant with over 20 years of industry experience, specializing in waterflooding, SmartWater EOR, produced-water management, CO_2 mineralization, and CCUS. He has authored and co-authored 88 journal papers and 130 conference papers, holds 68 granted patents, and is a highly recognized SPE leader and award recipient for technical excellence and service.

Moataz Abu-AlSaud is a Focus Area Champion at Saudi Aramco EXPEC Advanced Research Center, specializing in multiphase flow in porous media and improved oil recovery. He holds bachelor's degrees in mechanical engineering and mathematics from Rice University, a master's degree in mechanical engineering from King Abdullah University of Science and Technology, and a PhD in energy resources engineering from Stanford University.

Editorial Board

Dr. Shakeel Ahmed (Editor in Chief)

Dr. Shakeel Ahmed is a Research Scientist at the IRC for Refining & Advanced Chemicals at King Fahd University of Petroleum & Minerals. His primary areas of expertise include industrial catalysis, inorganic synthesis, and instrumental analysis. With over 200 publications and 77 co-invented patents to his name, Dr. Shakeel has made significant contributions to his field. He has been honored with numerous national and international awards and is recognized among the top 2% of scientists worldwide.

Dr. SK Safdar Hossain

Dr. SK Safdar Hossain is a Professor of Chemical Engineering at King Faisal University. He earned his Ph.D. in Catalysis from King Fahd University of Petroleum & Minerals (KFUPM). His research focuses on reaction engineering, energy storage devices, and chemical process control. He has published over seventy-five peer-reviewed articles and is a co-inventor on fifteen United States patents. Dr. Hossain is a Senior Member of the American Institute of Chemical Engineers (AIChE) and a Life Member of the Indian Institute of Chemical Engineers (IIChE).

Dr. Mansour Saleh Alturki

Dr. Mansour Saleh Alturki, Assistant Professor of Medicinal Chemistry at Imam Abdulrahman Bin Faisal University, specializes in synthetic chemistry and drug discovery targeting metabolic disorders, infectious diseases, and cancer. With 23+ years of experience, his expertise includes computational drug design, ADMET profiling, molecular dynamics, and AI-driven research in human health innovations.

Ms. Hissah Alqahtani

Ms. Hissah Alqahtani is a Lecturer in Physical Chemistry at Al Yamamah University, specializing in electrochemistry and advanced materials for energy and environmental applications. With expertise in corrosion, supercapacitors, solar cells, and water treatment, she has published extensively and holds three patents in these fields. Ms. Alqahtani is also a reviewer for international scientific journals, including the Molecular Structure Journal and Springer Nature.

Partners & Sponsors

" Together, advancing the frontiers of chemistry for a better tomorrow "

PRINICIPAL

Diamond

STRATEGIC PARTNERS

THE JOURNAL OF CHEMICALS RESEARCH & INNOVATION SOCIETY

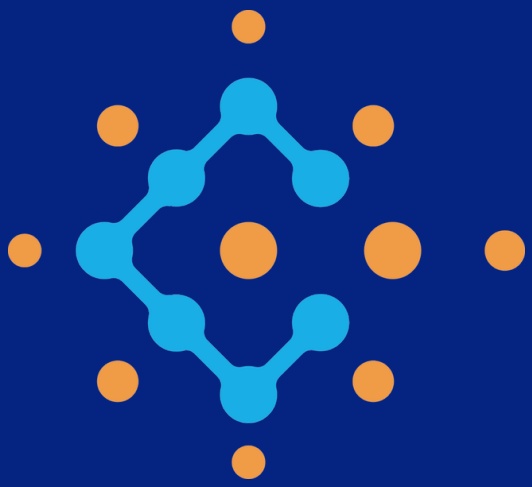

editorial@cris.org.sa

www.cris.org.sa

@chemreain